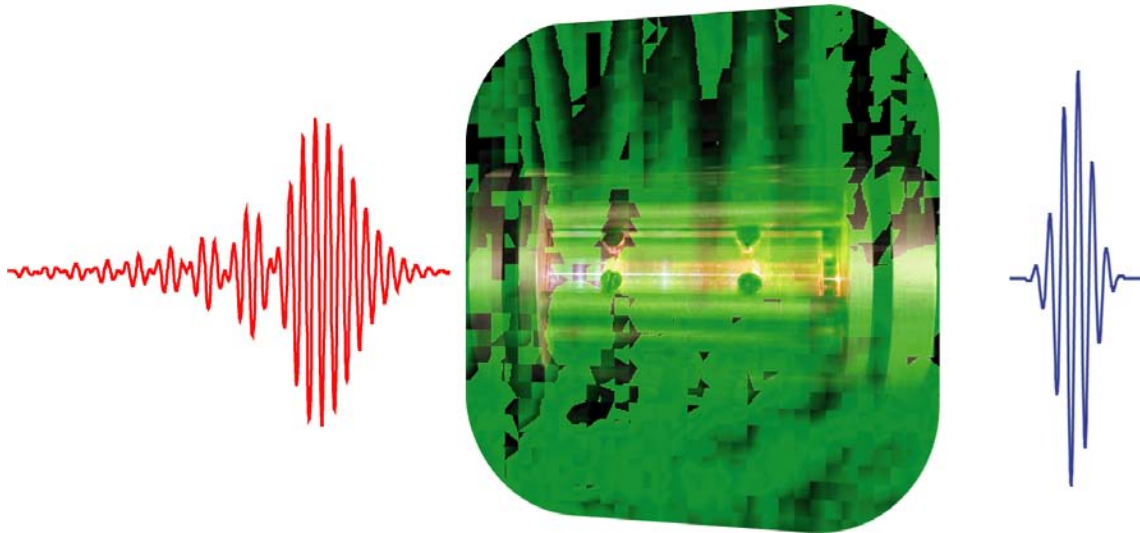


Adaptive Control of Ultrashort Laser Pulses for High-Harmonic Generation



**Dissertation zur Erlangung des
naturwissenschaftlichen Doktorgrades
der Bayerischen Julius-Maximilians-Universität
Würzburg**

vorgelegt von
Dominik Walter
aus Würzburg

Würzburg 2006

Eingereicht am: 20.12 2006
bei der Fakultät für Physik und Astronomie

Gutachter der Dissertation:

1. Gutachter: Prof. Dr. G. Gerber
2. Gutachter: Prof. Dr. J. Geurts

Prüfer im Promotionskolloquium:

Prof. Dr. G. Gerber
Prof. Dr. J. Geurts
Prof. Dr. W. Kinzel

Tag der mündlichen Prüfung (Promotionskolloquium): 23. Februar 2007

List of Publications

Parts of this work have been published in the following references:

M. Y. Emelin, M. Y. Ryabikin, A. M. Sergeev, M. D. Chernobrovtsseva, T. Pfeifer, D. Walter, and G. Gerber.

Attosecond Burst and High-Harmonic Generation in Molecular Ionization by Ultrashort Laser Pulses.

JETP Lett. **77**, 212–216 (2003).

A. Flettner, T. Pfeifer, D. Walter, C. Winterfeldt, C. Spielmann, and G. Gerber.

High-harmonic generation and plasma radiation from water microdroplets.

Appl. Phys. B **77**, 747–751 (2003).

T. Pfeifer, D. Walter, G. Gerber, M. Y. Emelin, M. Y. Ryabikin, M. D. Chernobrovtsseva, and A. M. Sergeev.

Transient Enhancement of High-Harmonic Generation in Expanding Molecules.

Phys. Rev. A, **70**, 013805 (2004).

T. Brixner, C. Dietl, G. Krampert, P. Niklaus, E. Papastathopoulos, T. Pfeifer, R. Selle, G. Vogt, D. Walter, C. Winterfeldt, and G. Gerber

Adaptive femtosecond quantum control,

In F. Krausz, G. Korn, P. Corkum, and I. A. Walmsley (Eds.), *Ultrafast Optics IV,*

Vol. 95 of *Springer Series in Optical Sciences*, pp. 117-126, Springer, Berlin (2004).

T. Pfeifer, D. Walter, C. Winterfeldt, C. Spielmann, and G. Gerber.

Adaptive engineering of coherent soft x-rays,

in *Ultrafast Phenomena XIV*, (eds. T. Kobayashi, T. Okada, T. Kobayashi, K. A. Nelson, and S. de Silvestri) (Springer, Berlin, 2004), Vol. 79 of *Springer Series in Chemical Physics*, pp. 178-180.

T. Pfeifer, D. Walter, C. Winterfeldt, C. Spielmann, and G. Gerber.

Controlling the spectral shape of coherent soft X-rays,

Appl. Phys. B **80**, 277–280 (2005).

T. Pfeifer, R. Kemmer, R. Spitzenpfeil, D. Walter, C. Winterfeldt, G. Gerber, and C. Spielmann.

Spatial control of high-harmonic generation in hollow fibers,

Opt. Lett. **30**, 1497–1499 (2005).

M. Yu. Emelin, M. Yu. Ryabikin, M. D. Chernobrovtsseva, A. M. Sergeev, T. Pfeifer, D. Walter, and G. Gerber.

High-efficiency generation of attosecond pulses during atomic ionization from excited electronic states,

Europhys. Lett., 69 (6), pp. 913-919 (2005).

D. Walter, T. Pfeifer, C. Winterfeldt, R. Kemmer, R. Spitzenpfeil, G. Gerber, and C. Spielmann.

Adaptive spatial control of fiber modes and their excitation for high-harmonic generation, Opt. Expr., Vol. 14, Issue 8, pp. 3433-3442 (2006).

C. Winterfeldt, T. Pfeifer, D. Walter, R. Kemmer, A. Paulus, R. Spitzenpfeil, G. Gerber, and C. Spielmann.

Adaptive temporal and spatial shaping of coherent soft x-rays,

Proc. SPIE Vol. 6187, Photon Management II, eds. J. T. Sheridan, F. Wyrowski, ISBN 0-8194-6243-8, 61870F (2006).

C. Winterfeldt, J. Lohbreier, A. Paulus, T. Pfeifer, R. Spitzenpfeil, D. Walter, G. Gerber, and C. Spielmann.

Adaptive spatial control of high-harmonic generation,

in Ultrafast Phenomena XV, (eds. R. J. D. Miller, A. M. Weiner, P. Corkum, D. Jonas) (Springer, Berlin, 2006), Springer Series in Chemical Physics.

T. Pfeifer, F. Dimler, R. Spitzenpfeil, D. Walter, C. Winterfeldt, C. Spielmann, and G. Gerber.

Optimal control with shaped soft-x-ray light,

Opt. Expr., accepted (2007).

D. Walter, S. Eyring, J. Lohbreier, R. Spitzenpfeil, and C. Spielmann.

Spatial Optimization of Filaments, submitted.

D. Walter, S. Eyring, J. Lohbreier, R. Spitzenpfeil, and C. Spielmann.

Two-dimensional evolutionary algorithm designed for spatial shaping of ultrashort laser pulses with high resolution,

in preparation.

Further publications beyond the scope of this work:

A. Paulus, C. Winterfeldt, T. Pfeifer, D. Walter, G. Gerber, and C. Spielmann.

Novel time-of-flight electron spectrometer optimized for time-resolved soft-x-ray photoelectron spectroscopy,

Rev. Sci. Instrum. **77**, 043105 (2006).

Contents

List of Publications	iii
1 Ultrashort Laser Pulses (NIR)	3
1.1 Mathematical Description	4
1.2 Titanium:Sapphire Laser System	6
1.3 Nonlinear Optical Kerr Effect	9
1.3.1 Self-Focusing	10
1.3.2 Self-Phase Modulation	10
1.4 Temporal Characterization	12
1.4.1 Interferometric Autocorrelation	12
1.4.2 Spectral Interferometry	14
1.4.3 SPIDER	15
1.5 Femtosecond Pulse Shaping	16
1.5.1 Pulse Shaping Devices	17
1.5.2 Learning Algorithm	19
1.6 Applications of Ultrashort Pulses	20
2 Adaptive Temporal Compression of Ultrashort Laser Pulses	23
2.1 Temporal Compression in a Hollow Fiber Setup	25
2.1.1 Temporal Compression	26
2.1.2 Spatio-temporal Compression	29
2.2 Temporal Compression by Filamentation	32
2.2.1 Generation of Light Filaments	33
2.2.2 Temporal Compression	34
2.2.3 Spatio-temporal Compression	36
2.2.4 Adaptive Compression using SPIDER	37
2.2.5 Spatial Optimization of the Beam Profile	41
2.3 Conclusion	44
3 High-Harmonic Generation	47
3.1 Theoretical Description	48
3.1.1 Three-Step Model	49
3.1.2 Quantum Mechanical Description	51

3.2	Sub-fs Pulse Production	55
3.3	Characterization Techniques	56
3.4	Experimental Realization of High-Harmonic Generation	57
3.4.1	Basic setup: Gas Jet	58
3.4.2	Gas-filled Hollow-Core Fiber	60
3.4.3	Water Microdroplets	65
3.5	Optimization Schemes	72
3.5.1	HHG from Excited Electronic States	73
3.5.2	HHG in Expanding Molecules	76
3.5.3	Outlook: Pulse Shaping	82
3.6	Competitive Sources of Ultrashort EUV and X-Ray Radiation	83
4	Adaptive Optimization of High Harmonics	85
4.1	Optimization Setup	86
4.2	Controlling the Spectral Shape of High Harmonics	87
4.2.1	Gas-Jet Setup	87
4.2.2	Hollow-Fiber Setup	89
4.3	Spatial Control of High-Harmonic Generation in Hollow Fibers	96
A	Programmable Phase Modulator Hamamatsu X8267	111
B	Two-dimensional Implementation of the Evolutionary Algorithm	117
	Bibliography	119
	Acknowledgments	137
	Curriculum Vitae	139

Introduction

Curiosity and the desire to understand the world around them is one of the most valuable human traits that has helped to discover fundamental laws and to develop basic techniques to control fundamental processes. After mastering the laws of classical mechanics at the end of the 19th century, however, there was a feeling that nothing new was left in the field of physics—“almost everything is already discovered, and all that remains is to fill a few holes,” as the Munich physics professor Philipp von Jolly told the 16 year-old Max Planck at the begin of his studies in 1874.

In 1900 Max Planck discovered that the energy of waves could be described as consisting of small packets or quanta. Subsequent investigations led to the discovery of the quantum nature of electromagnetic waves and the wave-like behaviour of matter—the era of quantum mechanics was born. The discovery of the quantum structure of atoms and light allowed a closer look into the finer structure of matter. On its smallest scales the world is full of details that have yet to be discovered.

Since this time there has been much progress in the understanding of these light quanta, the photons, and their potential to help us “see” the mechanics of physics on the most microscopic and macroscopic levels. With the advent of the “LASER” in 1960 a device was introduced that works as a coherent source of light—from this time on, the properties of the light field could be controlled in a well-defined manner and were used as an instrumental tool of high precision.

Only few decades later, in the era of photonics, ultrashort pulses of this laser light have become a basic tool in physics. In 1999 Ahmed H. Zewail won the Nobel Prize in Chemistry for his pioneering work that enabled chemists to see how reactions proceed on a time scale of few hundreds of femtoseconds using ultrashort pulses. The time scale of atomic vibrations was approached and now chemical processes can be traced and even controlled to a certain extent. This is achieved by manipulating the electronic motion with engineered electric fields inside complex molecules.

Electrons are of fundamental value as they can trigger or mediate virtually all processes in biology, chemistry and physics. The dream to control electron dynamics with laser fields in real time is nearly achieved. Science is about to enter a new field of ultrafast physics devoted to the direct exploration of electronic motion.

For the precise study of matter and its interaction with electromagnetic radiation, we need to know how to handle and manipulate our tool, the light.

This will be the topic of this thesis: The generation and modification of intense ultrashort light pulses in a controlled manner. Confining infrared (IR) laser fields to femtosecond time scales ($1 \text{ fs} = 10^{-15} \text{ s}$) allows for intensities high enough to exploit nonlinear features of matter that will influence the interacting light. Subsequent spatial confinement to the micrometer scale then generates intensities much higher than the Coulomb binding force in atoms. The radiation, that is generated during the fast recombination of field ionized electrons with an ionic core, forms energetic soft x-ray light pulses of durations below a single femtosecond. Even these shortest man-made pulses can be engineered by the laser light that generates them—we now have the possibilities to control electronic motion on its natural time scale.

This work is divided into four chapters. Chapter 1 gives the necessary background for the generation, characterization and modification of ultrashort laser pulses. It also includes nonlinear effects that will be important. Chapter 2 is devoted to efficient temporal compression of those pulses to even shorter durations. Different compression setups are investigated that adaptively can optimize the spatial and spectral properties of laser pulses in the visible and near infrared (NIR) spectral range. This is the preparation for Chapter 3 in which ultrashort pulses are used for frequency up-conversion in a process called “high-harmonic generation” (HHG). It covers the theoretical background and basic setups for high-harmonic generation. Different methods are described to enhance the conversion process to yield powerful soft-x-ray pulses with attosecond time structure. The technique of femtosecond laser shaping is then applied in Chapter 4 to optimize the high-harmonic generation process and to control the spatial and spectral properties of the generated radiation in the extreme ultraviolet (XUV) spectral region.

Chapter 1

Ultrashort Laser Pulses (NIR)

The generation, modification and application of ultrashort laser pulses is involved in all different aspects of this work. Ultrashort laser pulses are bursts of electromagnetic radiation that are of the order of 10^{-15} s. These short time scales cannot be reached by any means to mechanically “cut” slices of light pulses with shutters. Even high-speed electronic shutters, like Pockels-cells, only operate on a time scale of few nanoseconds ($1 \text{ ns} = 10^{-9}$ s). To generate a short pulse of “waves” in time, a number of waves with different frequencies have to be combined and have to be able to constructively interfere. The more frequencies can contribute, the shorter the resulting pulse can be. This ultimately leads to an uncertainty product, the time-bandwidth product:

$$\tau_p \Delta\omega \geq 2\pi c_B \quad (1.1)$$

with τ_p being the pulse duration and $\Delta\omega$ the spectral bandwidth of the laser pulse at its full-width half-maximum (FWHM). The factor c_B is of the order of 1 (for Gaussian shaped field-envelopes $c_B \approx 0,441$ [1]). Eq. (1.1) quantitatively connects the shortest pulse duration that will be possible for a given spectrum of frequencies. The more detailed mathematical description will be found in the following section.

In the early days of lasers a continuous wave (cw) of coherent light with small bandwidth was emitted. Not much later the method of Q-switching was proposed by Hellwarth in 1961 [2] and pulsed laser output not much shorter than 100 ns was possible. The need for finer time resolution led to the discovery that many different laser modes can be coupled to form pulses with broader bandwidth. This technique of “mode-locking” [3] is still used today in much more advanced systems and is described in Section 1.2, which deals with nowadays commercially available laser systems that can already generate intense laser pulses of the order of few tens of femtoseconds. Section 1.3 describes nonlinear effects that will be important throughout this work. The peak intensity of ultrashort laser pulses is strong enough that it will “feel” the matter it interacts with. This interaction will change the spatial and spectral properties of the light. As there exists no shutter to generate ultrashort pulses it is understandable that they will also be much faster than conventional measurement devices. However, the rich effects of nonlinear optics can be exploited to analyze modified replica of the ultrafast laser pulses to be able to reconstruct their hidden phase information. Different characterization setups can be found in Section 1.4.

Nonlinear effects can be used to broaden the spectrum of the pulses. Their temporal phase

information, on the other hand, can be modified in simple setups using different spectral phase modulators (Section 1.5.1). The challenging aspect in engineering spectral phases is the high degree of freedom of today's pulse shaping devices. Our tool, the laser pulse, must have "the ideal" shape to be able to efficiently work as intended. This is a nontrivial problem and there exists no general solution to date. However, with the help of iterative algorithms the optimal pulse shape can be approached by a "trial-and-error" method. One of the best time-tested iteration is that of evolution itself and will be the driving force in most experiments. Different implementations of these "evolutionary algorithms" are used in this work. Due to their "own" evolution and because they can be treated as a mere tool throughout this work the details are summarized in Appendix B.

The final section gives a short overview of important applications of ultrashort laser pulses that are thematically not part of this work.

1.1 Mathematical Description

The dynamics of electromagnetic waves are described as a solution of Maxwell's equations [4]:

$$\nabla \cdot \mathbf{D} = \rho, \quad (1.2)$$

$$\nabla \cdot \mathbf{B} = 0, \quad (1.3)$$

$$\nabla \times \mathbf{E} = -\frac{\partial \mathbf{B}}{\partial t}, \quad (1.4)$$

$$\nabla \times \mathbf{H} = \mathbf{J} + \frac{\partial \mathbf{D}}{\partial t}. \quad (1.5)$$

To describe a laser pulse, we are first interested in the simplest solution of a plane electromagnetic wave propagating in vacuum. For sake of simplicity, any spatial dependence of the electric field will be neglected. The field will be described as a function of its propagation coordinate z and its temporal evolution. Important spatial effects and complicated nonlinear interactions will be presented later (see Section 1.3). The solutions in terms of the electric field strength $E(z, t)$ can be written as:

$$E(z, t) = E_0 \cos(k_z z - \omega(k_z) t). \quad (1.6)$$

k_z is the wave vector \vec{k} in the direction of propagation z , ω is the angular frequency, and E_0 is the field amplitude. The function $\omega(\vec{k})$ is the dispersion relation of the medium, with the ratio $\omega/|\vec{k}|$ being the phase velocity of light $\nu = c/n$ (c is the speed of light in vacuum).

The duration of such a monochromatic plane wave is infinite. As mentioned above, to generate short pulses a broad spectrum is needed. A short pulse results as superposition of many plane waves with different frequencies. The temporal electric field for a pulse is simply obtained by replacing the constant field amplitude E_0 with a time-dependent field amplitude $E_0(t)$ (also denoted as field envelope).

Using the convention that physical electric fields are obtained by taking the real parts of complex quantities, the electric field for a pulse at a fixed point in space can be written as:

$$E(t) = E_0(t)e^{i\phi(t)}, \quad (1.7)$$

where i is the imaginary unit, and $\phi(t)$ the time-dependent phase function. The spectral amplitude $E(\omega)$ is given by Fourier transformation of Eq. (1.7):

$$E(\omega) = \frac{1}{\sqrt{2\pi}} \int_{-\infty}^{\infty} E(t)e^{-i\omega t} dt = \sqrt{I(\omega)}e^{-i\phi(\omega)}. \quad (1.8)$$

The squared modulus of $E(\omega)$ gives the spectral intensity $I(\omega)$ that is the most easily accessible quantity for experimenters. In analogy, the temporal intensity $I(t)$ is defined as $E_0(t)^2$. The pulse duration τ_p and spectral bandwidth $\Delta\omega$ of the field envelopes of $I(t)$ and $I(\omega)$ are then connected by the time-bandwidth product (Eq. (1.1)) that was already introduced above.

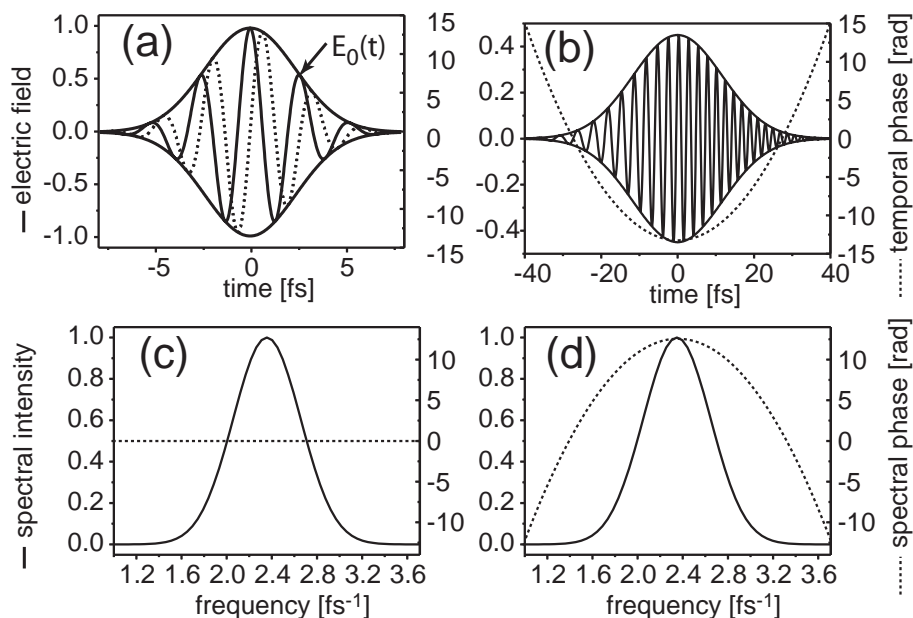


Figure 1.1: Temporal laser pulse shapes for a bandwidth limited 4 fs pulse (a) and a chirped pulse (b). The dotted line in (b) represents the temporal phase. (c) and (d) show the corresponding spectral intensities and spectral phases. As the spectral phase of (a) is flat, its temporal phase will be also flat (not shown). The dotted line in (a) gives an example of a second temporal pulse shape with a $\pi/2$ shifted carrier-envelope phase.

Fig. 1.1 gives an overview of important quantities. In Fig. 1.1a the electric field of a 4 fs pulse is plotted together with its field envelope $E_0(t)$. The dotted line depicts a second pulse with a $\pi/2$ shifted temporal phase. The phase shift of the carrier-frequency with respect to the envelope is called the carrier-envelope phase (CEP) and will play a crucial role in experiments with few cycle pulses [5, 6]. If the pulse durations are long compared to the single cycle duration of the carrier wave the CEP will become negligible.

As was already stated above, the broader the spectrum the shorter the pulse can be. How short it will be for a given spectrum depends on its spectral phase $\phi(\omega)$. Fig. 1.1c shows the spectral intensity (= spectrum) and the spectral phase for the pulse in Fig. 1.1a. A constant phase leads to equality of Eq. (1.1). Such pulses are called bandwidth-limited pulses. They will have the smallest possible FWHM for a given spectrum. This ideal case of pulses with flat spectral phases will be aspired in Chapter 2. During the generation process and any kind of nonlinear interaction the spectral phase can get distorted. Correction of these distortions is a nontrivial matter and not always possible.

One simple case of a nonconstant spectral phase $\phi(\omega)$ is a linear dependence which results in the temporal displacement of pulses. A quadratic dependence will stretch a pulse in time (Fig. 1.1b, d). This effect is important when light travels in dispersive media with different phase velocities due to a wavelength dependent index of refraction $n(\lambda)$. This is the most basic kind of a “chirped” pulse (i.e. a pulse with nonconstant spectral phase $\phi(\omega)$ of the order ≥ 2) as the frequency will change only linearly in time (linear “chirp”). The term “spatial chirp” is also used for nonconstant spatial frequency distributions (important in Chapter 2).

However, even for the bandwidth limited case, the central wavelength represents the final limit for the shortest of pulses. The electric field of each pulse must satisfy

$$\int_{-\infty}^{\infty} E(t)dt = 0, \quad (1.9)$$

to be a physically reasonable solution.

The acronym “NIR” in the headline of this chapter denotes the near infrared frequency range. For a central wavelength of 800 nm the pulse durations are limited to about 2.7 fs. As will be shown in the next section, the widely used Ti:Sa laser-systems work in this frequency range. At higher frequencies shorter light pulses are possible and will be the topic in Chapter 3.

The technical realization of such kinds of light pulses is not intuitive. A laser-system for the generation of ultrafast pulses has to provide a wide range of frequencies that are mode-locked to each other and only low order chirp may be introduced that can easily be compensated. For the experiments presented in this thesis two different Ti:Sa laser systems were used. However, they share the same design concepts that are described in the next section.

1.2 Titanium:Sapphire Laser System

The goal of an ultrashort-pulsed laser-system is to maximize the peak intensity of its output pulses. This is generally achieved by confinement of amplified laser energy to very short durations as will be described below.

The development from the first systems that were based on light amplification by stimulated emission of radiation (“LASER”) to nowadays compact and reliable ultrashort-pulsed laser-systems follows an exciting road full of discoveries and technical innovation.

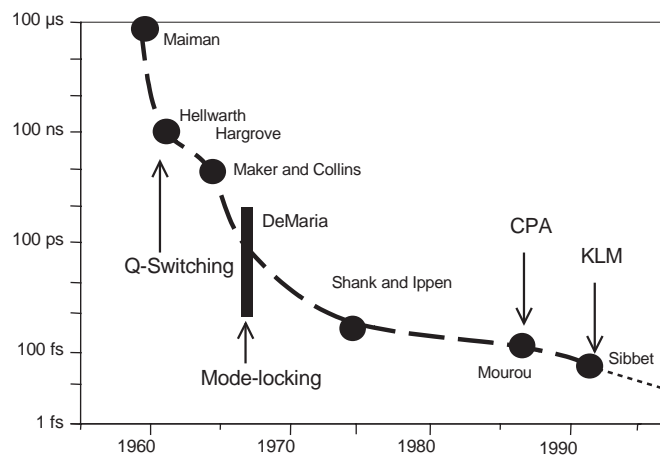


Figure 1.2: Timeline of the evolution of the shortest visible laser pulse lengths. Important innovations are specially marked (adapted from [7]).

Extended historical reviews about this subject can be found in [8] and [7]. The following paragraph gives only a short summary of the most important steps in its evolution (see Fig. 1.2).

With the innovative method of mode-locking in 1966 [3] pulses with durations of 100 ps were possible. Mode-locking means that a fixed phase relationship is achieved between the longitudinal modes in a laser cavity and it is the key for the generation of short laser pulses. The additional discovery and application of broad-gain dye laser media and further technical innovations in the seventies [9] could decrease the new limit into the sub-ps regime. This development was peaked with the introduction of the organic dye Rhodamine 6G (Rh6G) as gain medium at a wavelength of about 620 nm (sub 100 fs). Dye lasers were used for many years to come.

Beginning in 1986, the advent of sapphire crystals that were doped with titanium ions as active medium (Ti:Sa [10]) replaced the widespread use of dyes. The solid state gain medium had a whole list of advantages: smaller sized setups were possible and the performance and reproducibility of the systems were superior—not to forget that no more hazardous dyes were required. The Ti:Sa has the broad bandwidth of 650 nm to 1100 nm and introduced the new central wavelength of about 800 nm. The final improvement, that will be discussed here, was developed in the end of the eighties: Kerr-lens modelocking (KLM [11]).

The Kerr-lens effect is the nonlinear effect of self-focusing of intense laser pulses in dispersive materials (see Section 1.3 for detailed explanation of self-focusing). As illustrated in Fig. 1.3 this effect can be used to favor the coupling of many different laser modes. Only by mode-coupling an intense laser pulse will be formed that can self-focus in the laser crystal and pass the aperture of Fig. 1.3 without additional losses. Any single-modes, however, will not pass the aperture and will thus be suppressed. Kerr-lens mode-locked

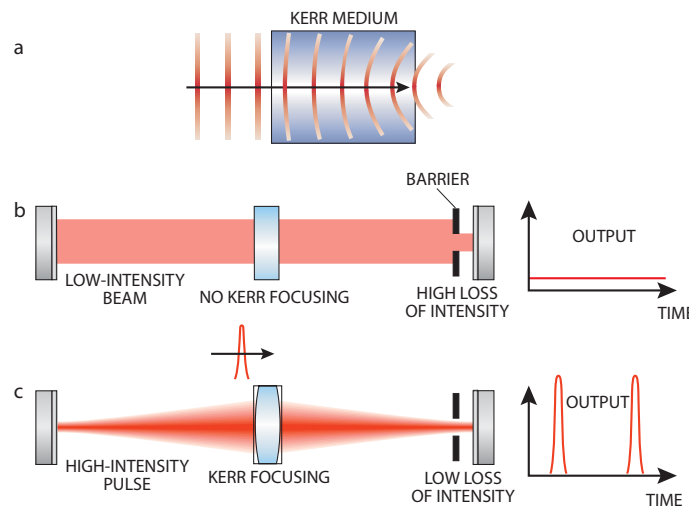


Figure 1.3: Kerr-lens modelocking in laser resonators [12]. At high peak intensities laser pulses start to self-focus in the laser crystal (a). By placing an aperture in the resonator ((b), (c)), mode-locked laser pulses (higher peak intensity (c)) have lower losses than pulses with lower peak intensities (b). Therefore, only mode-locked pulses can be amplified efficiently.

lasers have the drawback that they need a small perturbation to start pulsing (usually achieved by mechanically ‘shaking’ one of the cavity mirrors). Pulses generated in such laser systems (oscillators) have relatively low output, because high gains would damage the Ti:Sa crystal. However, they can be used as ‘seeds’ for amplifier systems.

Ti:Sa oscillators generate a train of pulses with 5-100 fs duration at a repetition rate of the order of 100 MHz. The average power is usually of the order of several 100 mW with an energy of about 1 nJ per pulse. The pulses can be focused to yield intensities of the order of 10^{12} W/cm². For the experiments presented in this work much higher intensities are needed (focused intensities of 10^{14} W/cm²).

The method of choice to amplify ultrashort pulses is called “Chirped Pulse Amplification” (CPA) and was developed by Strickland and Mourou in 1985 [13]. As the name implies a temporally chirped version of the laser pulse gets amplified. This is done in a second Ti:Sa crystal. Due to the temporal spread of frequencies the peak intensity of the pulse is lowered and the chirped version can be amplified again without damaging the crystal. The amplified beam is afterwards temporally compressed and a much more intense femtosecond pulse is obtained (Fig. 1.4).

For the experiments presented in Chapter 3 and 4 a regenerative Ti:Sa amplifier with 80 fs output-pulses was used (“Spitfire” (Spectra Physics)). The pulse-compression experiments of the next chapter were performed with a multipass amplifier with 30 fs output pulses (Femtopower Compact Pro (Femtolasers)). Both laser systems operate at a repetition rate of 1 kHz with a pulse energy of about 0.8 mJ.

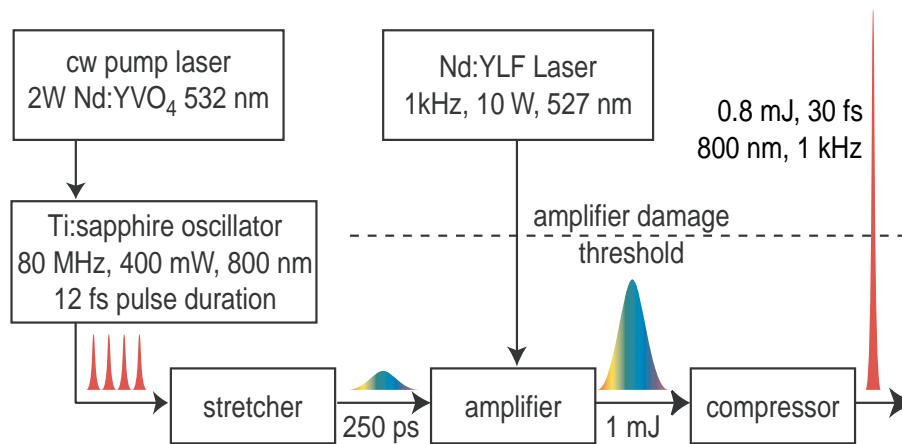


Figure 1.4: Ultrashort laser amplification system based on the CPA-technique. The laser pulses emitted of a fs-oscillator are stretched in time (stretcher) before they get amplified (amplifier). Amplified peak intensities will be kept below the amplifier damage threshold and are compressed again to short durations (compressor).

1.3 Nonlinear Optical Kerr Effect

Polarization is the response of matter to external electric fields. For low field strengths—“low” means that the electron can be described as bound particle in a parabolic potential—this response stays linear. The nonlinear regime can be easily accessed by the high field strengths of ultrashort laser pulses. The nonlinear polarization is given by:

$$P(t) \propto \chi^{(1)}E(t) + \chi^{(2)}E^2(t) + \chi^{(3)}E^3(t) + \dots \quad (1.10)$$

Here, the coefficients $\chi^{(n)}$ are the n -th order susceptibilities of the medium. As illustrated in Fig. 1.5, the effect of higher order terms introduces distortions and the polarization can no longer “follow” the electric field. Depending on the interaction parameters a number of surprising nonlinear effects are revealed. Many nonlinear effects are already beneficially exploited for various optical systems, but generally they will make experiments with intense laser pulses more complicated—especially if they can really “surprise” the experimenter.

The optical Kerr effect is already known from the method of Kerr-lens modelocking described in the previous section. This effect is based on an intensity dependence of the refractive index at high intensities:

$$\Delta n(\vec{r}, t) = n_2 I(\vec{r}, t), \quad (1.11)$$

with n_2 being the nonlinear index of refraction. In terms of the nonlinear polarization defined in Eq. (1.10) n_2 can be expressed as [1]:

$$n_2 = \frac{3\chi^{(3)}}{4\varepsilon_0 c n_0^2}, \quad (1.12)$$

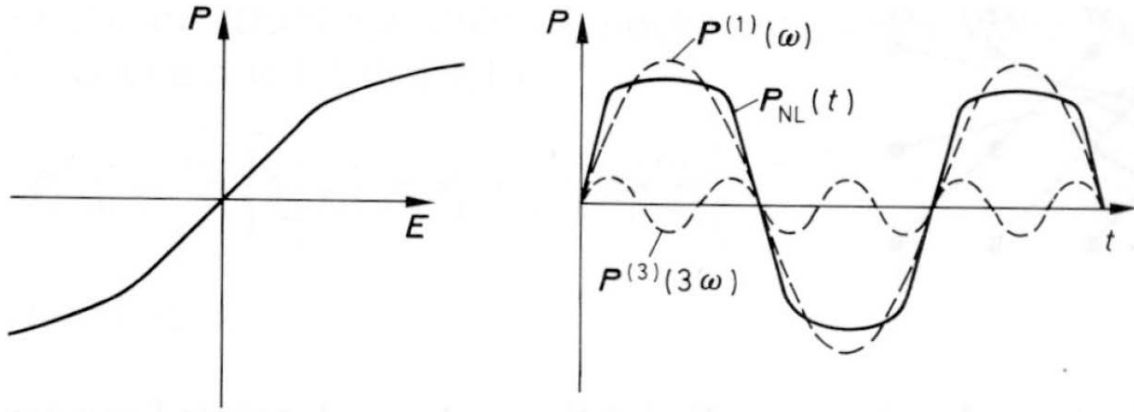


Figure 1.5: nonlinear polarization response of systems with inversion symmetry [14].

with $\chi^{(3)}$ being the 3rd-order susceptibility and ε_0 being the vacuum dielectric constant. In air, at the laser wavelength of $\lambda_0 = 800$ nm, the nonlinear index of refraction is: $n_2 = 3.2 \times 10^{-19}$ cm²/W [15]. This intensity dependence is responsible for the effects of self-focusing and self-phase modulation.

1.3.1 Self-Focusing

The nonlinear effect of self-focusing is a consequence of the spatial intensity distribution of a laser pulse. This distribution can generally be assumed to be radially symmetric and having a gaussian profile. Therefore, its intensity will be high in the inner region and slowly decrease to the outer region. Due to Eq. (1.11) the nonlinear index of refraction has the same spatial distribution as the intensity. As n_2 is positive in most materials, this will lead to a lensing effect and the laser pulse gets focused (see Fig. 1.3). A critical power P_{crit} can be defined, above which a laser pulse will start to self-focus [16]:

$$P_{crit} = \frac{\lambda_0^2}{2\pi n_0 n_2}. \quad (1.13)$$

In air, at the laser wavelength of $\lambda_0 = 800$ nm the critical power for self-focusing is about 3.2 GW. This effect is essential for the Kerr-lens mode-locking mechanism described above (Fig. 1.3). It will also play a dominant role for the generation of light-filaments discussed in Chapter 2.

1.3.2 Self-Phase Modulation

For the nonlinear effect of self-phase modulation the temporal intensity distribution is important. Self-phase modulation (SPM) can be understood from a qualitative point of view. An analytical explanation will also be given below.

In analogy to the effect of self-focusing, we will assume a Gaussian shaped temporal intensity distribution of the laser pulse. This has the effect that the refractive index $n(t)$ will

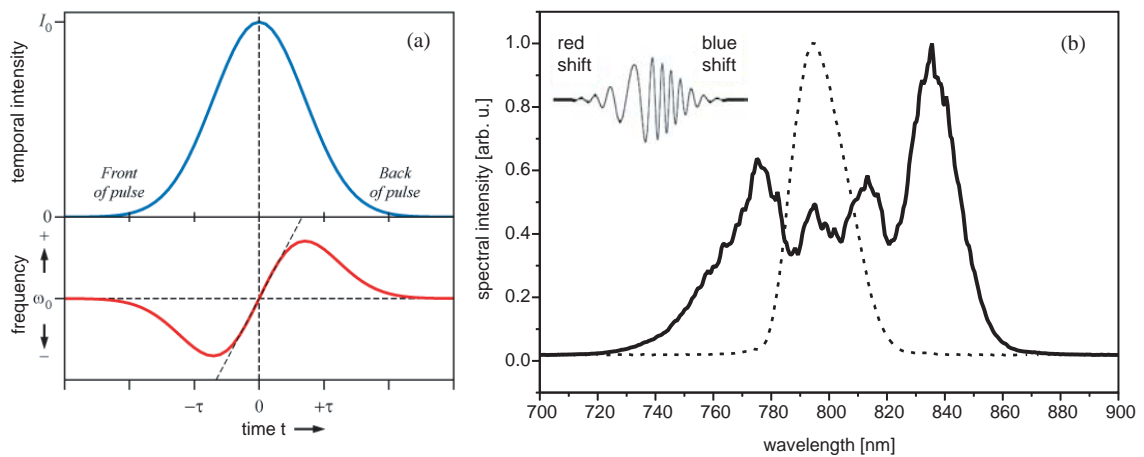


Figure 1.6: The nonlinear effect of self-phase modulation. Due to an intensity dependent index of refraction the frequency components of a laser pulse will be shifted (a), leading to a broadening of the spectrum (b). The front of the pulse is shifted to lower frequencies (redshift) and the back of the pulse to higher frequencies (blueshift) [17]. (b) Spectrally broadened laser pulse before (dotted line) and after self-phase modulation in a hollow fiber setup (solid line).

rise in the leading edge of the pulse due to increasing intensities—and it will decrease during the trailing edge. Keeping the definition of the phase velocity $v = c/n$ in mind, we have a decreasing phase velocity in the leading edge—this will stretch the wavelengths, causing a redshift of the spectrum. In the trailing edge the reverse effect will happen: the phase velocity will increase more and more to the end of the pulse—this will compress the wavelengths causing a blueshift of the spectrum (see Fig. 1.6a).

This example demonstrated that parts of a given spectrum will be blueshifted and redshifted at the same time—in other words: the spectrum will broaden (Fig. 1.6b).

In mathematical terms, a monochromatic electric field with the time dependent nonlinear term of the refractive index $n(t)$ can be written as:

$$E(z, t) = E_0 e^{i(\omega t - kz)} = E_0 e^{i(\omega t - n(t) \frac{\omega}{c} z)} = E_0 e^{i\Phi(t)}. \quad (1.14)$$

The instantaneous frequency ω at time t is:

$$\omega(t) = \frac{d\Phi(t)}{dt} = \omega_0 - \frac{dn(t)}{dt} \frac{\omega}{c} z = \omega_0 - n_0 \frac{\omega}{c} z - n_2 \frac{dI(t)}{dt} \frac{\omega}{c} z. \quad (1.15)$$

The frequency will shift according to the derivative of the intensity $\frac{dI(t)}{dt}$ of the pulse. This relationship is also plotted in Fig. 1.6a. The effect of self-phase modulation will be used in the next chapter for spectral broadening in gas-filled hollow fibers [18, 19] and filaments [20].

1.4 Temporal Characterization

As briefly mentioned before, there are no common detectors that are fast enough to record the temporal intensity profile of ultrashort laser pulses. With the help of the nonlinear effects described above, clever optical setups have been developed to circumvent this problem. Only the two temporal characterization techniques that are used in this work are described in detail. They all work with replica of the laser pulse that is to be diagnosed—the pulse is used to measure itself!

1.4.1 Interferometric Autocorrelation

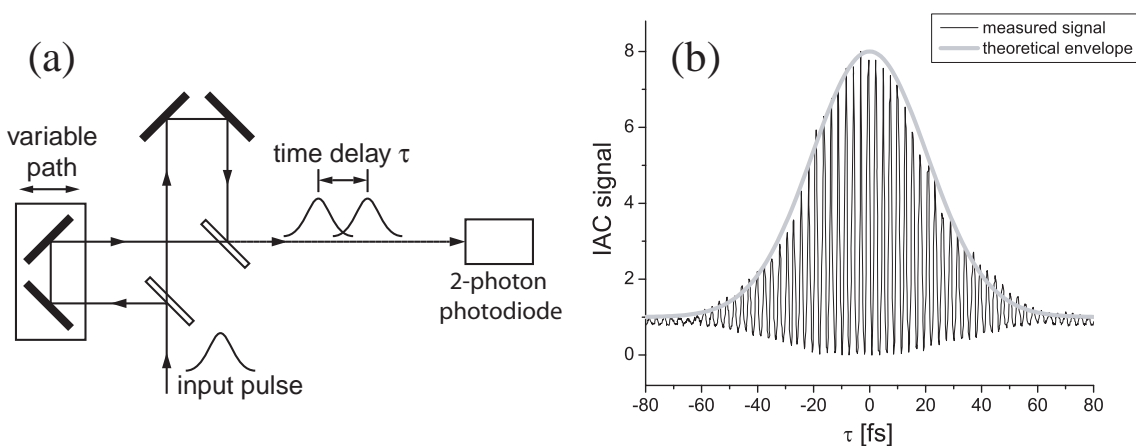


Figure 1.7: (a) Mach-Zehnder autocorrelation setup for temporal laser pulse characterization. The interference signal of two pulse replica that are delayed in time with respect to each other is recorded in a two-photon photodiode. The interferometric autocorrelation signal I_{IAC} is obtained as function of the delay. (b) Autocorrelation trace of the 30 fs amplifier output of the Femtopower laser system (black curve) together with its calculated envelope (grey curve).

The setup for the interferometric autocorrelation is based on a Michelson- or Mach-Zehnder interferometer (see Fig. 1.7a). In these setups two replica of the laser pulse are generated by beam-splitters. One of these pulses is then variably delayed with respect to the other before they are recombined collinearly. Then they are spatially overlapped in an instantaneously responding nonlinear optical medium. The autocorrelation signal is obtained as a function of the delay between the two pulses.

Commonly the second-harmonic signal that is generated in a nonlinear crystal (SHG crystal [21]) is detected with a photodiode. An alternative method is to use photodiodes with large bandgaps, where only two-photon absorption in the photodiode contributes to the photocurrent, while the photon energy is smaller than the bandgap. Both of these effects (frequency-doubling, two-photon absorption) depend quadratically on the intensity.

The recombined electric field of both replica $E_{\text{res}}(t, \tau)$ is given by:

$$E_{\text{res}}(t, \tau) = E(t) + E(t - \tau). \quad (1.16)$$

Depending on the delay τ between the two pulses, $E_{\text{res}}(t, \tau)$ is the result of constructive or destructive interference. If the electric field of both pulses overlap completely ($\tau = 0$) the highest signal is expected. The measured interferometric autocorrelation intensity $I_{\text{IAC}}(\tau)$ is then proportional to the measured photocurrent:

$$I_{\text{IAC}}(\tau) = \int_{-\infty}^{+\infty} |E_{\text{res}}(t, \tau)|^2 dt = \int_{-\infty}^{+\infty} |(E(t) + E(t - \tau))|^2 dt. \quad (1.17)$$

For the case of a large τ and no temporal overlap between the two pulses, one obtains:

$$I_{\text{IAC}}(\infty) = \int_{-\infty}^{+\infty} |E(t)|^2 dt + \int_{-\infty}^{+\infty} |E(-\infty)|^2 dt = 2 \int_{-\infty}^{+\infty} E^4(t) dt. \quad (1.18)$$

On the other hand $I_{\text{IAC}}(0)$ yields:

$$I_{\text{IAC}}(0) = \int_{-\infty}^{+\infty} |(2E(t))|^2 dt = 16 \int_{-\infty}^{+\infty} E^4(t) dt. \quad (1.19)$$

The ratio $I_{\text{IAC}}(0) : I_{\text{IAC}}(\infty)$ gives the characteristic peak to background ratio of 8:1 that can be seen in Fig. 1.7b. A typical autocorrelation signal for a near bandwidth-limited 30 fs pulse is plotted in Fig. 1.7b. It consists of an oscillating carrier signal that is the result of the interference of the two electric fields. The DC-part of this signal gives the result of an *intensity autocorrelation* [1]. The information of the duration of the pulse can be extracted from the envelope of I_{IAC} . However, no information about the actual temporal pulse shape can be obtained. If we assume a sech^2 -pulse, the ratio between τ_{IAC} (the FWHM of the interferometric autocorrelation signal I_{IAC}) and τ_{p} (the FWHM of $I(t)$) gives the deconvolution factor:

$$\frac{\tau_{\text{IAC}}}{\tau_{\text{p}}} \approx 1.9. \quad (1.20)$$

This ratio, however, depends on the real temporal laser pulse shape and has therefore to be used with care. Table 8.1 in Diels et al. [1] contains a list of deconvolution factors for different pulse envelopes. The interferometric autocorrelation is sensitive to chirps and thus in principle allows to extract more information on the pulses than the intensity autocorrelation [1]. However, for chirped pulses the pulse duration may be underestimated if only the width of the autocorrelation signal is considered. The more accurate methods of FROG and SPIDER are described below.

FROG

An extension of the method of autocorrelation that can retrieve the full temporal information of the laser pulse should also be mentioned here. The method of ‘‘Frequency Resolved Optical Gating’’ (FROG [22]) uses the basic setup of the interferometric autocorrelation with a SHG crystal. The photodiode is replaced by a spectrometer and the spectrum is measured for each delay. This generates a frequency resolved spectrogram of the laser

pulse, also known as a ‘‘FROG trace,’’. With the help of an algorithm, the FROG trace is evaluated to give the time-dependent intensity and phase of the pulse. The FROG-method is general, relatively simple to implement and has become a very successful technique with many accomplishments.

1.4.2 Spectral Interferometry

The method of ‘‘Spectral Interferometry’’ (SI) can retrieve the phase of a laser pulse—however, a reference pulse with known spectral properties is required.

To understand its principles let us assume that we have two pulses with identical spectra that travel collinearly with a fixed time delay τ . One of the two pulses is the reference pulse (pulse 1) with known spectral phase and amplitude. The other pulse (pulse 2) has experienced some kind of unknown modulation to its phase that we want to measure. If they travel collinearly their frequency components will interfere which leads to a complete modulation of the resulting spectrum with fringes separated by about $2\pi/\tau$. This fringe pattern also contains the phase difference of the two pulses. With the additional information of the original spectrum of one of the pulses, it will be simple to reconstruct the phase relationship for each frequency component based on their interference amplitude. Therefore the phase difference of these two pulses can be obtained.

A quantitative analysis of spectral interferometry is based on the Fourier transformation of the interferometric signal I_{SI} :

$$I_{SI}(\omega) = |E_1(\omega) + E_2(\omega)e^{-i\omega\tau}|^2, \quad (1.21)$$

where the phase delay $e^{-i\omega\tau}$ is due to the temporal delay τ between the modulated and the reference pulse. Now the two different single spectral distributions $I_1(\omega)$ and $I_2(\omega)$ can be detected separately and subtracted from I_{SI} . This leads to the interference term $S(\omega)$:

$$S(\omega) = I_{SI}(\omega) - I_1(\omega) - I_2(\omega). \quad (1.22)$$

With the definitions of the electric fields $E_n(\omega) = E_{n0}(\omega)e^{-i\Phi_n(\omega)}$ and $I_n = E_{n0}^2$ ($n=1, 2$) the interference term $S(\omega)$ can be written:

$$S(\omega) = [E_1(\omega)]^* E_2(\omega)e^{-i\omega\tau} + E_1(\omega)[E_2(\omega)]^* e^{i\omega\tau} \quad (1.23)$$

$$= 2\sqrt{I_1(\omega)I_2(\omega)} \cos(\Phi_1(\omega) - \Phi_2(\omega) - \omega\tau). \quad (1.24)$$

$S(\omega)$ contains the unknown phase $\Phi_2(\omega)$. We can now extract the phase difference $\Delta\Phi = \Phi_1(\omega) - \Phi_2(\omega)$ by Fourier transformation of $S(\omega)$. The result will be a signal that has nonzero components at $t = 0$ (DC-component, containing only the envelope of the signal that is of no interest to us) and at time $t = \tau$ and $t = -\tau$ (AC-component, containing the modulated carrier-wave). The phase information is contained in both components at τ and $-\tau$. We can now isolate the peak at $t = \tau$ and inverse Fourier-transform this signal. The phase difference can now be easily obtained from the argument of the result.

Again, the disadvantage of this method is that a reference pulse with known phase is needed. However, this method is ideal for diagnostic of single optics or complex new setups. Generally, an identical copy of a known (or unknown) pulse will be used. As the pulse passes the setup its phase will be modified. The phase-difference that is obtained can be measured by SI.

1.4.3 SPIDER

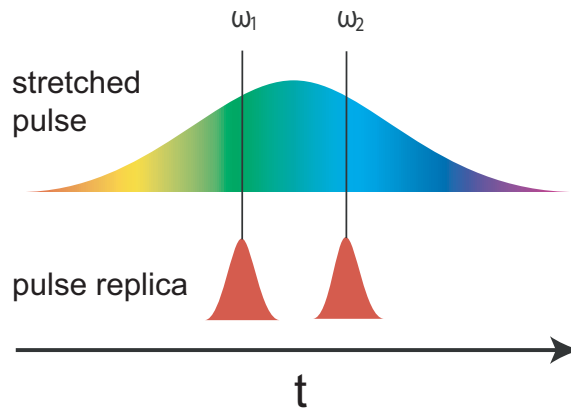


Figure 1.8: Realization of the spectral shear $\Delta\omega$ between two pulse replica used in SPIDER. Each of the pulses will be frequency mixed with a temporally chirped pulse at different frequencies.

The final method that will be described here is capable to completely reconstruct the electric field and is called "Spectral-Interferometry for Direct Electric-field Reconstruction (SPIDER)". In difference to the method of FROG no algorithm is needed—the field can be directly reconstructed from the measured data. This opens up the possibility to design setups for real-time pulse characterization up to 1 kHz repetition rate [23].

To be independent of a known reference pulse that is needed to retrieve the phase information of an unknown pulse—like in the case of SI—the SPIDER-setup was demonstrated by Iaconis and Walmsley [24] in 1998. Again, the basic idea is to create an identical copy of an unknown laser pulse for example with an interferometric setup (see Fig. 1.7).

In analogy to the description of SI, one of the two replica is again the reference pulse (pulse 1) and the other will get modified and analyzed (pulse 2). However, only the spectrum of the reference pulse will be known this time (can be measured independently)—its phase is unknown.

Now pulse 2 gets frequency shifted by a defined amount: the spectral shear $\Delta\omega$. Following relations are now valid: $I_2(\omega) = I_1(\omega + \Delta\omega)$ and $\Phi_2(\omega) = \Phi_1(\omega + \Delta\omega)$. The interferometric signal of pulse 1 and pulse 2 is again given by $I_{SI}(\omega)$ from Eq. (1.21) and for this case identified as SPIDER-spectrum $S_{SPIDER}(\omega)$:

$$I_{SI}(\omega) = S_{SPIDER}(\omega) = I_1(\omega) + I_2(\omega) + 2\sqrt{I_1(\omega)I_2(\omega)} \cos(\Phi_1(\omega) - \Phi_2(\omega) - \omega\tau). \quad (1.25)$$

The difference phase $\Delta\Phi(\omega)$ can be obtained by a SI-measurement (Section 1.4.2):

$$\Delta\Phi(\omega) = \Phi_1(\omega) - \Phi_2(\omega) = \Phi_1(\omega) - \Phi_1(\omega + \Delta\omega). \quad (1.26)$$

$\Delta\Phi(\omega)$ is close to the derivative of $\Phi_1'(\omega)$ for sufficiently small spectral shear $\Delta\omega$.

$$\Phi_1'(\omega) = \lim_{\Delta\omega \rightarrow 0} \frac{\Phi_1(\omega + \Delta\omega) - \Phi_1(\omega)}{\Delta\omega}. \quad (1.27)$$

Therefore, $\Phi_1(\omega)$ can be obtained by mere integration if $\Delta\omega$ is infinitesimally small. An infinitesimal small $\Delta\omega$ is, of course, experimentally not realizable. However, this basic idea of the reconstruction of the phase still works for all $\Delta\omega$ that will fulfill the Nyquist limit (Eq. 1.28) as described below.

The experimental realization of the SPIDER-setup used for this work includes a Mach-Zehnder interferometer to generate two replica of the laser pulse with variable time-delay τ . The above mentioned frequency-shift of one of the two pulses is realized by a frequency shift of both pulses. This is done by sum-frequency mixing those two pulses in a nonlinear crystal (BBO [25]) with a third pulse that is temporally chirped. As illustrated in Fig. 1.8 the two pulse replica, that travel collinearly with a delay τ , will temporally overlap with the chirped pulse at different frequencies. In the nonlinear crystal they will be sum-frequency mixed with those frequencies. This results in two up-converted pulses that have identical properties besides a frequency-shift of $\Delta\omega$.

For an ideal SPIDER measurement, the pulse duration of the temporally stretched pulse has to be large compared to the durations of the two pulse replica, so that they will interact with a defined frequency. The value of $\Delta\omega$ is chosen such that the Nyquist limit of sampling (Eq. (1.28)) will be fulfilled. At least two sample points are needed to resolve the SPIDER-fringe pattern. The spectrometer resolution for a given pulse delay τ therefore needs to be better than:

$$\delta\omega = \frac{\pi}{\tau}. \quad (1.28)$$

The SPIDER setup will be used to measure and to adaptively compress laser pulses in Chapter 2.

1.5 Femtosecond Pulse Shaping

The ability to control the temporal shape of electric fields is of great value. The nonlinear response of many quantum-mechanical systems often depends on its temporal evolution. On the femtosecond timescale of moving atoms exists no type of device that can directly shape the temporal amplitudes of the light pulses, but it is possible to influence their spectral properties.

The basic design of a femtosecond pulse shaper is easily described. The frequency components of the broad spectrum are spatially dispersed by a grating or prism and imaged onto a spatial light modulator (SLM) that is placed at the Fourier-plane of the setup. Those

devices are able to manipulate the light by variation of the optical path length (and therefore the phase) for light that is incident on their modulation area. In case of a spectrally dispersed pulse, the phase of different frequencies can be modulated. The dispersed laser pulse is afterwards recollimated and will have a modified temporal structure (see Fig. 1.9a for the basic setup working with a deformable mirror as pulse shaping device).

Without going into detail of the variety of possible setups, the working principle of the two different SLMs used for this work will be described in the following subsection. Their task is to manipulate the phase of the pulse in the spectral domain, while conserving the pulse energy. As today's SLMs are generally controlled electronically they are also addressable by computers. This opens up the possibility to implement complicated algorithms to iteratively adapt the control 'knobs' of the light modulators to experimental needs. One realization of such a control algorithm, an evolutionary algorithm, that has proven to be highly reliable, is found in the last subsection.

1.5.1 Pulse Shaping Devices

1.5.1.1 Deformable Mirror

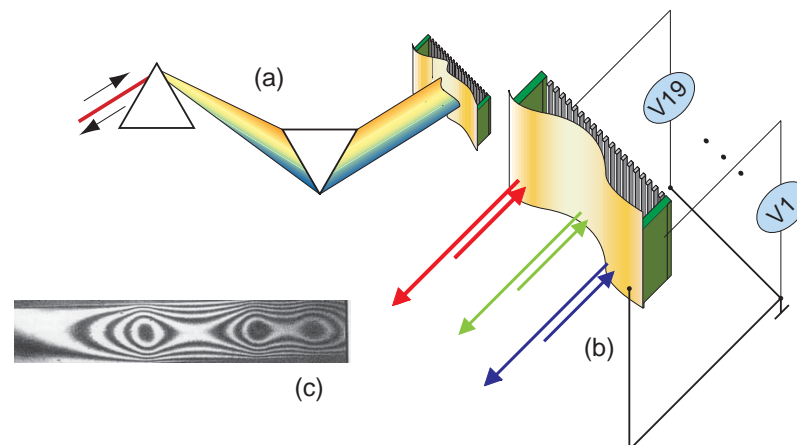


Figure 1.9: (a) Basic design of a deformable mirror pulse shaping setup. (b) Depending on the mirror's curvature the frequencies of spectrally dispersed pulses will travel different distances before they are recombined. This results in a temporally modulated laser pulse. (c) Interferometric image of the mirror's surface. A two-dimensional curvature is obtained by changing the voltage pattern of the linear array of 19 actuators placed behind the reflective membrane.

A very intuitive way for realization of a spatial light modulator is a mirror with a deformable surface. Depending on its curvature, light travels different distances when reflected at different positions (Fig. 1.9). The deformable mirror that was used for this work has 19 actuators that are placed linearly behind a gold coated reflective membrane. The maximum deflection is $7 \mu\text{m}$ which corresponds to a modulation depths of more than 8π at 800 nm .

Main advantages of this realization are the smooth surface that will reflect the full spectrum of a laser pulse with high efficiency. Deformable mirrors are relatively cheap and

have high reflectivity over a broad bandwidth. The actuators can be electronically addressed and have a fast response time of about 2 ms.

However, due to the mirror's curvature, sharp phase jumps are not realizable and therefore the effective resolution stays limited. Despite its design as a one-dimensional pulse shaping device the mirror's curvature will be two-dimensional leading to focusing or defocusing effects (Fig. 1.9c).

The deformable mirror will be used extensively in Chapter 4 to shape light pulses that control the process of high-harmonic generation. Even with the relatively low number of only 19 degrees of freedom a high level of control of this process can be achieved.

1.5.1.2 Liquid Crystal Display

Liquid crystal displays (LCDs) work on the principle that light passes a layer filled with liquid crystals that can be aligned by an external AC electric field. Depending on their orientation the optical path length for one polarization of the passing light is influenced. LCDs have therefore also the advantage that they can be used to realize a more complex polarization shaping setup [26, 27]. The active area of an LCD is divided into "pixels" that can be addressed independently. Between each pixel is a small gap that light cannot pass. This "pixelation" leads to unwanted pre- and postpulses of the order of few ps and also diffract the light [28, 29].

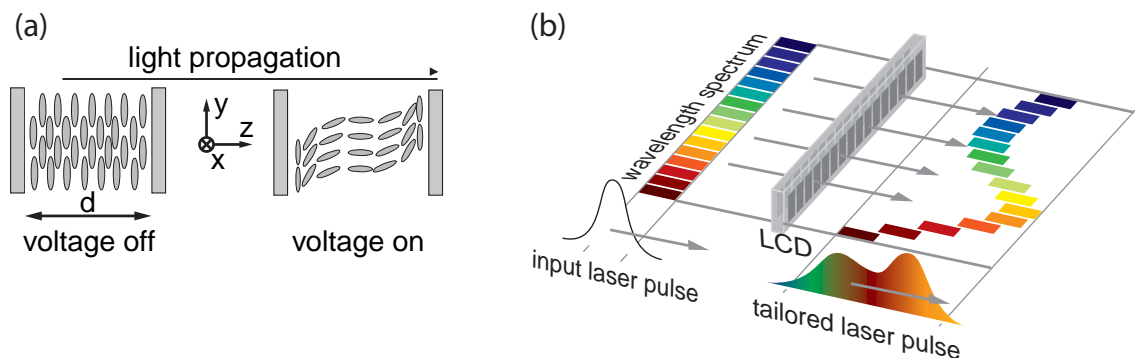


Figure 1.10: (a) By adjusting the voltages of the individual LCD pixels, the liquid-crystal molecules will be partly reoriented along the direction of the electric field. This changes the index of refraction for linear polarized light. (b) The index of refraction for different frequency components can be independently controlled in a temporal pulse shaping setup and laser pulses with specifically engineered temporal profiles can be generated.

The experiments of Chapter 2 use an advanced two-dimensional version of this type of pulse shaping device. The details are explained in Chapter 2 and especially in Appendix A.

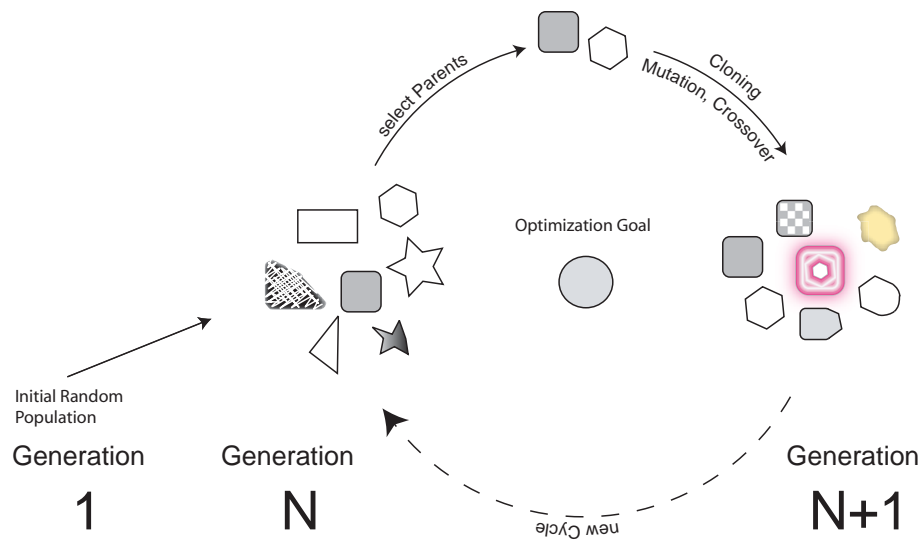


Figure 1.11: Illustration of the working principle of the evolutionary algorithm. The optimization goal for a population of colored shapes is the realization of a grey sphere. Starting with an initial random population (generation 1, N) two shapes that have the highest similarity to the optimization goal (high fitness) are chosen as parents. The next generation (N+1) consists of the unaltered parent-shapes (Cloning) and mutated versions (Mutation, Crossover). Then, again, new parent-shapes will be chosen... This process repeats until the optimization goal is reached.

1.5.2 Learning Algorithm

To determine the optimal parameter set for the spatial light modulator to optimally shape the light field can be quite an effort. By aiming to take advantage of the full resolution that the device can offer, there will be a tremendous amount of possible settings. In most cases the optimal pulse shape is unknown—often there is also no or insufficient information about the system under study. Even with such information it would be difficult to determine optimally shaped fields to control complex quantum systems and to realize such predictions under laboratory conditions. The simple brute force approach to test all possible pulse shapes will also ultimately fail due to the huge number of degrees of freedom in the system.

A solution to this problem is a feedback-looped algorithm to iteratively approach an optimum. This idea was originally proposed by Judson and Rabitz in 1992 [30]: a feed-back loop (or more appropriately, a learning loop) will allow the quantum system under study to determine which pulse shape best controls the system. The idea is based on the principle that different settings of the pulse shaping device will generate different experimental results. Unknown quantum systems are used as a kind of analog computer that calculates its own response to various input fields in real time. This response is evaluated and sent to an optimization algorithm as feedback. The algorithm decides what to do next, it “learns” from the feedback information. It will selectively modify the settings of the pulse shaping device and the new configuration is again tested in the experiment. The pulse shape will be iteratively adapted to the unknown system and optimize its response. A “clever” optimization algorithm can therefore asymptotically converge to an optimal set of parameters.

The optimization algorithm used for this work is an evolutionary algorithm. These algorithms are loosely based on the principles of biological evolution. The following is a short summary of the working principle in the case of a pixelated LCD device.

At the beginning of the optimization, we start with a number of random phase patterns of the spatial light modulator. Each pattern will shape the laser pulse and generate an experimental result. The phase patterns can be interpreted as a pool of individuals that are randomly initialized and then tested under experimental conditions. The phase values of the pixels are their genetic information—the phase of one pixel is a gene. The size of the pool, e.g. the amount of different phase patterns, determines the diversity of the genetic material.

The success of a particular individual is judged with respect to an optimization task determined by a fitness function. The fitness function is specifically designed to guide the algorithm to an optimum. The better the outcome of the quantum control experiment, the higher the fitness of the individual will be. After the fitness of all individuals from the pool has been obtained, a second generation of new individuals is generated by cloning, mutation and crossover operations on the genetic material of the previous generation. Depending on the quality of their genetic code (their individual fitness), only the best individuals from each generation are chosen to be transferred unaltered (cloned) to the next generation—they serve as parents. The rest of the individuals will get a certain percentage of randomly modified genes from those parents (mutation) or parts of the genetic material of different parent individuals (crossover)—they serve as “children” with new trial solutions. Therefore, the offsprings will generally inherit good traits from their parents and genetic variants appear that will prove to be well adapted to the environmental conditions. The new generation is then again tested for its fitness and—again—only the fittest will survive. Then another cycle of (natural) selection, reproduction and testing will start until the fitness converges to an optimum (see illustration in Fig. 1.11).

In this sense, the phase pattern of the pulse shaping device will adapt to the experimental conditions as a function of generation number and will become better suited to obtain an optimized experimental result. This algorithm will be applied for different pulse shaping devices in Chapters 2 and 4. It will be used to compress laser pulses in time close to their bandwidth-limit, optimize the output and control the shape of high-harmonic radiation.

1.6 Applications of Ultrashort Pulses

Ultrashort laser pulses have become a very versatile tool for a high number of applications. The short time structure allows time-resolved experiments on the time-scale of molecular vibrations. They are also very suitable for controlled laser ablation of materials and for delicate surgery in the eye. The pulses are not limited to the NIR spectral range. Additional optical setups like NOPA [31] allow the frequency conversion of the laser pulse into the visible range. Conversion to even much higher frequencies (into the XUV or soft-x-ray range [32, 33]) will be discussed in Chapter 3. Here, only a short impression of the many possible applications will be given that use these pulses as tools with high temporal and spatial precision and impressive peak power.

The broad spectrum of these pulses allows the excitation of a coherent superposition of vibrational modes in molecules. A vibrational wave packet is then generated in an excited state. With time-resolved pump-probe spectroscopy on the femtosecond time scale this wave packet can be probed at defined positions during its propagation along complex potential-surfaces [34, 35]. Its motion can be controlled and the outcome of chemical reactions influenced (coherent control [36–38]). This not only opens the way to control the outcome of chemical reactions, but also allows to gain more insight on the dynamics of quantum systems. This “problem of inversion” [39] is a very challenging task for more complex systems [40].

Using the technique of “multiphoton absorption confocal imaging” the spatial distributions of particular molecules can be determined even in a living cell [41]. This has many advantages compared to studies with UV-radiation as the femtosecond NIR-pulse will reduce damage of the tissue. This also helps during retinal surgery. Using a technique analogous to the ultrasound, a method of optical-coherence tomography with femtosecond pulses was developed that has permitted real-time imaging applications on micrometer resolution [42]. The depth information is obtained by measuring the “echo” time of backscattered light with interferometric methods.

The use of laser pulses in living organisms with delicate precision is complemented by brute force high power applications. At large laser facilities on-target intensities as high as 2×10^{21} W/cm² could already be achieved with peak powers reaching the petawatt level (10^{15} W) [43]. Within these fields electrons can be accelerated to relativistic energies (wakefield acceleration [44, 45]) and photon induced nuclear reactions can be observed [46, 43]. They can also provide temperatures and pressures comparable to those inside stars, permitting laboratory-based astrophysics.

Ultrashort laser pulses are also used as precision tools for micromachining, drilling, cutting and welding [47, 48]. The laser pulses turn the material into plasma instead of melting it and the energy is deposited too rapidly for the heat to diffuse into the surrounding unirradiated areas. Therefore, craters produced by femtosecond light-pulses possess well-defined boundaries indicating sharp ablation thresholds on the nanometer scale. Smooth features with high precision are generated compared to alternative methods.

Highest precision is also found in the time domain. The Nobel prize in physics 2005 was awarded to John L. Hall and Theodor W. Hänsch “for their contributions to the development of laser-based precision spectroscopy, including the optical frequency comb technique”. Optical frequency combs are generated by trains of broadband femtosecond pulses with a fixed carrier-envelope phase to each other [49]. The pulse train from the time domain can then be found also in the frequency domain (frequency comb). This comb of well defined frequencies can be used as “optical ruler” to measure unknown frequencies with unprecedented precision. This is achieved by acquiring the “beating signal” of an unknown frequency to a close-lying frequency of the comb. From this measurement the unknown frequency can be determined with the highest precision.

Chapter 2

Adaptive Temporal Compression of Ultrashort Laser Pulses

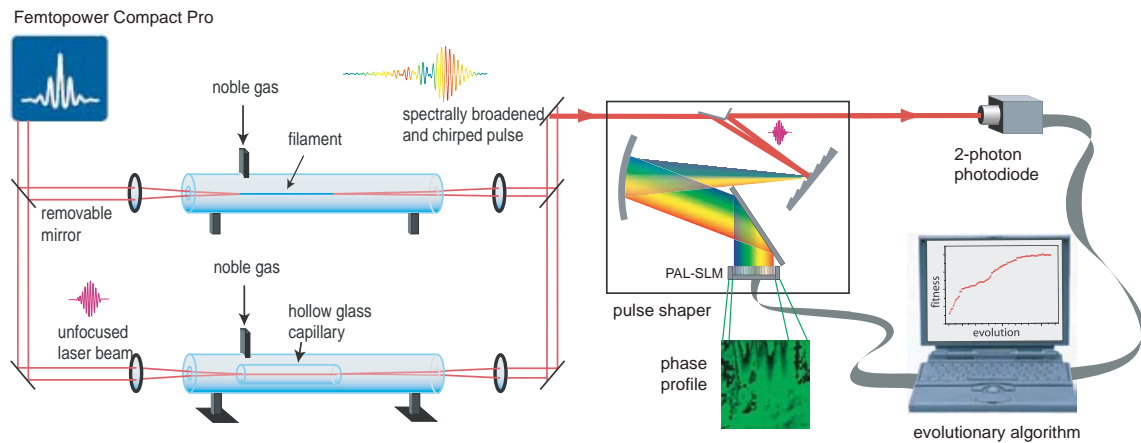


Figure 2.1: Optical setup for adaptive compression of ultrashort laser pulses. 30 fs output pulses of the Femtopower laser system are spectrally broadened in a hollow fiber setup (lower configuration) or by filamentation (upper configuration). The spectrally broadened pulses are afterwards temporally compressed in a pulse shaping setup. The feedback for the evolutionary algorithm that controls the compression process is given by the photocurrent of a two-photon photodiode.

This chapter will be focused on experimental results of compression of ultrashort pulses in different pulse shaping setups. Ultrashort pulses will be important for the efficient generation of high-harmonics discussed in the next chapters.

A two-dimensional spatial shaping device will be used in a temporal and spatiotemporal pulse shaping setup. An advanced implementation of the evolutionary algorithm was developed that converges at high resolution to an optimum of the fitness on a small time scale. The main purpose of this pulse shaping setup is efficient temporal compression of spectrally broadened laser pulses. It will be important, that the optimum of the pulse shape is found fast to speed up experimental work and to keep the effects of laser fluctuations over longer timescales as low as possible.

In the following paragraphs the pulse-shaping setup and the advanced version of the evolutionary algorithm are introduced. Pulse compression with different configurations for

spectral broadening will be examined in the following sections. In Section 2.1 a hollow-fiber setup will be used for spectral broadening. Section 2.2 introduces spectral broadening in filaments as alternative technique with much higher throughput of laser power. Fig. 2.1 gives an overview of the basic experimental setup. For the experiments of this chapter the Femtopower laser system was used (see Section 1.2).

Two-dimensional Temporal Pulse Shaping Setup

A two-dimensional version of a LCD-based pulse shaping device is used for the following experiments that is placed in a specifically designed pulse shaping setup. The two-dimensional spatial light modulator (Hamamatsu Photonics PAL-SLM, X8267 [50]) works in a reflective mode with an active area of $20 \times 20 \text{ mm}^2$ (reflectivity $\approx 90\%$). Inside the PAL-SLM is a two-dimensional liquid-crystal display (LCD) with a usable area of 768×768 pixels working as a pixel mask controllable by an XVGA signal from a computer. By means of a built-in laser diode this pixel mask is imaged onto the backside of the active area. As a consequence, the refractive index changes for linearly polarized light impinging on the front side (read light) depending on the intensity of the laser diode light (write light) [51]. The phase-modulation depth for 800 nm is about 3π (Fig. A.2). The imaged LCD pattern is blurred by about 2-3 pixels. Due to this smoothing there are no gaps between neighboring pixels and therefore no “pixelation”-effects (see Section 1.5.1.2). However, this blurring has the disadvantage that no sharp phase jumps (e.g. phase jumps of 2π) can be realized without the appearance of steep phase gradients that will deflect part of the laser beam. The implementation of the evolutionary algorithm described below, allows the optimization to phase profiles with a smooth surface, but phase jumps of 2π , that are necessary to realize a modulation depth of more than 3π , will still distort the beam (see also Appendix A).

To use the PAL-SLM as temporal shaping device a compact zero-dispersion grating compressor setup was designed [52]. The laser beam is spectrally dispersed with a 300 l/mm gold-coated grating and then focused on the active area of the PAL-SLM by a cylindrical concave mirror (focal length of 30.0 cm) in a $2f$ configuration. The use of a grating instead of a prism allows for a more compact design. All optics are placed on a transportable breadboard ($60 \text{ mm} \times 45 \text{ mm}$). The pulse shaping setup is designed to be able to modulate a bandwidth of up to 200 nm around the central wavelength of 800 nm supporting bandwidth limited pulses of about 10 fs. The throughput of the whole setup was measured to be about 60%. Generally, a suitable attenuator was placed in front of the pulse shaping setup to avoid beam distortions caused by nonlinear effects in the modulation area of the PAL-SLM (see Appendix A). This setup will later be modified to allow temporal AND spatial shaping of laser pulses. The realization is rather simple as the unmodified laser beam just has to hit the front of the PAL-SLM a second time (before or after it enters the $2f$ configuration for temporal modulation).

Evolutionary Algorithm for a Large Number of Degrees of Freedom

The phase of each of the 768×768 pixels of the PAL-SLM can be set in a range of 0 and 2π with a stepsize of $\pi/100$ at 800 nm. To take advantage of the full resolution of the device is problematic as the evolutionary algorithm will not converge on a reasonable

time scale if the number of degrees of freedom is that large. Reduction of the complexity of the system by working with quadratic arrays of pixel blocks with identical phase values will reduce resolution.

The following implementation was realized: The optimization starts with a low number of degrees of freedom that is adaptively increased during the process. In the beginning all pixels of the spatial light modulator are grouped to one big quadratic array of pixels to work as a plane surface. These planes can be tilted to better adapt to the optimization problem and they will be subdivided into smaller parts to successively increase the resolution (for a more detailed description see Appendix B or [53]).

2.1 Temporal Compression in a Hollow Fiber Setup

A hollow-fiber setup was designed to be able to spectrally broaden laser pulses [54]. By confining the laser inside a gas-filled fiber the length of nonlinear interaction with the gas will be increased. As a consequence the spectrum gets broadened by self-phase modulation (see Section 1.3.2). Hollow-fiber setups are widely used to generate broadband laser pulses as they generally produce laser pulses of high spatial quality [55]. However, part of the energy is lost during propagation as hollow fibers are unable to confine the full beam by total reflection (“lossy” waveguides [18]). Highest losses are experienced by higher order fiber-modes. Propagation inside hollow fibers will therefore filter the spatial profile of laser pulses. Over-one-octave broad spectra can be generated in the visible and the subsequent compression of pulses to durations shorter than 4 fs could already be demonstrated [56, 57]. By exploiting ionization effects even self-compression of intense laser pulses during propagation through a short hollow fiber setup could be observed [58].

The hollow fiber used in this chapter has a length of about 70 cm and an inner diameter of 267 μm and was filled with argon. The fiber throughput was measured to lie between 35 and 55% of the beam energy of the input pulse. The losses are partly attributed to imperfections of the hollow fiber. Additional 10 to 20% of the energy were lost by aperturing the central part of the beam profile. Using argon-gas pressures of about 300 mbar, output spectra with a FWHM of 100 to 150 nm could be obtained (Fig. 1.6b).

The spectrally broadened laser beam passes the pulse shaping setup and is afterwards analyzed in a Michelson-based interferometric autocorrelator (see Section 1.4.1). The position of one arm of the setup was controlled by a piezo-motor at a spatial resolution of about 40 nm. The autocorrelation signal is detected with a GaAs photodiode which can only detect two-photon transitions for a wavelength range between 700 nm and 900 nm. A concave mirror with a focal length of 1.5 m is used to slightly focus on the photodiode. As feedback signal for the evolutionary algorithm the signal of the two-photon photodiode was used. During each optimization one arm of the autocorrelator was always blocked to suppress signal fluctuations by interference effects. As reference signal the two-photon signal for a flat phase profile on the PAL-SLM was used.

Due to dispersion effects in the autocorrelator setup (the beam has to pass a 2 mm fused-silica beam-splitter 3 times) the time structure of the beam will be changed. However the introduced linear dispersion of the material can be easily compensated by slight adjustment of the grating compressor of the pulse shaper and will not be accounted for in the

compression experiments.

2.1.1 Temporal Compression

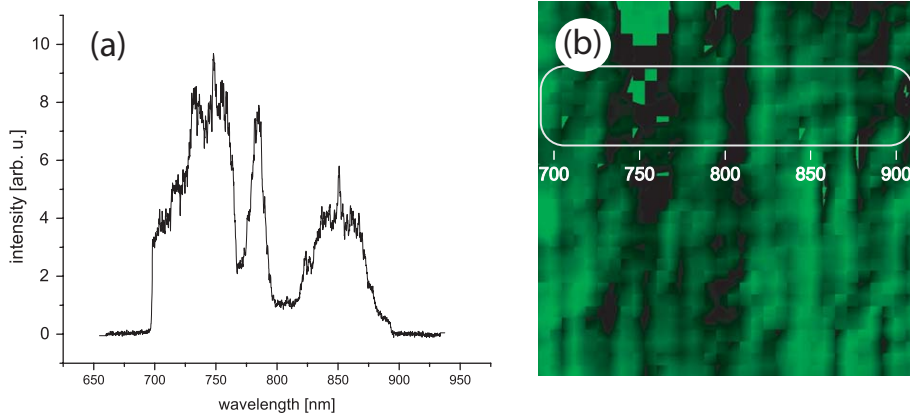


Figure 2.2: (a) Spectrum of the broadened laser pulses after passage of the pulse shaping setup. It has a non-Gaussian shape with two major spectral holes leading to small sidewings of bandwidth limited pulses. (b) Modulation area of the PAL-SLM at the end of the compression optimization. Though the two-dimensional area is subdivided into a matrix of 32×32 tiltable planes at the end of the optimization, the horizontal degrees of freedom were favored as the resolution was increased during the optimization. This results in a stripe-like structure. The white box indicates the area on which the spectrally dispersed laser pulse hits the SLM.

For efficient compression of laser pulses, that were spectrally broadened inside hollow fibers, generally no pulse shaping device is mandatory. Near bandwidth limited pulses can be achieved using simple prism- or grating compressors or chirped mirrors [59]. The use of specifically designed chirped mirrors for compression achieves impressive results but they are limited to compensate specific phase-functions. Using a prism pair to temporally compress the hollow-fiber output pulse was already investigated [54], with limited success. The spectral phase could not be completely flattened, i.e. the pulse compressed. Therefore, the temporal pulse shaping setup is chosen for adaptive compression.

The first optimization results were obtained using the pulse shaper in its original zero-dispersion configuration [54, 52]. The modulation area was divided into a one-dimensional array of 100 columns of grouped pixels. The optimization results demonstrated that this configuration can correct the overall quadratic chirp [54, 52]. The shortest pulse duration was measured to be 25 fs after compression laser pulses with a spectral bandwidth of about 125 nm. As explained more detailed in Appendix A the grouping of pixels to act as a block (or stripe in this case) with uniform phase value has the problem of sharp phase jumps that generally occur between neighboring pixel-blocks. As the pulse shaping device had to compensate the full amount of quadratic chirp the optimized phase profile also consisted of a number of 2π phase jumps.

Each phase jump introduces a steep phase gradient due to the smoothing effect of the PAL-SLM. This phase gradient will deflects part of the beam.

Therefore, tiltable planes were implemented in the evolutionary algorithm that can prevent

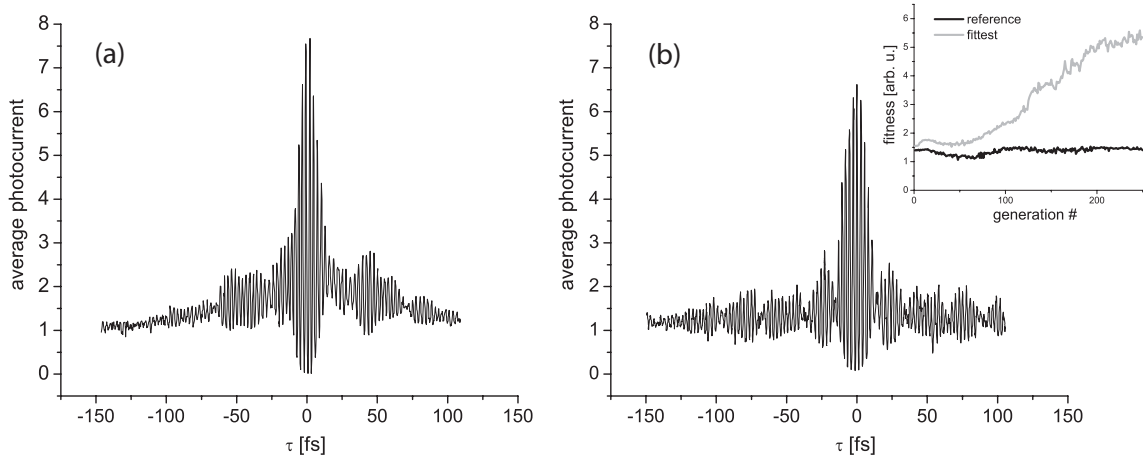


Figure 2.3: Interferometric autocorrelation traces of the laser pulses before (a) and after (b) adaptive compression. The overall chirp could be reduced and pulse durations of around 11 fs are obtained. The inset of (b) presents the evolution of the fitness during the optimization (black: maximum fitness, grey: fitness of reference pulse shape).

this behaviour (see Appendix B) and the overall quadratic chirp was precompensated with the grating compressor. Prior to each optimization the coupling into the hollow fiber was adjusted for highest throughput and homogeneous beam profile of the output pulse. The gas pressure was chosen to spectrally broaden the laser pulses to a bandwidth of about 100 to 125 nm (Fig. 2.2a). The cylindrical mirror of the pulse shaping setup was adjusted for the highest signal on the two-photon-diode with a flat phase on the PAL-SLM. This was used as reference signal (Fig. 2.3a). In Fig. 2.3a one still can see a high amount of quadratic chirp, which results in a so-called “wing” structure, however the signal-peak in the middle is already very short (about 7 oscillations corresponding to a duration of about 10 fs). The pulse shaper should be capable to remove this chirp while keeping the pulse duration as short as possible.

The population size for the evolutionary algorithm was reduced to only 10 individuals per generation. This accelerated each optimization to finish in about 30 minutes to a few hours but will limit the probability to reach a global optimum. Reduction of this parameter was essential as the laser started to drift considerably on the timescale of hours (more on this subject below). As already explained above, the modulation area of the PAL-SLM was subdivided into an array of quadratic tiltable planes. Their numbers could be increased during the optimization to increase the resolution. Laser pulses are spectrally dispersed on the horizontal axis but still have a one dimensional spatial component in the vertical direction that can be modulated independently for each wavelength. Therefore the “temporal”-pulse shaping setup will also shape the vertical spatial component of each frequency. However, to better distinguish this more basic setup from the modified version used in Section 2.1.2 and 2.2.3, in which the additional modulation of the two-dimensional spatial profile of the laser pulses is included, it will be further denoted as “temporal”-shaping setup.

The result of the temporal optimization is presented in Fig. 2.3b. The wing structure is gone (i.e. the remaining quadratic chirp was compensated) and the measured phase is very flat compared to the autocorrelation of the reference signal. The corresponding

optimized phase profile on the modulation area of the PAL-SLM is shown in Fig. 2.2b. The approximate area on which the spectrally dispersed laser pulse hits the modulation area of the PAL-SLM is indicated by a red box. The signal-peak in the middle slightly broadened resulting in a pulse of about 11 fs. The inset of Fig. 2.3b presents the evolution of the fitness values. Shown are the maximum fitness (black) and the reference value (grey).

Experimental Difficulties

Even after minimizing the convergence time of the adaptive optimization setup, a slow laser drift and power fluctuations prevented successful optimization runs most of the time. A slow vertical drift of the laser changes the coupling efficiency into the fiber. Therefore, higher order fiber modes can get excited. This will reduce the laser throughput and the amount of spectral broadening. Stronger laser drifts may even damage the fiber entrance. In most cases the pulse shaper was not able to adapt to this slow change and the measurement had to be aborted before an optimum could be found. The source of this drift was presumably temperature related and could not be circumvented. To compensate this drift the first mirror of the periscope outside the laser amplifier was substituted by a piezo-motor-controlled version. Two piezo-motors can control both tilt angles of the mirror and are addressed by a computer [60]. The reflection of a beam-splitter was used to get the feedback for the tilt angles of this mirror. It was imaged onto a CCD-camera and evaluated by the computer that controls the mirror tilt angles.

This small compensation setup could indeed fix the position of the laser reflex on the CCD-chip of the camera, however by controlling only one mirror a laser beam cannot be fully aligned. The adaptive drift-compensation worked well enough to keep the laser focus always inside the fiber entrance hole, however, now the coupling-angle still slowly drifted. As a consequence the throughput power and the output spectrum still varied on timescales of about one hour.

There also was another problem with this stabilization setup: everytime when the laser spot on the CCD-camera drifted out of a predefined threshold region (see [60]) the mirror tilt-angles were automatically adjusted to direct it back to its original position. This was realized by a stepwise change of the tilt-angle of the mirror under control. If this correction-step happened during an optimization run, the fitness might have been influenced slightly for part of the individuals of a generation. This disturbs and slows down the optimization process.

A possible solution might have been a trigger signal of the evolutionary algorithm after it has finished data collection for one generation. Control of both mirrors of the periscope should allow to fully compensate any kind of drift—however, the output power of the laser system still slowly drops over time (This power loss could be again compensated with a tunable attenuator for a certain amount of time).

The alternative solution of manual readjustment of the laser system after a small number of generations proved to be most effective. After a power drift, the laser system had to be realigned to increase its output power to the reference value of the start of an optimization. A similar effort was necessary for vertical drifts of the laser. The spatial profile and the spectral output had to be readjusted to reference values obtained at start-up.

2.1.2 Spatio-temporal Compression

Due to the vertical laser drift the spatial profile of the laser pulse changed slowly as a function of time. This is caused by excitation of higher-order fiber modes and therefore different intensity distributions inside the fiber. The spectrally broadened output pulse then has a more complex spatial intensity profile. Different frequency components can travel in different fiber modes leading to spatial chirp after the laser pulse exits the fiber. To compensate these spatial distortions, the shaping capabilities of the setup were extended to additionally include shaping of the full two-dimensional spatial beam profile (see proposed setup in [52]). The flexible parameterization of the modulation area of the PAL-SLM makes the device independent of where and how often the laser will hit. Thus it can be used to shape a single laser pulse multiple times.

The lower half of the active area of the PAL-SLM is now used for spatial shaping while the upper half can modulate the spectral phase the same way as described in the previous section. The throughput of the setup was reduced to about 50%. Due to geometrical reasons, the laser spot that hits the PAL-SLM for spatial shaping, is centered near the left edge of the modulation area (Fig. 2.5a).

The evolutionary algorithm tries to find the best phase profile in the “spatial section” of the modulation area, that will lead to the highest signal on the two-photon photodiode. It will therefore start to focus the beam to a small spot-size on the two-photon diode and therefore increase the detected photocurrent. This smaller spot size can increase the measured photocurrent to saturation. Therefore, additional attenuators have to be employed and the signal-to-noise ratio will be decreased. To prevent this behavior an additional iris-aperture was placed at the original focus position of the detection setup. This fixed the position of the focus in space and prevented additional focusing of the spatial section of the PAL-SLM.

In the first realization of the spatiotemporal pulse shaping setup the laser beam was spatially modulated before it was temporally shaped. An optimization of the spatial section alone resulted in an increase of the photo-current without reduction of the pulse duration as explained above.

Using the spatial and the temporal section for optimizations was not successful in first runs. The stability of the algorithm was reduced: A change of spatial profile of the laser pulse in the spatial section (for example reflection under a slightly different angle) influenced the positions of the spectrally dispersed beam in the temporal section of the modulation area. Therefore, the temporal part of the optimization could not produce any reasonable results as the frequency positions on the modulation area were no longer fixed.

Therefore the setup was changed to perform spatial shaping AFTER temporal shaping. The progression of optimization worked best if only one section (spatial or temporal) was allowed to vary for a number of generations while the other section was kept at fixed phase values (mutation rate = 0).

Fig. 2.4a shows a broadened spectrum with a bimodal distribution that proved to be very suitable for optimizations over long timescales. By realignment of the laser amplifier and manual compensation of spatial laser drift in certain time intervals (~ 30 min) to reproduce the spectrum of Fig. 2.4a an optimization with a number of more than thousand

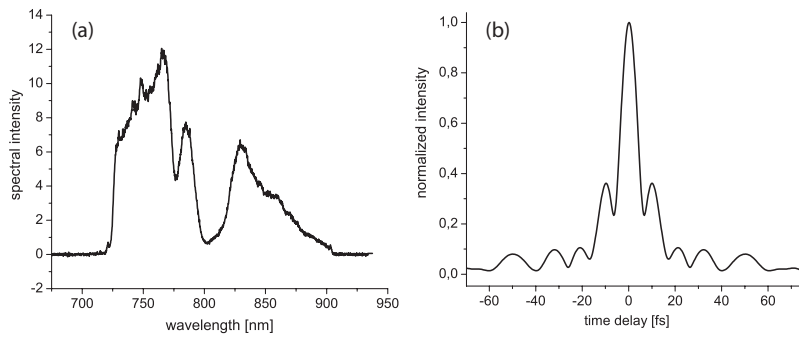


Figure 2.4: (a) Spectrum of the broadened laser pulses after passage of the pulse shaping setup. Due to a bimodal structure the corresponding temporal intensity distribution of the bandwidth-limited pulse (FWHM of about 9 fs (b)) has small sidewings.

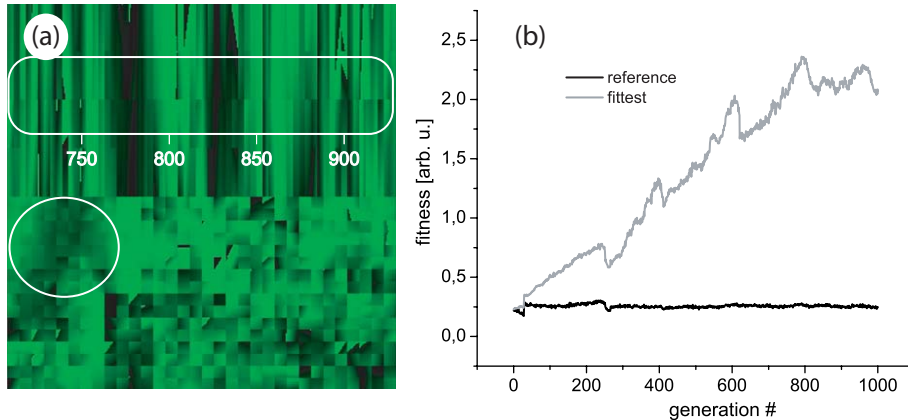


Figure 2.5: (a) Optimized two-dimensional phase profile of a spatio-temporal minimization of the pulse duration. The spectrally dispersed laser pulse hits in the indicated region in the upper section of the modulation area, while the two-dimensional spatial profile of the laser pulse is modulated in the lower section. (b) The corresponding fitness curve reveals a step-like structure that is attributed to a set of suboptimal parameters of the evolutionary algorithm after an increase of the number of degrees of freedom of the system (see Appendix B).

generations was possible (running time ~ 7 hours).

Fig. 2.5 presents the evolution of the fitness during the optimization process. Most striking features are a number of drops of the fitness value followed by a steep rising fitness. This behaviour is caused solely by the parameters of the evolutionary algorithm. Every time after the number of genes of the spatial or the temporal section was increased (number of tiltable planes doubled in x , or y -direction) the fitness started to drop and recovered after a number of generations.

This result was surprising at first, but can be explained. In Section 2.2.3 a similar optimization was performed without this feature in the evolution of the fitness. The main difference between the optimization parameters in these two runs is the amplitude of the maximum deviation during the mutation process (see Appendix B). For Fig. 2.5 a fixed mutation deviation of 100 was used, while the mutation deviation in Section 2.2.3 was manually reduced every time after the number of degrees of freedom was increased.

The mechanism that causes the fitness to drop is closely connected to the limited number

of only 10 individuals per generation and short-time fluctuations of the laser intensity and photo-current as described in Appendix B. In principle, the level of mutation rate was too high after doubling of the degrees of freedom. It had to be manually lowered to stop signal degradation.

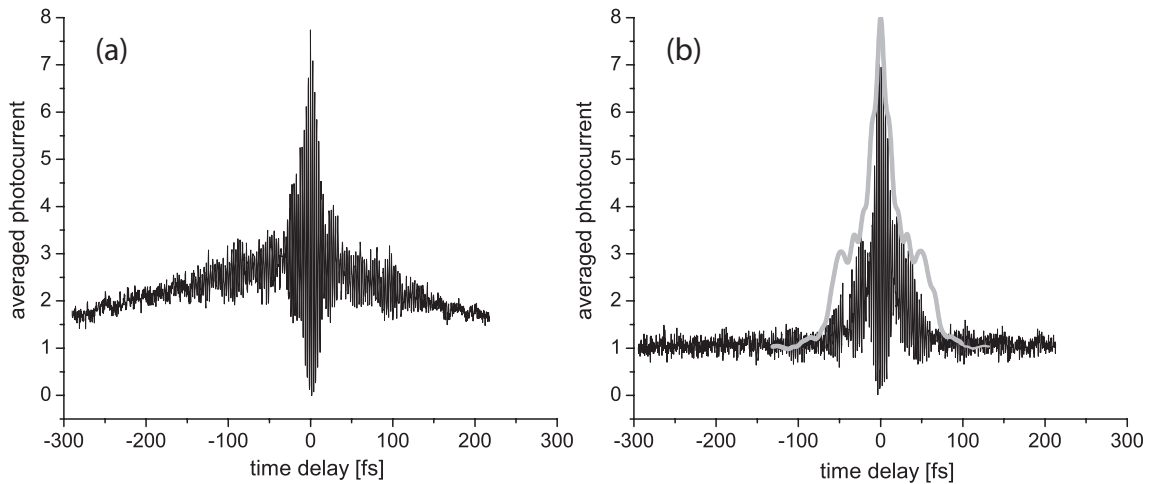


Figure 2.6: Interferometric autocorrelation traces of the laser pulses before (a) and after (b) spatio-temporal compression. The overall chirp could be reduced and pulse durations of around 11 fs are obtained. The grey line in (b) gives the calculated envelope of the autocorrelation trace using the bandwidth-limited pulse of Fig. 2.4. The difference to the experimental data is attributed to remaining spatial chirp of the optimized pulse that appears to be compressed near to its bandwidth-limit.

Fig. 2.6 gives the comparison of the autocorrelation of the reference (Fig. 2.6a) with the fittest pulse shape (Fig. 2.6b). The remaining quadratic chirp (wing structure of Fig. 2.6a) was again removed and the pulse duration could be reduced near to its bandwidth-limit. Fig. 2.4b shows the calculated intensity distribution of the bandwidth-limited pulse of the spectrum of Fig. 2.4a. This pulse has a FWHM of less than 9 fs. Due to the bimodal structure of the spectrum small sidewings are present. This pulse was used to calculate the envelope of the interferometric autocorrelation (grey line in 2.6b). A comparison to the measured autocorrelation nearly implies that the fittest pulses might even be shorter compared to the bandwidth-limited case. However, remaining spatial chirp smoothes interferometric signals and the amplitude of oscillations will be lowered. Therefore, the measured interferometric autocorrelation signal will generally have lower oscillation amplitudes than theoretically expected. The FWHM of the interferometric autocorrelation gives only a rough estimate of the pulses duration and is about 11 fs.

In the following section spatial shaping experiments will play a more dominant role (especially in Section 2.2.5). However it should be noted here that spatial modulation of a broad spectrum is problematic with LCD-based devices as only the wavelength-dependent refractive index of the material can be controlled. Different colors will experience a different amount of phase shift and cannot be influenced separately.

Conclusion

Pulse compression of laser pulses that are spectrally broadened in a hollow fiber setup

could be successfully demonstrated. Pulse compression seems to be not limited by the pulse shaping setup, but depends strongly on the initial spectral distribution and the stability of the laser system. Under ideal conditions spatial chirp of laser pulses was low and near bandwidth-limited pulses of around 11 fs have been obtained. A more detailed study of the spectral broadening mechanism using for example a mixture of different gases can be helpful for the generation of Gaussian-shaped spectra with bandwidths up to 150 nm.

2.2 Temporal Compression by Filamentation

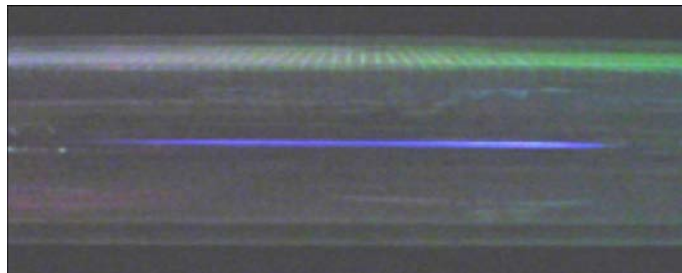


Figure 2.7: Plasma-recombination light of the 20 cm long plasma channel of a filament.

The hollow-fiber setup for spectral broadening, that was described in the previous section, provided spectra that could be compressed down to 11 fs. However, part of the intensity will always be lost during the conversion process inside the lossy waveguides [18]. It is also challenging to stabilize the laser system to be able to efficiently couple into the waveguide structure over longer time periods. Due to propagation of pulses with high peak power the waveguide structure can deteriorate slowly over time and has to be replaced.

Another promising method for spectral broadening is the generation of self-induced filaments (Fig. 2.7) that are generated by intense laser pulses as they propagate through gas filled cells [15,61]. Filaments are the result of an interplay between the optical Kerr effect (see Section 1.3) which leads to self-focusing and the defocusing effect of a low-density electron plasma that is generated at high intensities (Fig. 2.8). These two effects can cancel each other and a 'filament' is formed. In this case, the laser pulse forms its own plasma channel (diameter of about 100 μm) that keeps field intensities high enough to broaden its spectrum while traveling nearly lossless over long distances [20]. Laser pulses traveling inside filaments can even modify their temporal structure and self-compress [62]. Using a setup with two gas cells for filamentation laser pulses as short as 5.1 fs have already been demonstrated [63].

In analogy to the previous section, pulse compression experiments will be performed on the broadened output pulses of filaments with the pulse shaping setup. In addition to a temporal and spatiotemporal optimization of the pulse duration, Section 2.2.4 uses the phase of the broadened laser pulses, that is measured with a SPIDER-setup, for negative phase feedback. The last subsection includes a spatial modulation of laser pulses prior

to filamentation to optimize the filamentation process with respect to reduction of spatial chirp of the output pulses.

2.2.1 Generation of Light Filaments

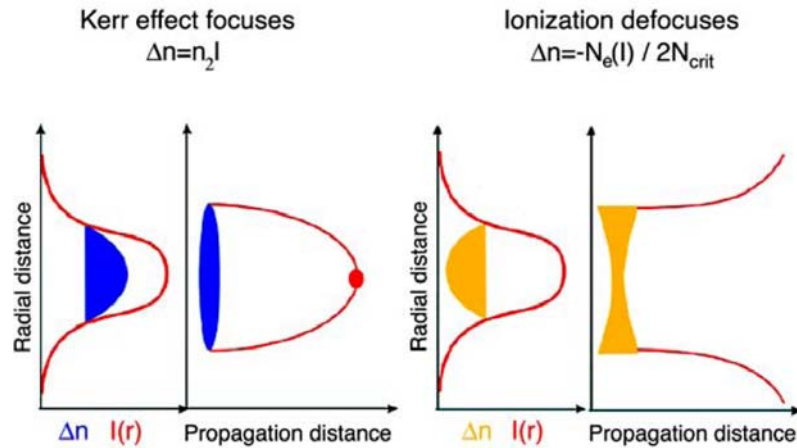


Figure 2.8: Mechanism for the formation of a plasma channel [64]. The effect of self-focusing is compensated by the defocusing effect the generated plasma distribution.

To generate a light filament a second gas-filled tube with anti-reflection coated windows was built. The tube had a length of about 1.7 m and was filled with argon gas. To obtain ideal conditions for the generation of a filament, a range of different focusing optics was tested while the gas pressure inside the gas cell was varied [65]. The laser was tuned to deliver pulses with 0.9 mJ. Careful study of the results revealed different regimes of pressure for each focal length for the generation of one single filament and multiple filaments.

Depending on the beam profile of the incoming laser pulse multiple filaments are generated if the laser power is much higher than the critical power P_{crit} (Eq. 1.13), with higher values for homogeneous beam profiles [66]. Irregularities in the beam profile will be enhanced during self-focusing and multiple filaments can be started at different positions [67]. Even flat-top pulses can break into multiple filaments as the maximum power that one filament can sustain is limited [68] and usually on the order of P_{crit} for each filament.

So-called “parent” and “child”-filaments travel next to each other and compete for energy [69,70]. They may even fuse together and split up again [71]. The different parts of the laser pulses traveling in different single filaments will generally experience individual amounts of spectral broadening due to self-phase modulation as laser intensities can vary in each of the single filaments of the multifilament. This will lead to a high amount of spatial chirp at the end of the multifilament. Parts of the output “beam” will have different divergences, spectra and phase structures (Fig. 2.9b). Those “beams” cannot be temporally compressed as a whole—multifilamentation is to be avoided.

There also exists a significant broadening of the angular spectrum dictated by the spatial variations of the pulse phase during filamentation. These variations are responsible for

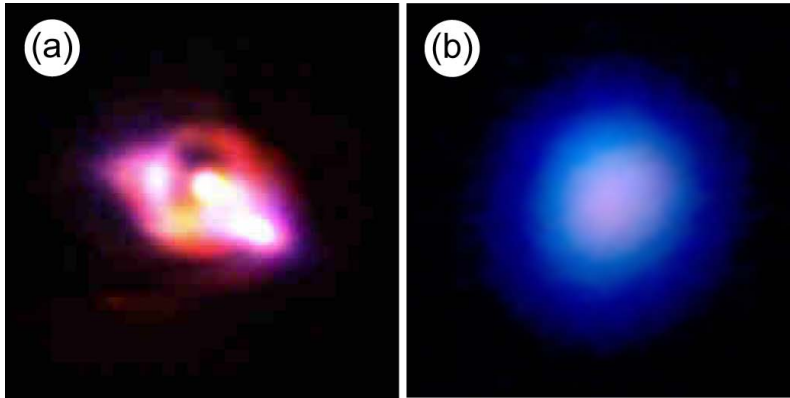


Figure 2.9: Pictures of the laser beam taken with a color CCD camera with IR-filter after it exits the gas cell. (a) Inhomogeneities of the initial laser beam profile and high laser intensities lead to the generation of multiple filaments and a high amount of spatial chirp can be observed in the beam profile of the output pulse. (b) Homogeneous beam profile of a single filament. The only visible spatial chirp is distributed radially and due to conical emission during propagation along the filament [15]. The radial symmetry is high and the beam profile looks rather homogeneous.

conical emission (CE) [15, 72] through which the beam diverges as a concentric rainbow with colors ranging from red to blue. These effects can be seen in the beam profile of Fig. 2.9b. The highest visible frequencies (blue) have the largest angular divergence.

Ideal parameters for filamentation were found for a focal length of 1.5 m, pulse energies between 0.6 and 0.7 mJ and gas pressures between 0.8 and 1.5 bar [65]. The pulse intensity and gas pressure were determined experimentally every day to generate a single filament with a length of about 15 cm. The power throughput was measured to be above 93%. For the following compression experiments laser pulses with a bandwidth of usually about 150 nm were generated.

In comparison with the hollow fiber setup filaments are independent of small drifts of the laser position. Only dropping laser power had to be readjusted every few hours. Due to the high energy throughput of the filament and low divergence of the output pulse the first optics after the exit of the filament tend to get damaged (especially any kind of attenuators that had to be used to protect the sensitive modulation area of the PAL-SLM (see Appendix A).

As explained above, the filamentation process is very sensitive to the spatial profile of the incoming laser pulse. Inhomogeneous pulse profiles will cause a high amount of chirp (Fig. 2.9a) or indications of multiple filaments [65]. This sensitivity seems to be the main drawback of this technique.

2.2.2 Temporal Compression

To integrate the filament into the existing pulse compression setup the gas-tube with the hollow-fiber was simply replaced by a longer gas-tube for generation of a filament. The pressure inside the argon-filled tube was set to 1.2 bar to broaden the spectrum to a FWHM between 100 and 150 nm. Similar to the hollow-fiber setup only the central part of the

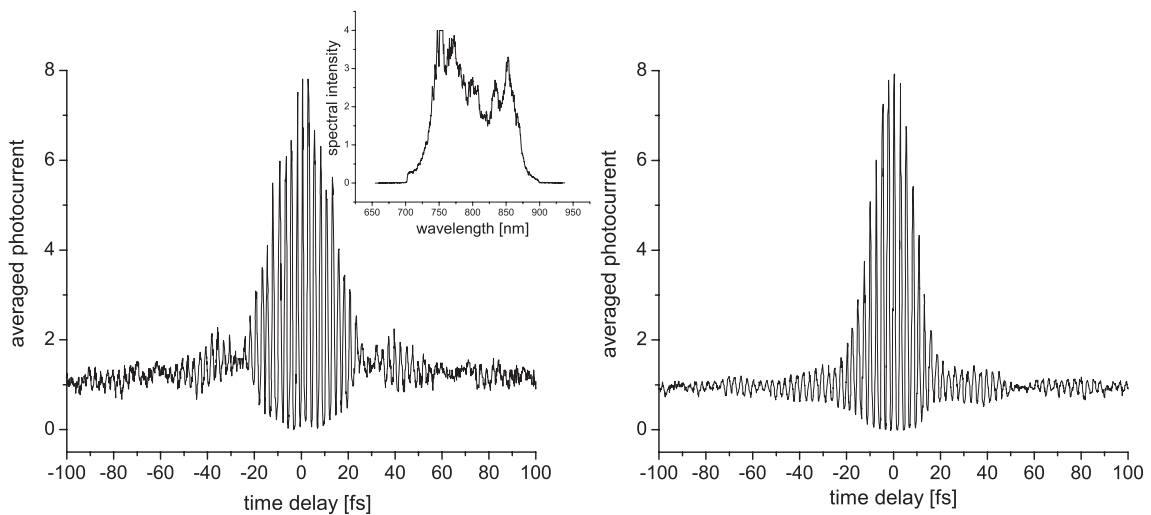


Figure 2.10: Interferometric autocorrelation traces of the laser pulses before (a) and after (b) adaptive compression. The overall chirp could be reduced and pulse durations of around 13 fs are obtained. The inset of (a) shows the spectrum of the output pulse of the filament.

output pulse was used for compression containing about 80% of the energy.

Simple compression using a grating or prism compressor were disappointing as only autocorrelations with low peak to background ratio could be obtained (lower than the 8:1 ratio for interferometric autocorrelation). This was attributed to spatial chirp that was still present in the apertured beam profile. Spatial chirp partly “smears out” oscillations of a interferometric autocorrelation. This problem could not be solved until the beam profile of the incoming laser pulse was optimized in Section 2.2.5. Until then, only small areas in the middle part of the beam were used for optimizations. Especially closing iris apertures in front of the autocorrelator-setup can improve results.

For optimizations the grating-compressor was adjusted to yield the maximum photocurrent on the photodiode for a flat phase profile on the PAL-SLM. As can be seen in Fig. 2.10a, which represents the autocorrelation of the reference pulse, the main part of the chirp was hereby reduced leaving an inner pulse structure of only about 11 fringes (≈ 15 fs). The active area of the PAL-SLM was parameterized as an one-dimensional horizontal array of tiltable planes. The number of parameters was again increased stepwise during the optimization. Fig. 2.10b presents the optimized result. The wing-like structure could be reduced and the pulse duration shortened to about 12.5 fs. The spectrum in the inset of Fig. 2.10a should be able to support much shorter pulse durations below 10 fs. Presumably, remaining spatial inhomogeneities and chirp limit the compressibility.

The included possibility to also modulate the spectrally resolved vertical component of the beam in the “temporal”-shaping setup (see Section 2.1.1) could compensate the spatial chirp partly. Interferometric autocorrelations of optimized pulses generally had a slightly higher peak-to-background ratio than reference pulses. To be able to counteract the spatial chirp a spatio-temporal optimization was performed in the following.

2.2.3 Spatio-temporal Compression

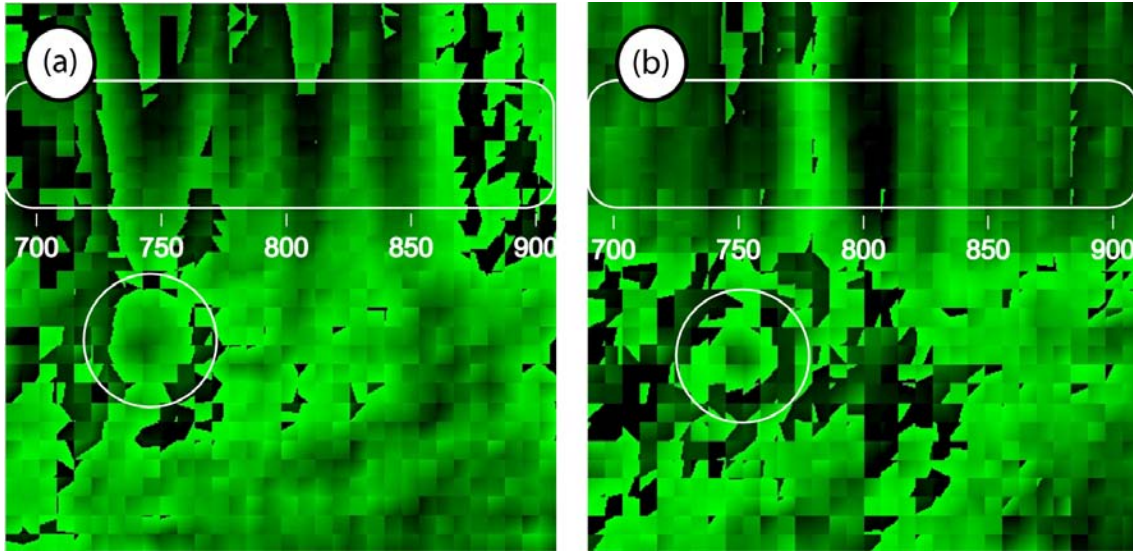


Figure 2.11: Optimized two-dimensional phase profile of two similar spatio-temporal minimization of the pulse duration obtained on two different days.

Analogue to the case of the spatio-temporal optimization of the hollow-fiber output pulse described in Section 2.1.2, the setup of the pulse shaper was modified so that the spatial profile of the temporally shaped laser pulse also hits the active area at a displaced position. Unlike the realization in Section 2.1.2 the laser spot on the spatial section of the modulation area was now moved closer to its center (Fig. 2.11a).

Fig. 2.12a shows the interferometric autocorrelation trace of the unmodulated laser pulse. A peak-to-background ratio as low as 4:1 is obtained and attributed to spatial chirp of the pulses. The IAC-trace of the temporally compressed and spatially modulated pulse (Fig. 2.12b) has an increased peak-to-background ratio of 6:1. However, this result is inferior to previous optimizations. The spatial chirp of the laser pulses could not be reduced completely. Further closure of the iris aperture in front of the photodiode changes the shape of autocorrelation trace (Fig. 2.12c). This is a clear indication that the laser pulses still have an inhomogeneous spatial profile.

Taking a closer look at the optimized phase profile of Fig. 2.11a, the position at which the laser pulse hits the modulation area (indicated by the grey circle) is surrounded by 2π -phase jumps that inevitably distort the spatial profile of broadband laser pulses (Appendix B).

The phase profile of the PAL-SLM is presented in Fig. 2.12a together with an equivalent optimization from a different day (Fig. 2.12b). Main differences can be seen in the temporal section (upper part) as generated spectra vary on a daily basis even for identical gas-pressures and laser powers. However, the phase profiles in the vicinity of the laser spot in the spatial section resemble each other. If it is possible to generate laser pulses with similar properties after spectral broadening on different days, it should also be possible to use previously optimized phase profiles as an “initial”-profile that already compensates most of the temporal chirp. This should further reduce the amount of time that is needed

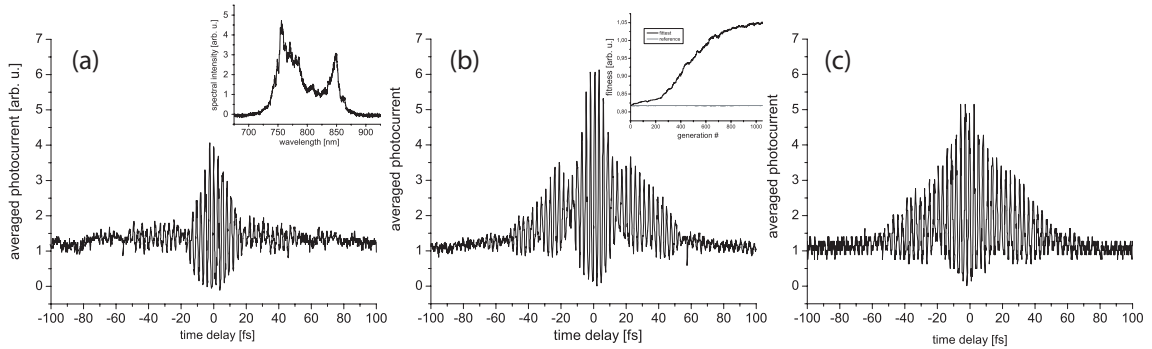


Figure 2.12: Interferometric autocorrelation traces of the laser pulses before (a) and after (b, c) adaptive compression. As the measured autocorrelations have low peak-to-background ratio estimations about the pulse duration (≈ 12 to 15 fs) are unreliable. The peak-to-background ratio could be increased by the optimization, but spatial chirp was not fully compensated. (c) was obtained by further closure of an iris aperture in front of the two-photon photodiode revealing a modified temporal pulse profile—an indication of spatial chirp. The inset of (a) shows the spectrum and the inset of (b) the evolution of the fitness of the optimization.

for the adaptive compression.

2.2.4 Adaptive Compression using SPIDER

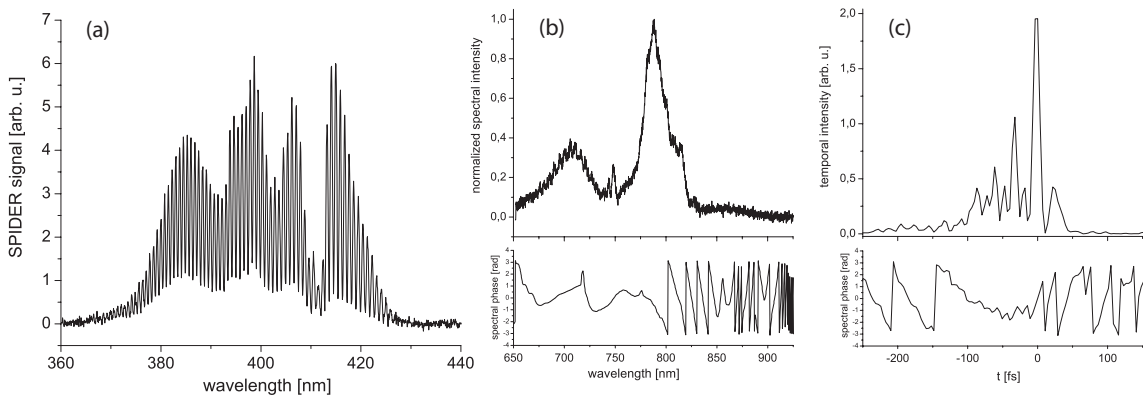


Figure 2.13: (a) SPIDER-trace of an unmodulated broadband laser pulse. Its spectrum is given in (b) together with the reconstructed spectral phase. This complicated phase function cannot be compensated by simple grating- or prism compressors. The corresponding temporal intensity distribution (and its temporal phase) is shown in (c). A pulse train of a duration of up to 100 fs is obtained.

As was already mentioned, the result of the interferometric autocorrelation can be unreliable for unknown or even complex temporal pulse shapes. It was previously shown that additional distortions like spatial chirp can destroy interference fringes making further analysis unreliable. Pulse durations measured under such conditions have to be double-checked with an alternative characterization method. Therefore a SPIDER setup was de-

signed that can determine the complete temporal information of laser pulses (see Section 1.4.3). In comparison to the simple setup for interferometric autocorrelation the SPIDER setup is much more sophisticated and has to be adjusted with greatest care.

SPIDER-Characterization of Broadband Laser Pulses

To generate a SPIDER spectrum spatial and temporal overlap of a double pulse with a temporally chirped pulse in a nonlinear crystal has to be achieved. A 25 μm BBO crystal was used for noncollinear frequency mixing. Thin crystals have low conversion efficiencies but are able to mix a wide range of frequencies due to limited phase mismatch. The interferometric signal of the frequency-mixed double pulses then gives the SPIDER spectrum from which the electric field of one of the pulse replica can be reconstructed. To maximize the detected SPIDER-signal no attenuators were used in the setup and laser power was controlled by aperturing the beam. It was carefully checked that the increased intensity did not damage the modulation area of the PAL-SLM.

Accurate measurement of spectrally broadened laser pulses with up to a spectral bandwidth of 250 nm that also exhibit spatial inhomogeneities and chirp can be a challenging task. Ideally, each of the two pulse replica has to be frequency-mixed with a defined frequency of the temporally chirped pulse. If this temporally chirped pulse also exhibits spatial chirp this condition can no longer be fulfilled and the SPIDER spectrum will be of limited use.

Therefore generally only homogeneous parts of the full beam were “SPIDERed”. In the next section a method is demonstrated to reduce the overall amount of spatial chirp of the output pulses of filaments. For this section apertured beams with low spatial chirp are used.

Fig. 2.13 shows the fundamental spectrum and the obtained SPIDER spectrum of spectrally broadened pulses directly after the exit of the filament tube without passing the pulse shaping setup. The corresponding retrieved spectral phase is given in Fig. 2.13c. Due to the non-flat structure the respective temporal electric field (Fig. 2.13d) consists rather of a pulse train with a length of more than 50 fs than of a single pulse. In the bandwidth limited case pulse durations of about 10 fs are expected. As the nontrivial phase profile of Fig. 2.13c cannot be expected to be compressible with a pair of prisms, the pulse shaping setup was used for compression.

Direct Pulse Compression using the Negative Phase as Feedback

As the SPIDER algorithm retrieves the phase of the measured pulses, the negative phase can be directly used to supply the temporal pulse shaping setup with the correct phase profile for compensation. Ideally, no iterative process will be needed as one SPIDER-measurement contains all information to compensate the phase structure of a pulse. However, depending on the modulation-depth of the SPIDER-trace, the values of the extracted phase can fluctuate and jumps of 2π are observed if spectral “holes” are present (Fig. 2.14a). In spectral parts with low intensity the amplitude of interference fringes in the SPIDER-trace will be low to non-existent and the recovered phase is subject to fluctuations. The stability and modulation of SPIDER-traces can be increased with lower pressure inside the filament-tube and smaller spectra to work with.

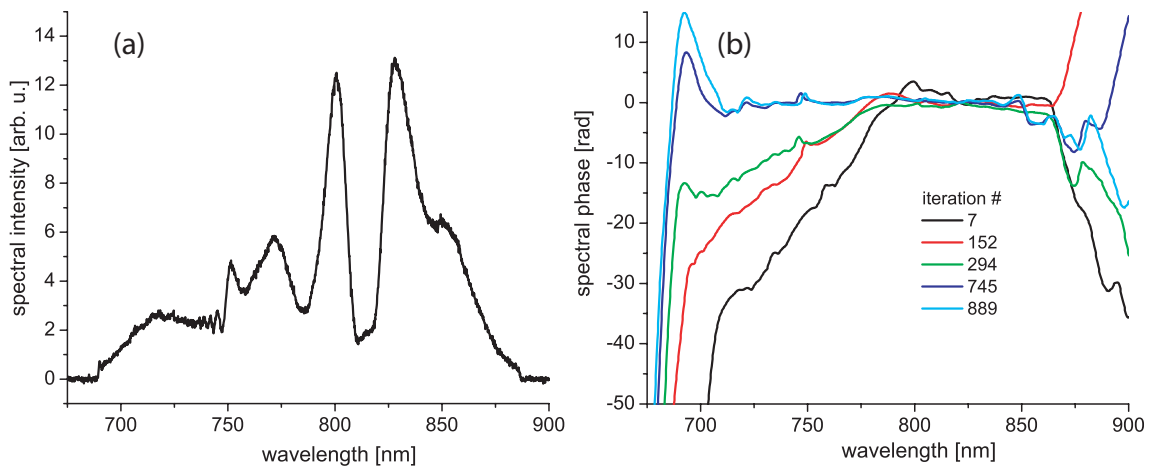


Figure 2.14: (a) Spectrum of the laser pulses that are compressed by phase compensation with the negative phase obtained by SPIDER. A spectral “hole” is present in the region around 815 nm that causes fluctuations in the reconstructed spectral phase (erratic jumps of 2π). (b) snapshots of the spectral phase during the iteration-process.

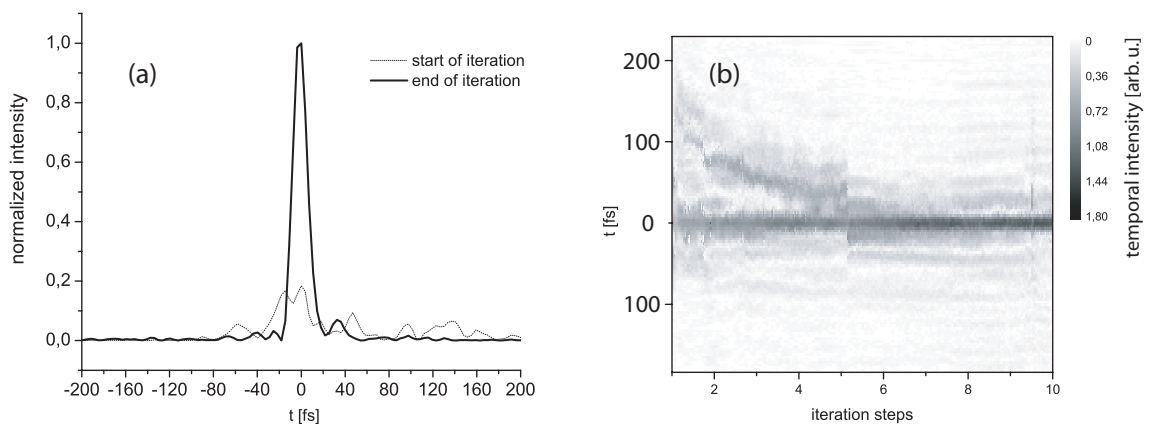


Figure 2.15: (a) Comparison of the temporal intensity distribution at the beginning (dotted line) and at the end of the iteration (solid line). The pulse duration was reduced to 15 fs. (b) Evolution of the temporal intensity distribution as function of iteration steps.

To directly display the negative phase as feedback the PAL-SLM was set to work in a one-dimensional mode (pixels were grouped in columns to form 768 vertical stripes). It received an input-phase proportional to the retrieved negative phase from the SPIDER-algorithm. The amplitude of this input-phase was chosen to be only a small fraction of the measured phase. Therefore, erratic fluctuations can be averaged after a number of iterations.

The iteration process converged to a nearly flat phase structure for the full spectrum. Fig. 2.14b illustrates the evolution of the iteration-process with snapshots of the reconstructed phase for different iteration numbers. The spectral phase could be flattened for the main part of the spectrum with remaining fluctuations of about ± 2 rad. As the PAL-SLM is capable to modify the phase of its modulation area with a resolution as low as about $\pi/100$ it should be able to compensate the remaining phase. However, this is only possible for pulses with a flat phase front for each frequency. Fig. 2.15a shows the reconstructed

temporal intensity distribution before and after the iteration-process and Fig. 2.15b illustrates the evolution of the temporal electric field as a number of iteration steps. Measured pulse durations of 15 fs could be obtained as a result.

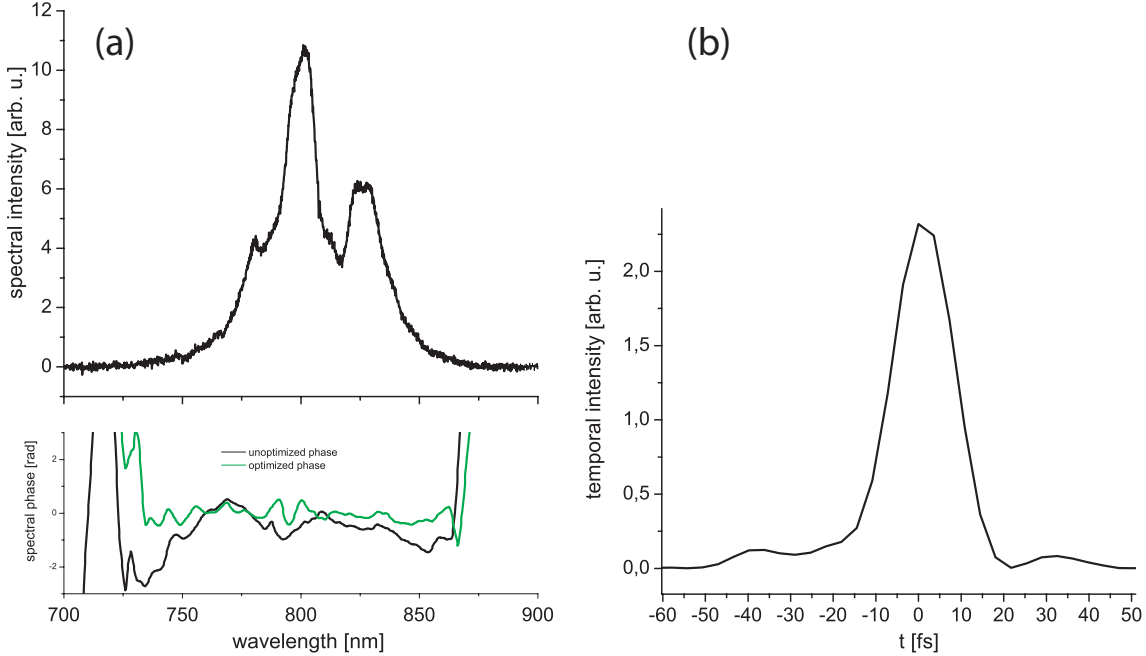


Figure 2.16: (a) Spectral intensity and phase for a slightly broadened laser pulse. The unoptimized spectral phase is already relatively flat and can be minimized into an interval of ± 0.5 rad. (b) corresponding temporal intensity distribution.

In Fig. 2.16 the compression of pulses with nearly Gaussian-shaped spectra are presented. The spectrum has only a FWHM of about 50 nm and was obtained with reduced pressure inside the filament-tube. Therefore the amount of self-phase modulation is reduced but spectral holes can be prevented. The optimized spectral phase in Fig. 2.16 has variations as low as ± 0.5 rad in a spectral range of 130 nm corresponding to a pulse duration of 16.8 fs. The phase oscillation at a wavelength of about 795 nm could not be removed, even after manual fine-tuning of the phase-profile on the PAL-SLM in this spectral region.

Careful study of the problem revealed that the laser intensity was high enough to influence the modulation area of the PAL-SLM. As is described in Appendix A, the PAL-SLM starts to change the polarization of an intense incident laser pulse (linear polarized pulses will become partly elliptically polarized). As a consequence parts of the spectrum will have a reduced reflectivity at polarization sensitive optics (e.g. gratings or beam-splitters). This influences the spectrum of the pulse after passage of the compression setup and changes the result of the SPIDER-measurement. This inherent intensity modulation of the laser pulses limits the applicability of the SPIDER-phase feedback method and explains the limited success of this method. As similar behaviour is expected during adaptive compressions of a non-attenuated beam using a learning algorithm setup. A redesign of the pulse shaping setup is therefore necessary that will distribute the pulse energy over the full modulation area of the PAL-SLM.

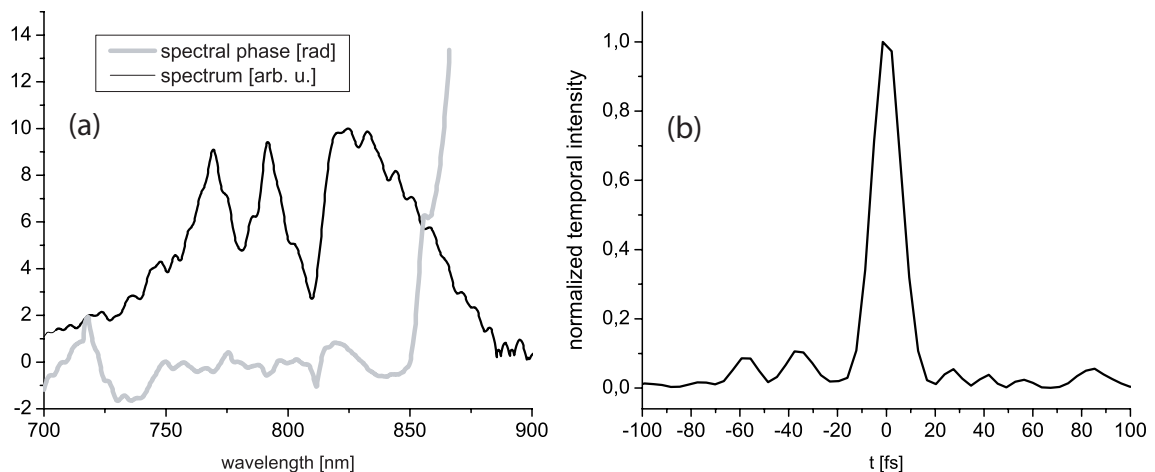


Figure 2.17: Compressed of laser pulse after manual alignment of the optical setup. (a) Spectrum and phase, (c) reconstructed temporal intensity distribution.

Manual Optimization of the Pulse Duration

Finally, the experimental setup was manually aligned with respect to a short pulse duration. This especially included adjustment of the laser coupling into the filament-tube and the argon pressure inside the tube. Quadratic chirp was compensated with the grating compressor of the pulse shaping setup for a flat phase profile on the PAL-SLM. Unlike the fluctuating spectral phase of Fig. 2.13b, phase variations smaller than ± 1 rad could be obtained corresponding to a pulse duration of about 13 fs. Subsequent compression using the negative phase as feedback did not result in further improvement.

Conclusion

The direct reconstruction of the electric field with SPIDER is a convenient method to get feedback information in real-time. This will help to fine-tune the pulse compression setup (including the sensitive alignment of filaments and hollow fiber-setsups). Such “manually” compressed pulses can then be directly used for experimental applications or used as starting point for an optimization.

Using the negative phase as feedback signal already works to flatten the phase of laser pulses down to about ± 1 rad in a short amount of time. Modification of the pulse shaping setup to distribute the spectrum over the full modulation area of the PAL-SLM can be a possible solution to the nonlinear behaviour of the device at high intensities that will limit its applicability.

2.2.5 Spatial Optimization of the Beam Profile

During the experimental work on laser pulse compression presented above the spatial chirp of the output of the filament-tube was reduced as far as possible. With growing experience in alignment of the compressor in the laser amplifier and the focusing lens for the filament a homogeneous beam profile was obtained (Fig. 2.9b)—at least to the human eye.

Fig. 2.9b shows the beam profile of the visible part of the laser beam after it exits the gas cell. This color picture was taken with a conventional color CCD-camera. Those cameras have integrated color filters and especially an IR-filter to resemble the spectral sensitivity of the human eye (frequencies greater than 700 nm are blocked). No spatial inhomogeneities are observable besides the radial chirp to higher frequencies with increasing divergence angle due to conical emission [15]. However, as opposed to Fig. 2.9b inhomogeneous structures are revealed when the full spectrum is recorded with a black-and-white CCD camera without spectral filters (SONY XC-ST 50 CCD), as can be seen in Fig. 2.18a. They presumably result from initial phase front distortions of the laser pulse prior to filamentation and the complex propagation dynamics within the filament. Recently it was demonstrated that the spatial intensity profile of the laser beam with 400 nm central wavelength can also be improved during propagation inside a long filament [73]. However, this has not been observed with the more compact setup used for this work. An inhomogeneous spectral intensity distribution allows only some parts of the pulse to be temporally compressed to shortest durations with high intensity, the remaining parts will keep a longer time structure.

To improve the spatial qualities of the beam profile after filamentation, the PAL-SLM will be used for spatial light modulation of the incoming laser pulses. Fig. 2.18a was obtained with a flat phase profile on the spatial light modulator. With the help of the evolutionary algorithm the spatial phase profile of the input pulse will be optimized. A similar setup has already been used to stabilize the filament with a fixed phase mask on the SLM [74]. However, no adaptive spatial optimization with respect to spatial chirp was performed.

As feedback a fitness function that evaluates the recorded intensity distribution of the output pulse was defined. This function divides the recorded image of the pulse into four quadrants and compares their integrated signals. A small difference between each of them will result in a high fitness and vice versa. Optimization of this fitness value will favor a symmetric beam profile over an asymmetric one.

However, the definition of this function does not yet include any information about the spectral width of the laser pulses and only evaluates its spatial properties. Therefore the algorithm can defocus the beam and prevent the generation of a filament while maintaining the good spatial profile of the laser beam. An easy way to counteract this behavior is to complement the fitness function by an additional fitness parameter. This parameter consists of the integrated intensity of a reflex of the visible tail of the white light continuum obtainable from a prism compressor. Thus, the algorithm will maintain the filament and can even improve the spectral width.

Fig. 2.18b shows the measured beam profile of the laser pulse after generation of a white light filament at the end of an optimization with the evolutionary algorithm (700 generations with 32×32 pixel planes used during the last 300 generations). In comparison to Fig. 2.18a inhomogeneities are minimized. The overall intensity is now concentrated within a more confined structure. The optimization shifted the onset of filamentation by about 2 cm and increased the length of the filament by about 4 cm. The divergence of the output beam was decreased at the same time.

To analyze the effect on the spatial chirp of the output pulse the spectral distribution at different positions along the spatial beam profile was measured. The beam with a FWHM

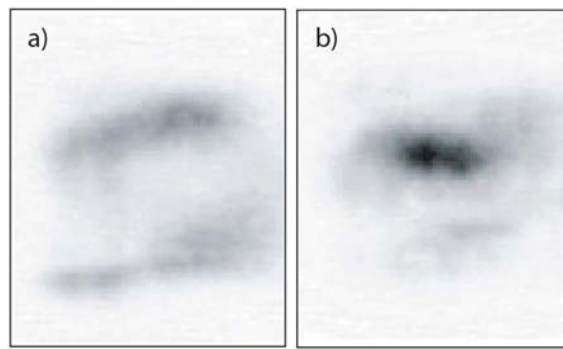


Figure 2.18: Spatial IR intensity distribution of the output pulse of the filament before (a) and after (b) an optimization of the spatial phase profile of the input pulse. The inhomogeneous structure of (a) could be reduced to only one peak of intensity (b).

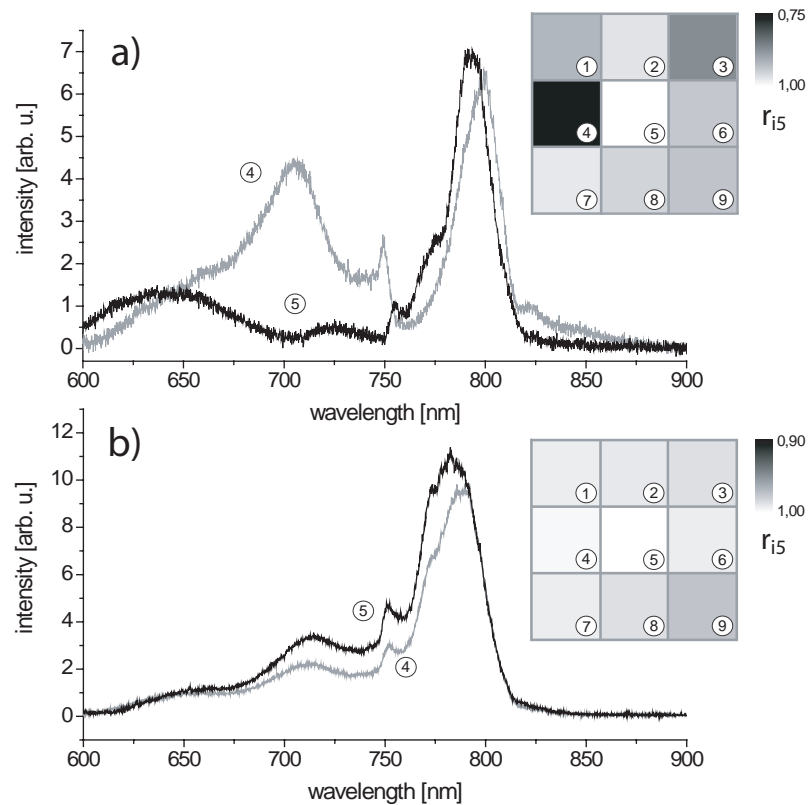


Figure 2.19: Spectra of the output pulse before (a) and after (b) an optimization of the spatial intensity profile of the laser pulse after filamentation. To quantify the spatial chirp in each case the insets show the correlation r_{i5} of measured spectra at different spatial positions along the beam profile (3×3 matrix pattern). As an example spectrum 4 (grey) and 5 (black) that have the lowest correlation of $r_{45} = 0.77$ are displayed in (a). The two spectral maxima are separated by different amounts and spectral holes are still present. This spatial chirp and spectral inhomogeneity is reduced in (b) with measured correlations $r_{i5} > 0.97$ (note also the different scaling for the inset of (b)).

diameter of about 8 mm was scanned in a 3×3 matrix pattern by an iris aperture of 2 mm diameter and for each position the spectrum of the apertured beam was recorded. Fig. 2.19a presents the result for a flat phase on the spatial light modulator. The two spectra were obtained at two neighboring spatial positions along the beam but still differ from each other significantly. To quantify the resulting spatial chirp the central spectrum of the 3×3 matrix was taken as a reference spectrum to which all surrounding spectra are compared. Therefore, each of the spectra is correlated to the central one. The corresponding correlation matrices are plotted in the insets of Fig. 2.19. The correlation r_{i5} of spectrum i with the central spectrum (designated as correlation 5 in the insets) is defined as:

$$r_{i5} = \frac{\int I_i(\lambda)I_5(\lambda)d\lambda}{(\int I_i(\lambda)^2d\lambda \int I_5(\lambda)^2d\lambda)^{1/2}} \quad (2.1)$$

with $I_i(\lambda)$ as the spectral intensity ($i = 1..9$) of the corresponding grid position of the matrix (see Fig. 2.19). A correlation close to 1 implies similar spectra and low spatial chirp. A direct comparison to the corresponding results in Fig. 2.19b for the optimized beam profile clearly shows an improvement. The average correlation increased from 0.92 to 0.99 as result of reduced spatial chirp. The measured spectra mainly varied only in intensity (Fig. 2.19b shows the central spectrum at position 5) and support the generation of 10 fs laser pulses.

Adaptive optimization of the spatial phase profile of ultrashort laser pulses prior to filamentation therefore proves to be a convenient technique to improve the spatial qualities of the spectrally broadened laser pulses. This will be beneficial to any application of ultrashort high intensity laser pulses like the efficient generation of high harmonics. A future setup will include the additional evaluation of the spectrum of broadened laser pulses. This will allow to engineer the spectral shape of the laser pulses during an optimization as the next step to get maximal control of the filament and to generate intense few cycle laser pulses.

2.3 Conclusion

Several different possibilities were investigated to compress ultrashort laser pulses. The main advantages and disadvantages can be summarized briefly:

- **Hollow-fiber setup:** compression to achieve shortest pulses possible (11 fs) due to good spatial qualities of output pulses. However, problems with long time stability and limited output power.
- **Filamentation:** High power output and improved long time stability. However, spatial chirps limits compression efficiency (this chirp can be reduced => further study needed).
- **Negative phase-feedback using SPIDER:** very fast method to compensate phase irregularities. However, sensitive alignment of setup required.

Using the spatiotemporal modification of the pulse shaping setup will be the most general solution for optimizations in future experimental applications. However, the pulse shaping setup may have to be modified to reduce the intensity of laser pulses during interaction with the sensitive modulation area of the PAL-SLM. The pulse shaping setup was mainly designed to “shape” laser pulses in a general sense and is not limited to merely temporal compression of pulses.

In the next chapter ultrashort laser pulses will be used for the generation of high-harmonic radiation. As will be shown in Chapter 4 shaped laser pulses can control or optimize the outcome of experiments. The process of high-harmonic generation is sensitive to the spatial and temporal structure of the driving laser pulse, it can therefore also be influenced by modified laser pulse shapes.

Chapter 3

High-Harmonic Generation

When an intense ultrashort laser pulse interacts with matter, part of the radiation can be converted to higher frequencies. Due to the generation of specifically multiples of the fundamental frequency this process is called high-harmonic generation (HHG). After the first measurements of low-order harmonics the conversion efficiency to higher orders was found to drop down exponentially. However, at some point this behaviour changed. It was discovered that with increasing order the conversion efficiency was relatively constant and the high-harmonic spectrum displayed a plateau-like structure that abruptly drops off at a certain energy [32, 33].

This surprising behaviour could be explained by a simple quasi-classical model. In 1993 Corkum [75] and Kulander et al. [76] simplified the problem and presented a theory that was able to explain the empirical results. The model could illustrate the harmonic plateau by assuming that perturbation theory is no longer valid for the plateau harmonics as they are generated by the free electron of the ionized atom. The position of the harmonic cut-off was obtained with striking accuracy. The electron that is ionized by the strong laser field gains additional energy in the laser field and recombines, emitting high energy radiation. As this process happens every half-cycle of the laser pulse a spectrum of odd harmonics of the fundamental laser field is generated. These generated harmonics can extend up to very high orders spanning a wide wavelength range of XUV or soft x-ray radiation.

X-ray radiation was already discovered by Röntgen in 1895 and x-rays have been generated in simple x-ray tubes. By generating high harmonics with ultrashort laser pulses the resulting high energy photons will have additional properties:

Due to the coherent nature of the process of HHG the generated radiation will be coherent in time and space. Unlike the incoherent x-rays of simple x-ray tubes, the coherent high-harmonic x-rays will propagate as a beam with high peak-brightness. The temporal coherence implies that the phases of all harmonics are coupled so that they will interfere and form short pulses. In fact, the timescale of the generated XUV bursts can reach down to the attosecond regime [77, 78].

A typical spectrum of high harmonics is found in Fig. 3.1 and consists only of odd integer orders. On the left part lower-order harmonics are shown that illustrate the different regimes of HHG. The harmonic intensity decreases rapidly for the lowest orders (pertur-

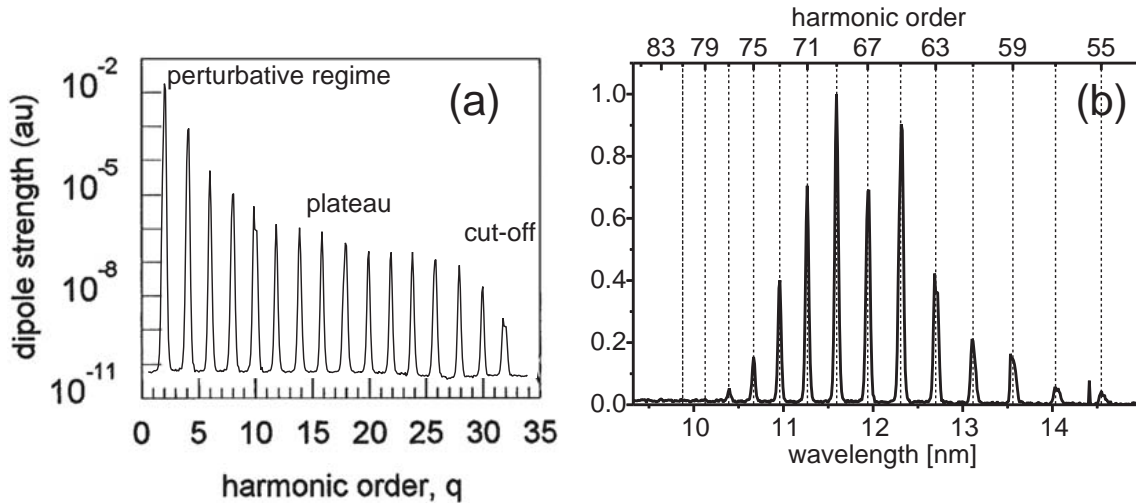


Figure 3.1: Typical high-harmonic spectra. (a) Unfiltered harmonic spectrum illustrating the characteristic spectral shape (adapted from [79]). The perturbative regime of the low-order harmonics is followed by the plateau region with harmonic peaks of constant intensity. The spectrum is terminated by the cut-off, the highest harmonics that are generated. (b) High harmonics generated in neon. A zirconium filter was used to separate the fundamental light and lower order harmonics. This explains the drop in intensity to lower orders.

bative regime). Higher orders exhibit equal intensity and form a plateau. The intensity of the highest orders then suddenly drops identifying the cut-off region. The right part shows harmonics of higher orders. Lower orders drop in intensity due to spectral filtering with a zirconium filter.

The following section gives an overview of the three-step model used for the description of HHG together with the quantum-mechanically approach. Section 3.2 investigates the possibility of attosecond-pulse production, while Section 3.3 presents different characterization methods. Section 3.4 includes different experimental setups to generate high-harmonics that are used in this work. Various important aspects closely related to the generation of high harmonics, like the generation of plasma, phase matching and absorption, have been integrated into the relevant experimental subsections. High-harmonics are still limited by low conversion efficiencies ($\eta = 10^{-5}$ to 10^{-4} [80, 81]) and many applications demand higher intensities. Therefore, Section 5 contains different ideas to enhance the high-harmonic output and Section 6 contains alternative methods to generate ultrashort x-rays.

3.1 Theoretical Description

The following section gives an overview of the theoretical concepts to describe the process of high-harmonic generation with some mathematical background. It will only cover the theory of the single-atom response to an external laser pulse. However, the experimental realization of HHG is dependent on the emission of a high number of atoms or molecules and will be subject to macroscopic effects like phase-matching and absorption. These

matters will be discussed in the following experimental section.

3.1.1 Three-Step Model

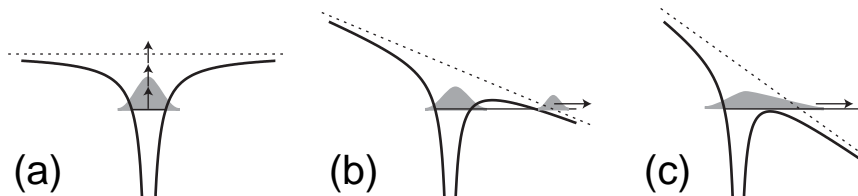


Figure 3.2: Different ionization scenarios. If the ionization potential is low compared to the frequency of the light but large compared to the electric field of the laser the absorption of multiple photons is the dominant ionization mechanism (multiphoton ionization (a)). If the electric field strength becomes comparable to the Coulomb binding force of the atom, the Coulomb potential is significantly modified. If the frequency of light is low enough such that the electron can respond to this changing potential, the electron can tunnel through the remaining potential wall (tunnel ionization (b)). Even higher electric fields can suppress the Coulomb barrier completely (barrier-suppressed ionization (c)).

The most important relations connected the generation of high-harmonic radiation can be explained in the picture of the semi-classical three-step model that was formulated by Corkum et al. in 1993 [75]. The experiment is modeled by considering an atom under the influence of a linearly polarized laser field. Furthermore, the single-electron approximation is used and the electron is treated as free particle after ionization.

The three-step model divides the process of high-harmonic generation into three consecutive steps (see also Fig. 3.3):

- **ionization** by the laser field
- **acceleration** in the laser field
- **recombination** with the parent atom and emission of a high energy photon

Ionization

At laser intensities higher than 10^{14} W/cm² the Coulomb barrier of the atom becomes depressed and the electron can tunnel with high probability through the remaining potential or is directly field ionized (barrier-suppressed ionization [82]). This will happen twice per optical cycle depending on the amplitude of the electric field. Whether the electron will be tunnel-ionized or ionized by absorption of multiple photons is determined by the ionization potential I_p of the atom, the electric field amplitude E_0 and the frequency of the field, i.e. the energy of the photons (Fig. 3.2).

To simplify the problem the ponderomotive potential U_p can be introduced (in atomic units):

$$U_p = E_0^2 / (4m\omega^2) \quad (3.1)$$

The ponderomotive potential is an effective potential seen by a particle in an oscillating field on average over the fast oscillations. It is not a true potential but can be used as relation to I_p .

In 1965 Keldysh introduced a parameter that connects both potentials U_p and I_p to give an estimate if an electron will tunnel out of the atom or is ionized by multi-photon absorption [83]: The Keldysh parameter:

$$\gamma = \sqrt{\frac{I_p}{2U_p}}. \quad (3.2)$$

- If $\gamma > 1$ then U_p is small compared to I_p and the electron will be mainly ionized by multi-photon ionization.
- If $\gamma < 1$ tunnel-ionization will prevail.

Propagation

Once the electron is free from the binding forces of the atom, it will feel only the strong electric field of the oscillating laser. First, it will be accelerated away from the atom and later back to it after the laser field reverses. The amplitude of this oscillation can be generalized to be E_0/ω^2 and is of the order of some nanometers. This justifies the assumption that the remaining Coulomb potential can be neglected for the “free” electron. Depending on the phase of the electric field in which the electron is ionized, it will experience different amounts of acceleration in the field and therefore gain different amounts of kinetic energy.

Recombination

Depending on its acceleration in the laser field the electron may be driven back towards the core with high kinetic energy and recombine to the ground state. In this case the kinetic energy that was obtained and the energy of the ionization potential will be released as a high-energy photon. Based on the model, it was calculated that electrons that are ionized at a phase of 18° will have acquired the highest possible energy in the oscillating field at the moment of recombination. This phase-value lies close to the peak of the electric field and the ionization probability will be high.

The energy of the emitted radiation of these electrons is estimated to be:

$$\hbar\omega_c = 3.17U_p + I_p. \quad (3.3)$$

Eq. (3.3) is known as the cut-off law and has been validated by experimental results.

According to the three-step model a continuous spectrum of high energy radiation will be emitted that drops rapidly to zero at the cut-off. Assuming that the electric field strength

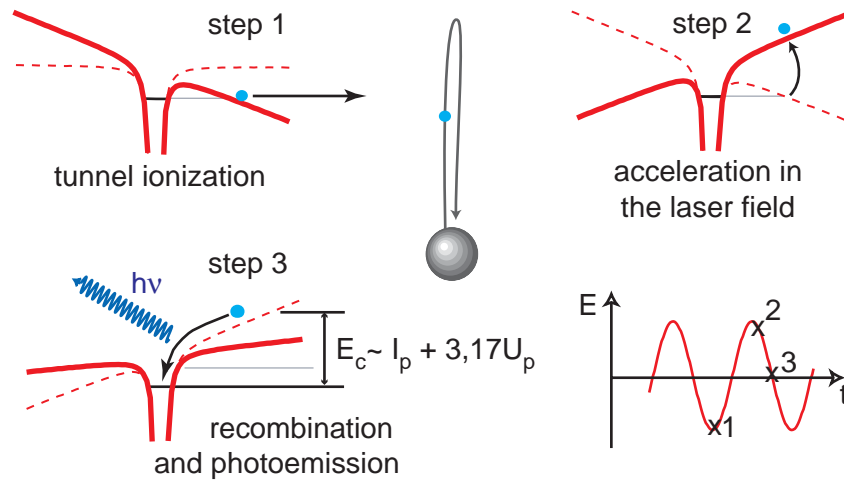


Figure 3.3: Illustration of the three-step model for high-harmonic generation. During step 1 the electron is ionized at a particular phase of the electric field. It is then accelerated in the laser field (step 2) and can recombine with the atom emitting a photon carrying the kinetic energy of the electron plus its ionization potential (step 3). The highest kinetic energies of this model are $3.17 U_p$, defining the so-called cut-off photon energy in the harmonic spectrum.

is strong enough, electrons that contribute to high-harmonic radiation are generated every half-cycle of the fundamental field. To explain the generation of equally spaced spectral peaks (Fig. 3.1) we have to take the temporal interference a large number of emitted high-energy photons, that are generated by these electrons during each half cycle, into account. If we now have a high number of emitting atoms with a fixed spatial distribution the spatial coherence of the generation process will direct the radiation to propagate collinearly to the driving laser field. A pulse train of harmonics will develop after some laser oscillations with a temporal separation of $T/2$ between subsequent pulses (T is the oscillation-cycle period of the driving field). Due to temporal coherence, the spectra of all pulses of the train will interfere and form a resulting spectrum of discrete lines. The spacing of these spectral lines is given by the inverse value of the temporal separation $1/\frac{T}{2} = 2f$ which corresponds to the spacing of the harmonics.

As the nonlinear polarization response $P(t)$ of a mono-atomic sample shows inversion-symmetry only the odd-orders in the Taylor-expansion of $P(t)$ (Eq. (1.10)) will contribute (as illustrated in Fig. 1.5). The field response is therefore only composed of odd harmonic frequencies.

3.1.2 Quantum Mechanical Description

One year after the formulation of the semi-classical three-step model Lewenstein et al. presented a quantum mechanical explanation [84]. Starting from the time-dependent

Schrödinger equation (in atomic units)

$$i \frac{\partial}{\partial t} |\psi(\vec{r}, t)\rangle = \left(-\frac{1}{2} \nabla^2 + V(\vec{r}) + \vec{r} \vec{E} \cos(\omega t) \right) |\psi(\vec{r}, t)\rangle \quad (3.4)$$

the time-dependent dipole moment

$$\vec{\mu}(t) = \langle \psi(\vec{r}, t) | -\vec{r} | \psi(\vec{r}, t) \rangle, \quad (3.5)$$

has to be calculated. It represents the oscillating source that is responsible for the generation of high harmonics. The harmonic spectrum is then obtained by Fourier transformation of the dipole acceleration.

Following assumptions were made [84]:

- The contribution to the evolution of the system of all bound states except the ground state $|0\rangle$ can be neglected. This is fulfilled in the strong-field limit ($\gamma < 1$) as excited bound electronic states are strongly Stark shifted and smeared out [8]. In this case intermediate resonances do not affect the transition from the ground state to positive-energy continuum states.
- The depletion of the ground state can be neglected ($U_p < U_{sat}$). This is fulfilled if the laser intensities are smaller than the saturation intensity of the medium to keep ionization rates low.
- In the continuum, the electron can be treated as a free particle moving in the electric field with no effect of the remaining Coulomb field. This is valid because of long electron trajectories of some nanometers (see above). U_p must be large compared to the remainder of the atomic potential. This is easily achieved for short range potentials.

Furthermore, only one electron is considered to be responsible for harmonic generation ('single-active electron approximation' (SAE [85, 76])).

Under consideration of above assumptions the following time-dependent dipole moment can be obtained:

$$\vec{\mu}(t) = i \int_0^t dt' \int d^3\vec{p} E \cos(\omega t') \times \left(\vec{d}(\vec{p} - \vec{A}(t')) \times \exp(-iS(\vec{p}, t, t')) \times \vec{d}^*(\vec{p} - \vec{A}(t')) \right) + c.c. \quad (3.6)$$

$\vec{A}(t)$ is the vector potential of the laser field and $S(\vec{p}, t, t')$ the quasi-classical action [4]:

$$S(\vec{p}, t, t') = \int_{t'}^t dt'' \left(\frac{(\vec{p} - \vec{A}(t''))^2}{2} + I_p \right) \quad (3.7)$$

Interestingly, different parts of Eq. (3.6) can now be identified with the three steps of the simple three-step model (theoretical details in [86, 87]). The equivalent conjugated complex terms (c.c. in Eq. (3.6)) are omitted for the sake of simplicity.

- $E \cos(\omega t') \times \left(\vec{d}^* \left(\vec{p} - \vec{A}(t') \right) \right)$ is the probability amplitude for an electron to make a transition to the continuum at time t' with the canonical momentum $p = v + A(t)$ —**ionization of the ground state at time t'** .
- The quasi-classical action $S(\vec{p}, t, t')$ describes the propagation of an electron freely moving in the laser field where it will acquire the phase factor $\exp(-iS(\vec{p}, t, t'))$ (atomic dipole phase)—**propagation in the continuum in the time interval $t - t'$** .
- The probability amplitude for recombination is finally given by $\vec{d}^* \left(\vec{p} - \vec{A}(t) \right)$ —**recombination to the ground state at time t** .

By Fourier transforming the time-dependent dipole moment, the harmonic spectra can be calculated and analyzed. The cut-off photon energy can now be found to be:

$$\hbar\omega_c = 3.17U_p + f\left(\frac{I_p}{U_p}\right) I_p, \quad (3.8)$$

where $f(x)$ is a slowly varying function of the order of 1 and includes purely quantum mechanical effects. Eq. (3.8) shows excellent agreement to its semi-classical counterpart Eq. (3.3) and confirms its validity.

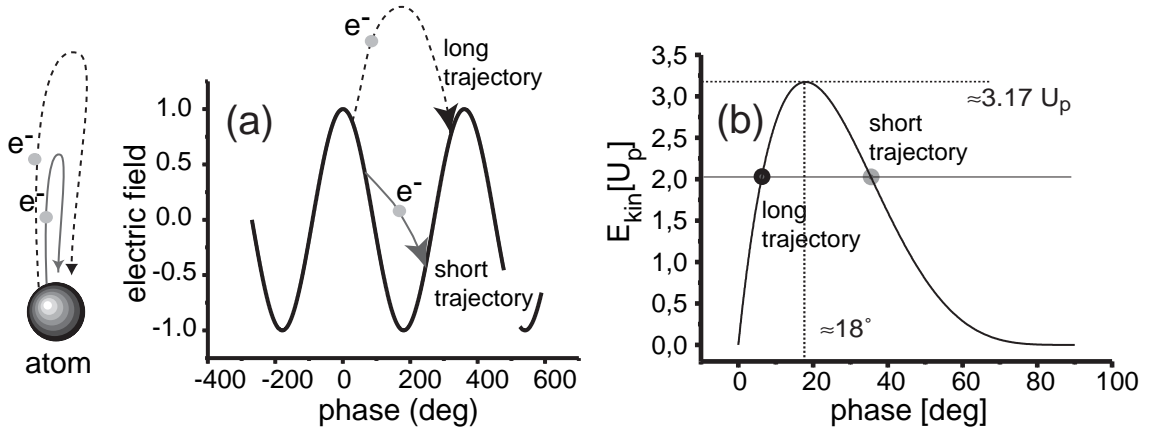


Figure 3.4: (a) Electrons that are ionized at different phases of the electric field travel in two different trajectories and are mainly responsible for the generation of harmonics with particular photon energy. (b) Kinetic energy of electrons at the moment of recombination with the atomic core for ionization at different phases. Ionization at a phase of 18 degrees yields the maximum energy (cut-off). For this phase only one electron trajectory exists.

A closer study reveals that each kinetic energy of the plateau region can be generated at two distinct particular phases of the electric field at the moment of ionization [88] (see

Fig. 3.4). In each of these two phases electrons are born that travel different trajectories—or quantum paths—until they recombine with the ion.

One of those two trajectories spends a longer time in the continuum and has a return time τ_2 very close to a full period of the laser field (‘long trajectory’). The other has a shorter return time τ_1 less than half a laser period (‘short trajectory’) (Fig. 3.4 and Fig. 3.5). Depending on their relative atomic dipole phases, these trajectories will interfere with each other. As the temporal shape of the electric field governs the propagation dynamics of the electrons in the continuum the long trajectory will feel effects of increased intensity or a temporally shaped laser field more strongly.

The phase of the long trajectory is nearly linearly proportional to the laser intensity I , while the phase of the short trajectory stays almost constant [89, 90]. This effect will introduce a linear chirp for the emitted high harmonics. Since the laser pulse intensity at the peak of the laser pulse can be approximated to vary quadratically with respect to time, a quadratic temporal phase will be imparted on the high-harmonics (=linear chirp) [91, 92].

By engineering the temporal structure of electric field of the driving pulse, it is therefore also possible to alter the temporal structure of the emitted harmonic radiation [93, 94]. As HHG can be used to generate attosecond-pulses (see Section 3.2) this is a possibility for attosecond pulse shaping.

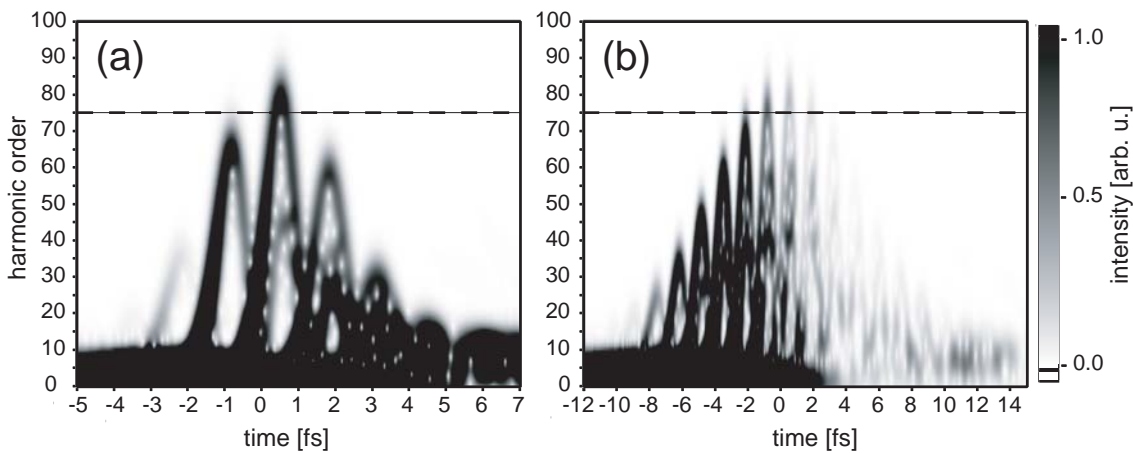


Figure 3.5: Time-frequency analysis of the simulated dipole response of hydrogen in an intense 5.5×10^{14} W/cm² 800 nm laser field for a 4 fs driving laser pulse (a) and a 10 fs driving laser pulse (b). The simulation was performed for a two-dimensional quantummechanical system using the split-step-operator technique [95]. In analogy to Fig. 3.4 the contribution of two different electron trajectories is visible. Above an energy threshold of 116 eV (75th harmonic at 800 nm) the generation of an isolated attosecond pulse is possible in the cut-off region of the spectrum for the 4 fs pulse. A train of about 4 attosecond pulses is generated for the 10 fs driving pulse in the same energy region.

3.2 Sub-fs Pulse Production

As already mentioned, the shortest possible pulses for a given central wavelength are single-cycle pulses. Ultrashort laser pulses generated by Ti:Sa laser systems will have their wavelength centered around 800 nm. This limits the shortest possible pulses to about 2.7 fs. Generation of shorter pulses will require higher carrier frequencies. With the technique of high-harmonic generation we have an excellent tool, to convert infrared radiation into the soft-x-ray regime. Due to the fact that harmonics are predominantly generated at the peaks of the electric field they will be emitted on timeframes quite shorter than one cycle of the driving pulse field.

As was already discussed, high harmonics exhibit an intrinsic chirp due to the intensity dependence of the electron's quantum paths. As was shown in [96], the limited number of five consecutive harmonics of the plateau region can exhibit a nearly linear chirp with respect to each other. For the synthesis of an attosecond pulse, it can therefore be more advantageous to only use a smaller number of harmonics with suitable phase relationship than taking the full harmonic spectrum.

Closer study of the HHG-process reveals that every half cycle of the electric field electrons are ionized that will follow the long and the short trajectory before they will recombine. As can be seen in Fig. 3.4, these two quantum paths exhibit complementary amounts of chirp. Higher harmonics are emitted after the lower ones for the short trajectories and lower harmonics are emitted after the higher ones for the long trajectories. In this picture two attosecond pulses are emitted each half-cycle of the field for each trajectory that will merge to one temporally broadened pulse with a more complicated chirp.

By placing the laser focus in front of a gas-jet Mairesse et al. [97] isolated the contribution of the short quantum path and measured a purely linear chirp for a range of 14 consecutive harmonics. This linear chirp can be compensated by use of additional plasma dispersion of an ionized gas or using the negative group delay dispersion (GDD) of a thin aluminum foil [98]. Another possibility is to isolate harmonics generated in the cut-off region where only one quantum path exists. To isolate this energy region wavelength-sensitive structures like multilayer-mirrors [99] or metallic filters are widely used.

Above methods will generate attosecond pulses every half-cycle of the laser field and finally produce an attosecond pulse train with a duration of the order of the fundamental femtosecond pulse. To isolate a single attosecond pulse from this train is not possible anymore. However, it is possible to only generate one attosecond pulse during the interaction process with the conversion medium.

One idea takes advantage of the linear polarization dependence of the HHG-process. Accelerating electrons in elliptically polarized laser fields show dropping probability for recombination with the parent ions for increasing degree of ellipticity. Polarization shaped pulses can be designed with linear polarization limited to only one half-cycle of the electric field [100]. HHG will have highest efficiency for this short time interval and only one dominating attosecond pulse will be emitted [100].

However, by usage of long driver pulses with many field oscillations exceeding the threshold for field ionization (10^9 V/cm²) the medium can get completely ionized long before the peak intensity is reached.

The steep rising intensity gradient of few-cycle driver pulses, on the other hand, allows electrons to survive in their bound atomic state to much higher field strengths than the Coulomb binding field [101]. By careful adjustment of the laser intensity, it is possible to generate the highest harmonics by a single-electron trajectory close to one single peak of a few-cycle pulse (see Fig. 3.5a). In this case, the periodicity of the high-harmonic generation process is completely suppressed and a smooth spectrum in the cut-off region is obtained. Unprecedented kinetic energies of more than 1 keV [102, 103] during their first field oscillation cycle could be demonstrated. In this wavelength range durations of single attosecond pulses shorter than 100 as are expected.

Some notable achievements in the emerging field of attoscience include the generation of x-ray pulses with a duration of 650 as [77], trains of 250 as pulses [78] and the creation of 250 as pulses to measure electron motion with a temporal resolution of 100 as [104].

Its pulse duration is only one of many aspects of light that can be important. The broad spectrum of attosecond pulses is undesirable by spectroscopic applications. Holographic imaging techniques require a high number of photons to interact with their samples, much higher than the low conversion efficiency of HHG can provide to date. There exists a large variety of different sources of soft-x-ray radiation that compete with a growing number of applications. In this large field, that is briefly touched in Section 3.6, high-harmonic generation is a cheap and very versatile source of soft x-rays with many unique advantages that only lacks in photon numbers.

3.3 Characterization Techniques

The next important step after generation of sub-fs pulses is the development of appropriate diagnostic techniques. Autocorrelation and spectral-interferometric based methods are well developed for characterization of ultrashort pulses in the visible range. They can also be transferred to the XUV or soft-x-ray regime but it will be a challenging task (see [105, 7] for recent reviews).

Attosecond pulses are spectrally much broader compared to their femtosecond counterparts in the infrared region. They have wavelengths in the nearly inaccessible UV-XUV spectral range as there are no beamsplitters and recombiners easily available in this spectral region. Intensities are orders of magnitude weaker, thus requiring ultrasensitive nonlinear detectors with a flat broadband response. The next problem is the generation of two replica of one XUV pulse and being able to delay them (e.g. for realization of autocorrelation in the XUV [106]).

A possible solution is the use of special mirrors that consist of different parts that can be translated with respect to each other [107, 77]. Such kind of mirror can be used for the realization of a second-order XUV autocorrelator [106]. A split-mirror serves as delay-line and a two-photon ionized He gas is used as nonlinear detection medium. The He ion yield is recorded by a time-of-flight (TOF) mass spectrometer which provides the autocorrelation signal. Individual pulses with a duration of 780 as could be verified.

To date, the metrology methods in most experiments in this field have been concentrated on measuring simply the duration of extreme ultraviolet (XUV) pulses [7]. The extraction

of much more information is possible. The above described method of autocorrelation of XUV-pulses can be extended to an “X-FROG”-setup. This was realized by Sekikawa et al. [108] who measured the FROG-trace of the 5th harmonic by two-photon ionization of xenon.

An electron generated by x-ray photoionization can be deflected by a strong laser field. Its energy and angular distribution depends on the phase of the laser field at the time of ionization. This phase dependence can be used to measure the duration and chirp of single sub-100-attosecond x-ray pulses [109].

Another method, known as RABBITT [110,111] (reconstruction of attosecond beating by interference of two-photon transitions), is particularly well adapted to the case of the discrete spectrum of a periodic train of attosecond pulses. Utilizing two-photon, multicolour ionization, the amplitudes and phases of the spectral components can be determined, thus allowing the reconstruction of an average temporal profile [96, 97]. RABBITT has been used to successfully characterize trains of 250 as pulses [96] but does not reveal anything about the spectral phase within each harmonic and only gives the relative phase between adjacent orders.

Different versions of SPIDER were also realized for the XUV region. The influence of an optical field on the photoelectron spectrum produced by the XUV pulse can be exploited to produce two sheared replica pulses. Two replica of the XUV pulse are delayed with respect to each other and interact with a different monochromatic frequency slice of a chirped optical pulse in a jet of gas (XSPIDER) [105]. The phase information needed for SPIDER are contained in sidebands of the photoelectron energy spectra.

An alternative method to realize the spectral sheared replica is presented in [112]. Two time-delayed IR-pulses with slightly different central wavelengths are supposed to generate nearly identical attosecond pulses besides a shift in frequency. Their SPIDER interferogram can then simply be detected in an x-ray spectrometer (XUV SPIDER [105] / HHSPIDER [112]). This method of detection has a higher precision than the detection of electrons via photoionization. However, only low intense IR-pulses can be used as ionization of the first pulse should not influence the HHG process of the second.

This difficulty can be avoided, however, if the geometry of the nonlinear interaction is altered, so that the interferogram has a spatial rather than spectral carrier (spatially encoded arrangement for SPIDER: SEA SPIDER [105]). The encoding of the phase information in this geometry is achieved by interfering two spatially separated XUV pulses in the spatial domain after they have propagated away from the generation region. As advantage it is not necessary to resolve any spectral fringes, which relaxes the constraint on the spectral resolution of the spectrometer [113]. Also, there is no need for a time delay between the interfering pulses and thus no calibration of this quantity is needed.

3.4 Experimental Realization of High-Harmonic Generation

Within this section different setups that were used for the generation of high harmonics are described. It will give a short impression of different aspects of HHG and prepare for

the next chapter where the focus will be shifted towards control and optimization.

The experiments presented in this section and the remaining part of the work were performed with the Spectra Physics laser system. That laser is a regeneratively amplified Ti:sapphire system that delivers 80 fs pulse at 0.8 mJ energy per pulse. It has a 800 nm central wavelength and a repetition rate of 1 kHz. Generally the laser pulses are spectrally broadened by self-phase modulation in a gas-filled hollow fiber (similar to the hollow-fiber described in Chapter 2) and afterwards compressed to about 20 fs in a prism compressor. They are focused into a vacuum system and (generally) interact with a gas-target. At intensities higher than 10^{14} W/cm² a small portion of the beam will be converted into harmonics that will travel alongside with the fundamental laser beam. The fundamental part of the radiation will be filtered by passage through a metallic foil and only high harmonics will pass. Afterwards, the radiation is detected by wavelength dispersive spectrometry based on a x-ray grating spectrograph.

3.4.1 Basic setup: Gas Jet

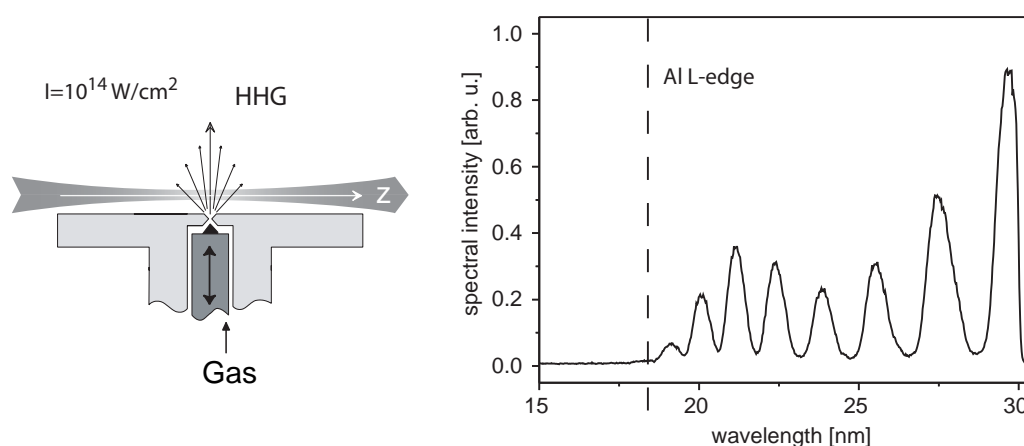


Figure 3.6: (a) Piezo-controlled pulsed gas nozzle used to prepare a gas-jet for the interaction with a focused laser pulse of high intensity inside a vacuum system. High harmonics are generated that can be detected in a x-ray spectrometer (not shown). (b) Generic spectrum of high-harmonics in the free-focusing geometry of (a). Harmonic orders up to the Al L-edge are visible. Ultrathin metallic filters (like an $0.3 \mu\text{m}$ aluminum filter) are used to block the fundamental laser beam.

The basic setup for high harmonic generation simply consists of an ultrashort laser pulse that interacts with gas atoms. As generated XUV or soft-x-ray radiation would be readily absorbed in air this has to be realized in a vacuum system. The laser pulse will be focused into a jet of noble-gas atoms (argon was generally used) provided by a gas nozzle.

To keep the background pressure as low as possible a 1 kHz pulsed gas nozzle was used that was synchronized to the laser system. Compared to conventional designs with continuous gas jets the pressure in the vacuum chamber could be reduced by a factor of 3 [114]. The laser was focused into the gas jet by a lens with 0.3 m focal length. The position of the nozzle was manually aligned with respect to the laser focus along the optical axis and

both transverse axes to maximize harmonic output. The backing pressure of the valve was chosen to be 2 bar. The amount of gas that exits the nozzle was controlled by the voltage of a piezo-modulator and carefully adjusted to have high efficiency and low gas consumption at the same time. Overheating of the nozzle was prevented by constant cooling with a water cooling system.

The spectrometer, that is used to detect the harmonics, consists of a toroidal grating illuminated under grazing incidence. The accessible photon energy range extends from about 20 eV (H13) to around 80 eV corresponding to H51. The spectrum is acquired with a back-side illuminated thinned X-ray CCD camera (Roper Scientific). The resolution of the spectrometer was estimated to be better than 0.3 nm in a wavelength range of 17 to 25 nm.

There is still a major problem concerning the generation of high harmonics in free focused geometries: As harmonics are generated, free electrons are generated as well, that will lower the phase velocity for increasing wavelengths (see “plasma-dispersion” in the next section). This introduces a strong phase mismatch between the fundamental and the harmonic beam. The mismatch increases with harmonic order and sets a limit to the highest achievable energies. If harmonics are only generated at very few cycles of the driving laser field (few-cycle pulses), phase matching effects become less important (see also Section 3.2).

Another simple way to extend the cut-off energy is to use driver pulses with longer wavelengths. According to the cut-off law (Eq. (3.3)), the ponderomotive potential U_p scales quadratically with the wavelength and therefore higher harmonic orders should be possible using driver pulses with longer wavelengths as was already demonstrated [115].

The focus position in relation to the gas-jet is of importance to the spatial [116] and temporal profile [117, 118] of generated harmonics. By analyzing the temporal coherence properties of the far-field profile of the 15th harmonic Bellini et al. [119] discovered that the inner region has a long coherence time, interpreted as being due to the contribution of the short trajectory. The coherence time of the outer region was much shorter and was contributed to emission of the long trajectory. The short trajectory contribution can be macroscopically selected by adjusting carefully the phase matching conditions, when the generating laser is focused slightly before the gas jet [116]. In this case high-harmonics with good spatial and temporal properties are obtained.

Gas-filled Ni-tube

An alternative realization of a gas-jet target for high-harmonic generation was developed for a new vacuum setup [120]. As shown in Fig. 3.7a, high harmonics are generated in a gas-filled thin-wall nickel tube (initial diameter 2 mm, see also [121, 122]). One end of the tube is filled with argon at a backing pressure of around 100 mbar, the other end is sealed. The femtosecond laser pulse is expected to drill its own holes into the sidewalls of the tube (thickness of 0.2 mm). Therefore gas losses will be minimal and an average pressure lower than 10^{-3} mbar is achieved. To further reduce gas-losses and to tune the interaction length to achieve phase-matching the tube can be squeezed.

First harmonics generated with this setup are shown in Fig. 3.7b. They were generated with uncompressed 30 fs pulses output pulses of the Femtopower-laser system (≈ 600 mJ)

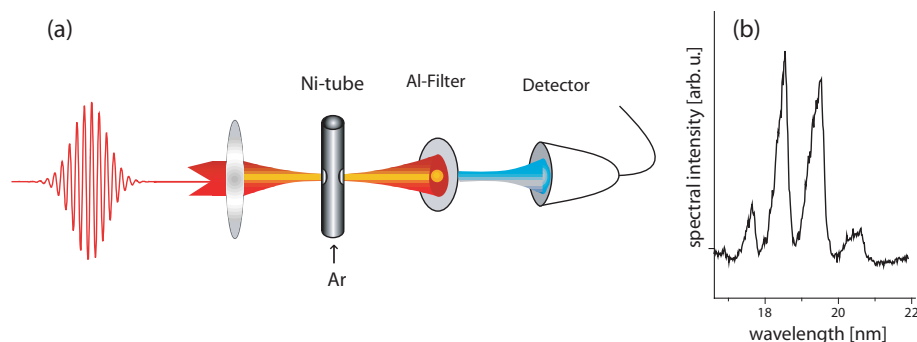


Figure 3.7: (a) Setup for high-harmonic generation in a gas-filled Ni-tube. The laser pulse drills its own holes into the sidewalls of the tube to limit gas losses. (b) First high harmonics generated with this setup. The detection of higher orders is still prevented by use of an Al-filter.

and an argon pressure of about 100 mbar. Presumably only part of the generated spectrum is visible as a $0.3 \mu\text{m}$ thick aluminum filter was used that absorbs radiation below 17 nm. Higher orders down to 10 nm are expected after pulse compression (see Chapter 2) and replacement of the Al-filter with a Zr-filter (Zr-filters have a transmission between 5 nm and 18 nm [123]).

In the next paragraph, a new conversion geometry is introduced that has a much longer interaction length. In this setup, optimal phase matching conditions can be realized in a gas-filled hollow-fiber.

3.4.2 Gas-filled Hollow-Core Fiber

In most experiments a gas jet is used as conversion medium in a moderately focused geometry. This way, a large number of harmonics up to the cut-off frequency can be generated. However, applications such as time-resolved spectroscopy require a large number of harmonic photons, preferably in a spectrally narrow region consisting only of a single isolated harmonic. In gas-jets all XUV photons are more or less evenly distributed among the plateau harmonics limiting the isolation of single harmonics. Different experiments have already been carried out to enhance the harmonic output using adaptive pulse shaping techniques, but the overall structure of the broad harmonic plateau is still present [124–126].

The more elegant alternative to spectral filtering is to only generate the radiation that is needed in the first place by manipulating the frequency conversion process itself. This could be done using designed driver pulses to exert control over the single atom response of the conversion medium. But as will be shown in the next chapter this effect has not been observed in gas jets so far [127].

However, it has already been successfully demonstrated that one can take advantage of phase-matching effects if the generation takes place inside a wave-guiding structure like a gas-filled hollow fiber. As will be shown below, the guiding geometry can counteract the phase-mismatch of the fundamental beam for a limited range of generated harmonics. This will limit the conversion process to a narrow spectral region with high efficiency [128].

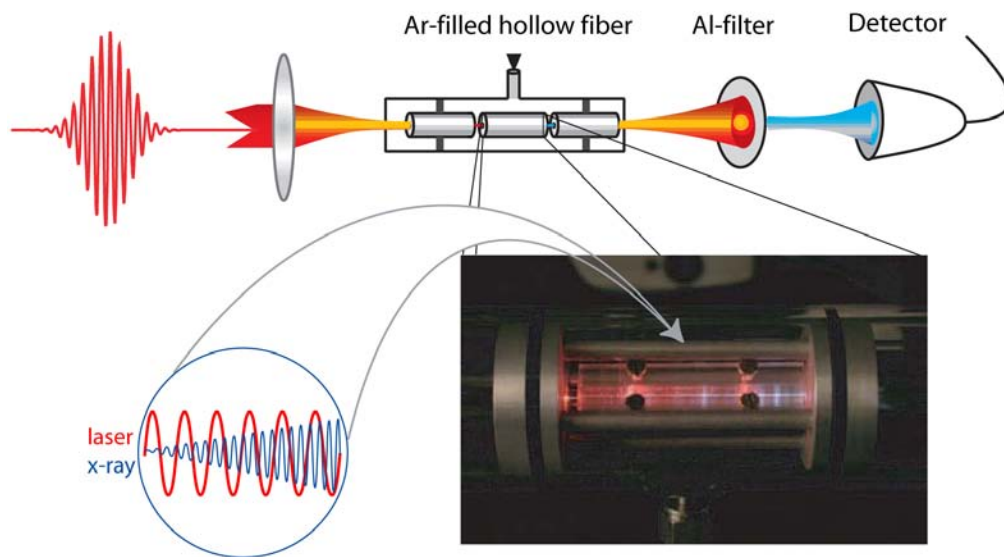


Figure 3.8: High-harmonic generation in a gas-filled hollow fiber. Due to guiding of the laser light by the waveguide structure phase-matched generation of high-harmonics is possible. In case of phase-matching the high harmonic signal interferes constructively and the yield is increased.

The basic setup for high-harmonic generation in a hollow-core fiber is illustrated in Fig. 3.8. A similar setup was also used by Rundquist et al. [128] who demonstrated phase-matched generation of high-harmonic radiation in a hollow fiber for the first time. The fiber of an overall length of 10 cm is divided into three separate parts to allow the middle part to be filled with argon at a constant pressure while the density in the outer parts drops down to vacuum level. This guarantees minimal absorption losses for harmonics that are generated in the middle part and limits plasma build-up at the entrance of the fiber that will defocus and distort the laser pulses. The fiber pieces have an inner diameter of $140 \mu\text{m}$. Gas consumption is low as the outer sections act as differential pumping stages.

Phase-matching for the harmonic order q is achieved when the phase velocity of the driving laser pulse matches that of the harmonic. In terms of the wavevector k the following condition must be met:

$$\Delta k = qk_{\text{laser}} - k_{x\text{-ray}} = 0. \quad (3.9)$$

The interaction with the conversion medium and the confinement of the waveguide structure influences the propagation of laser pulses—they modify the phase velocity.

Different contributions have to be considered:

- the **neutral dispersion** $n(\lambda)$
- **plasma-dispersion:** free electrons are generated as gas is ionized in the intense field.
- **waveguide dispersion:** the wavevector k is modified due to partial reflections within the waveguide structure

Including these contributions the wavevector $k(\lambda)$ can be written:

$$k(\lambda) = k_{vac.}(\lambda) + k_{disp.}(\lambda) + k_{plasma}(\lambda) + k_{geom.}(\lambda), \quad (3.10)$$

where $k_{vac.} = 2\pi/\lambda$ is the wavevector in free space. Each of these contributions are now discussed in more detail.

Neutral Dispersion

The amount of neutral dispersion is dependent on the pressure and the type of gas used. It can be written as:

$$k_{disp.}(\lambda) = \frac{2\pi N_a \delta(\lambda)}{\lambda}. \quad (3.11)$$

N_a is the atom density and $\delta(\lambda)$ depends on the neutral gas dispersion. In the visible range the refractive index is generally higher than in the soft-x-ray regime where the high harmonics are generated, therefore:

$$\Delta k_{disp} > 0. \quad (3.12)$$

Plasma Dispersion

A cloud of free electrons starts to oscillate in the laser field with respect to the embedded ionic centers. The refractive index of this system is defined by:

$$n_{plasma}(\omega) = \sqrt{1 - \left(\frac{\omega_p}{\omega}\right)^2}, \quad (3.13)$$

where ω_p is the plasma frequency that is the resonance frequency of forced oscillation of the plasma. It is given by:

$$\omega_p^2 = \frac{e^2 N_e}{\varepsilon_0 m_e}, \quad (3.14)$$

where e is the unit charge, N_e the free-electron density. ε_0 is the vacuum dielectric constant and m_e is the electron mass. As long as the relative amount of free electrons stays small, Eq. (3.13) can be linearly approximated:

$$n_{plasma}(\omega) \simeq 1 - \frac{1}{2} \left(\frac{\omega_p}{\omega}\right)^2. \quad (3.15)$$

By insertion of Eq. (3.14) the contribution-term to the wavevector k can then be expressed in terms of λ :

$$\Delta k_{plasma}(\lambda) = \frac{2\pi \Delta n(\lambda)}{\lambda} = -\frac{e^2 N_e \lambda}{4\pi \varepsilon_0 m_e c^2}. \quad (3.16)$$

Using the definition of the classical electron radius

$$r_e = \frac{1}{4\pi\epsilon_0} \frac{e^2}{m_e c^2}, \quad (3.17)$$

Eq. (3.16) can be simplified to:

$$\Delta k_{plasma}(\lambda) = -N_e r_e \lambda. \quad (3.18)$$

The plasma contribution will be negative:

$$\Delta k_{plasma} < 0. \quad (3.19)$$

As plasma is generated during the fast rise time of the electric field the pulse will feel the effect of a fast changing index of refraction $\Delta n < 0$. In analogy to the description of self-phase modulation (see 1.3.2) the laser pulse will experience a blueshift. The corresponding redshift is not observed, as the plasma recombination time is much longer than the pulse duration and of the order of nanoseconds. This behavior can be observed during HHG and controlled by changing the gas-pressure.

Waveguide Dispersion

When a laser beam travels inside a guiding structure a combination of discrete waveguide modes EH_{nl} is excited [129]. The transverse components of these modes are standing waves confined by the inner walls of the waveguide. The wavevector \vec{k}_0 therefore consists of a transverse k_{trans} and a longitudinal component k_z that is shorter compared to the freespace k -vector. The smaller the diameter of the waveguide compared to the wavelength of the guided light, the larger is the modification of the wavevector. The phase velocity along the waveguide will therefore become frequency-dependent.

The following relation is valid:

$$k_z^2 = k_0^2 - k_{trans}^2 = \left(\frac{2\pi}{\lambda}\right)^2 - \left(\frac{u_{nm}}{a}\right)^2, \quad (3.20)$$

with a as the inner radius of the hollow fiber and u_{nm} as the m th root of the Bessel function $J_{n-1}(z)$ corresponding to a discrete propagation mode in the fiber [129].

k_z can be approximated to be:

$$k_z = \frac{2\pi}{\lambda} \sqrt{1 - \left(\frac{u_{nm}\lambda}{2\pi a}\right)^2} \approx \frac{2\pi}{\lambda} \left[1 - \left(\frac{1}{2} \frac{u_{nm}\lambda}{2\pi a}\right)^2\right], \quad (3.21)$$

if the radius a of the capillary is much larger than the wavelength λ . The corresponding wavevector contribution of the waveguide is:

$$k_{geom.}(\lambda) = -\frac{u_{nm}^2 \lambda}{4\pi a^2} < 0. \quad (3.22)$$

Including all contributions the k -vector inside a gas-filled fiber is then approximately given by:

$$k \approx \frac{2\pi}{\lambda} + \frac{2\pi N_a \delta(\lambda)}{\lambda} - N_e r_e \lambda - \frac{u_{nm}^2 \lambda}{4\pi a^2}. \quad (3.23)$$

In Eq. (3.23) there are a number of different adjustable parameters by which the phase-matching condition Eq. (3.9) can be engineered: wavelength, gas pressure, gas species, wave-guide size and spatial mode.

As the different contributions vary in sign the right set of parameters can fulfill the phase-matching condition Eq. (3.9). In the case of perfect phase-matching the driving laser pulse continuously generates new harmonic light and the electric field of each phase-matched harmonic can add up constructively to the copropagating harmonic radiation generated earlier. With linear increasing field amplitudes the detected harmonic intensity will increase quadratically with the length of the interaction medium.

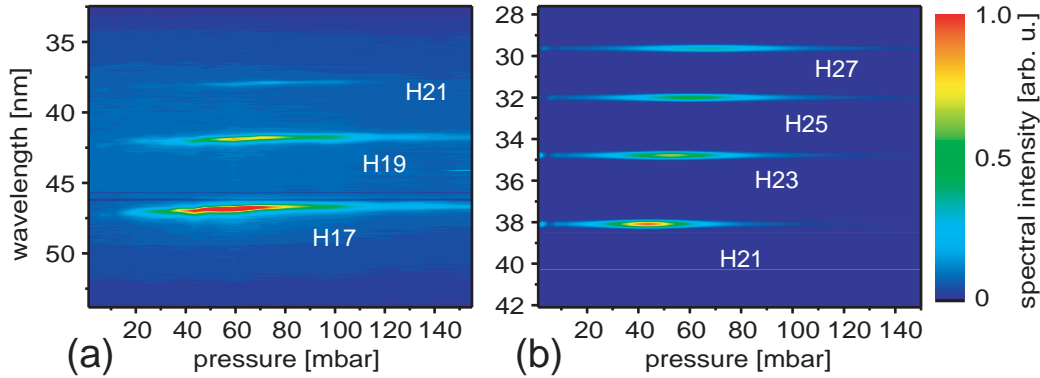


Figure 3.9: (a) Phase-matched generation of high-order harmonics in a hollow fiber. The gas pressure is varied to control the wavevector mismatch Δk in the high-harmonic generation process. At certain gas pressures perfect phase matching can be realized and the conversion efficiency of a particular harmonic is maximized. The optimum pressure shifts with the harmonic order as expected from Eq. (3.9). (b) This behaviour is verified by a simulation of Eq. (3.9) Since refractive index values were not available for simulation in the experimental wavelength region, the simulation was carried out for higher harmonic orders.

Generally, the pressure is varied to achieve phase-matching for a certain range of harmonics but as we will see in Section 4.3, the waveguide-dispersion can also be changed by excitation of different fiber-modes. Fig. 3.9 shows a pressure scan for HHG under phase-matching conditions in the gas-filled hollow-fiber. A simulation was performed using the results of Eq. (3.23). Both the experiment and the simulation show an expected increase of the optimum pressure for rising harmonic orders.

This is also the main advantage of this setup compared to the gas-jet setup. As the phase-mismatch can be minimized, the only remaining limit for efficient high-harmonic generation is absorption [130]. As photon energies in the soft x-ray range have large photoionization cross-sections σ in most materials, this aspect also has to be considered as

it will limit the conversion efficiency for long fiber lengths. The absorption length L_{abs} (the distance after which the intensity of light propagating in an absorbing medium has dropped to $1/e$) is given by:

$$L_{abs} = \frac{1}{\rho\sigma}, \quad (3.24)$$

where ρ denotes the particle density. In [130] it is shown that even for infinite coherence lengths, as in the case of perfect phase matching, the HH emission saturates as soon as the medium length is longer than a few L_{abs} , since harmonics emitted beyond that are reabsorbed. This limits the reasonable length of fibers to few centimeters.

Another method to extend phase matching to a wider range of frequencies is called quasi-phase matching. The interacting medium, in this case a hollow fiber, can be modulated to favor or disfavor harmonic generation in limited regions of the waveguide. Harmonics are generated only in regions where their signal will add constructively. The regions of destructive interference are suppressed. With this method enhancement of the high-harmonic output on the order of 10^2 to 10^3 can be achieved [128].

Quasi-phase matching can also be used to counteract the effect of plasma-induced defocusing, allowing high laser intensities to be achieved in a fully ionized gas medium. The large phase-mismatch associated with ionization can be partially compensated and harmonic generation in argon up to 250 eV was observed [131] (an extension of 100 eV compared to results in a gas-jet setup).

The high-harmonic output of hollow fibers has extraordinary spatial coherence properties [132]. The Fiber acts as spatial filter for the driving laser pulse. The enhanced spatial properties are transferred to the harmonic beam. This is also the case for high-harmonic generation under unguided conditions but is subject to the spatial beam profile of the fundamental pulse and depends on the position of the focus relative to the conversion medium.

This type of control of the generation medium for enhanced high-harmonic generation will be complemented by also tailoring the driving laser pulse itself. In the next chapter it will be demonstrated that in addition to the enhancement of the overall harmonic efficiency and the isolation of a single harmonic [93], more general possibilities to shape the XUV spectrum are possible. The optimization experiments in the next chapter will successfully demonstrate that the spectral shape of high harmonics can be controlled by temporal-only pulse shaping [127].

3.4.3 Water Microdroplets

As was shown above, the generation of high harmonics can be increased quadratically for perfect phase-matching conditions if the length of the interaction medium is increased. This is also valid for an increase of the density of the conversion medium. Phase-matching in non-guided geometries is usually limited by plasma-build up. However, an increased number of emission centers in high density media will also enhance the conversion efficiency.

Higher densities of solid or liquid systems make them valuable conversion media [133, 134]. In simple conversion geometries HHG in atomic systems already comes close

to experimental limits. More extended and complex systems like molecules have to be studied as they present large recombination targets and have a high number of inner degrees of freedom that provide further means of optimization.

As an alternative to gas-targets water microdroplets will be taken as high-density medium in this subsection for HHG. The spherical shape of the droplets will focus the incident laser radiation to a small volume inside the droplet, which leads to laser-induced breakdown (LIB [135, 136]). Plasma is created in the “hot spot” absorbing further laser light and the plasma grows until the droplet will explode. Therefore, microdroplets have been widely used as incoherent sources of soft x-rays that are generated as plasma recombination light with high efficiency [137, 138]. In comparison to the directional emission of the coherent high harmonics such sources have the drawback that the radiation will be emitted isotropically over 4π steradians (see also Section 3.6).

A pump-drive scheme with two laser pulses allows to disperse the water droplet before it interacts with a second laser pulse that drives the high-harmonic generation process. Therefore it becomes possible to probe regimes of different particle densities. Highly charged water clusters can form during a laser driven explosion of the droplets. Such clusters are extensively studied with respect to their unique frequency conversion properties [139–141]. In some of these studies it has been shown that clusters can be used to reach conversion efficiencies for incoherent plasma radiation comparable to those obtained in solid state systems. HHG in clustered media turned out to occur at smaller intensities, to have a higher photon energy cutoff and to saturate at higher laser intensities as compared to monoatomic targets.

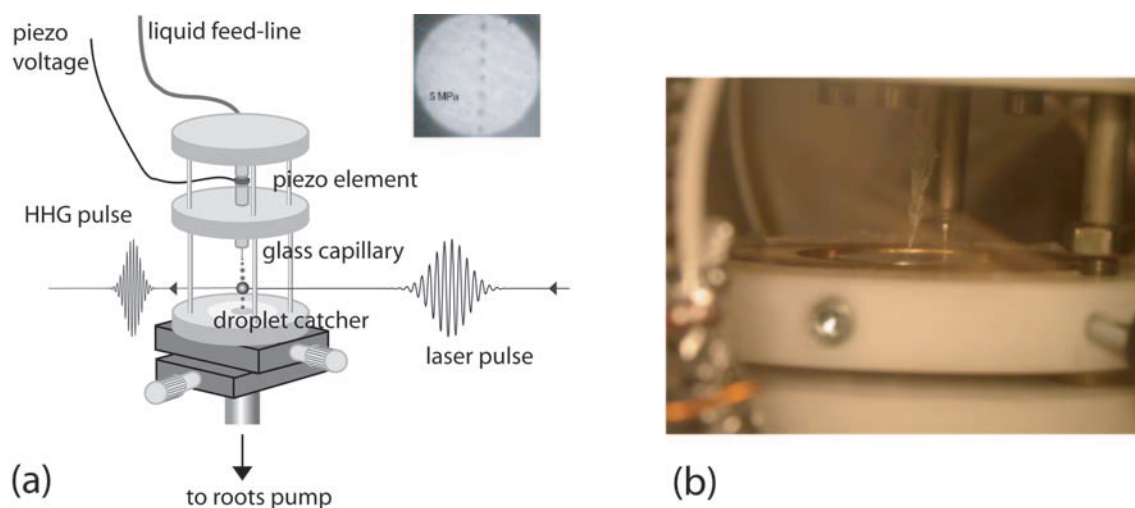


Figure 3.10: (a) Schematic setup. The glass capillary is mounted inside a vacuum chamber. The water droplet jet (inset) is produced vertically downwards. A piezo element can be used to control the droplet repetition rate. Droplets not used in the experiment are removed by direct pumping with a roots pump. Laser pulses interact with the water droplet jet below the capillary exit to induce plasma luminescence or HHG. (b) Picture of an ice-stalagmite that grows towards the glass capillary. External heating of the droplet-catcher tube was necessary for prevention.

Setup

The water microdroplets are produced by a glass capillary of 10 μm inner diameter (Microjet Components (Sweden)) backed with liquid water (see Fig. 3.10a). With a controlled fluid pump the pressure can be kept constant in a range of 2 to 5 MPa. The capillary is mounted vertically such that the water leaves at the lowermost end. A continuous water jet streams out of the capillary. After a certain propagation distance droplets are formed due to the Rayleigh-Taylor instability. To ensure reproducible droplet sizes, the capillary is equipped with a piezo transducer to modulate its diameter. Applying a high-frequency voltage of 15 V results in a fixed droplet repetition rate. The frequency has to be close to the natural repetition rate given by the Rayleigh-Taylor instability and were chosen between 0.9 and 1.1 MHz. The laser system was synchronized to the droplet repetition rate in a way that every laser pulse could interact with one microdroplet.

The inset of Fig. 3.10a shows a photograph of the droplet jet that was taken with a microscope objective and a CCD camera. The jet was illuminated by laser pulses incident on a screen placed behind the jet. A backing pressure of 5 MPa and a repetition rate of 1 MHz were used. When the backing pressure is increased, larger droplet diameters are obtained. On the other hand, increasing the piezo-frequency results in smaller droplets.

The capillary is mounted inside the vacuum chamber where a background pressure of $\sim 2 \times 10^{-3}$ mbar was achieved. The differential pumping stages along the way to the spectrometer lowered the pressure further until it reached about 10^{-5} mbar at the x-ray spectrometer. At a distance of about 5 mm below the exit of the capillary, the laser beam interacts with the droplet jet (see Fig. 3.10a). Focusing with a 20 cm focal length lens provides laser intensities of the order of 5×10^{14} W/cm². Further down, after about 40 mm, the jet enters through a small diameter aperture (0.5 mm) into a separate “catcher” compartment, which is kept evacuated directly by a roots pump. In order not to damage the pumps, a liquid nitrogen cooled cold trap is installed between the chamber and the pump. As liquid water at room temperature brought into vacuum tends to freeze and grow stalagmites [142] (Fig. 3.10b) where it hits an obstacle, it is important to keep the catcher at an elevated temperature of about 350 K. If the temperature is too low, ice stalagmites will grow all the way up to the exit of the capillary, preventing stable operation of the jet. If the fragile glass capillary will be frozen from the inside, permanent damage occurs.

For these measurements the emitted XUV radiation was detected with two different monochromators for two different photon energy ranges. The low energy radiation is characterized by a home-built Seya-Namioka monochromator (referred to as MC1) with a spherical grating. The full scanning range provides access to harmonic orders three (H3) to nineteen (H19). A scintillator (Na-salicylate) behind the exit slit is used to convert the XUV radiation into the visible. A photomultiplier is then used to acquire the spectrum as the grating rotates. The signal is DC-converted by a boxcar-averager which is read out by a computer. The other monochromator (MC2) was used to record 20 eV (H13) to around 80 eV corresponding to H51 and is already described in Section 3.4.1.

Fig. 3.10a displays a schematic view of the droplet system. The system is aligned in such a way that the laser beam propagates directly into the spectrometer. For detecting harmonic orders greater than H17, two aluminum filters (thicknesses 0.3 and 0.8 μm) [143] were inserted in order to block the fundamental light.

The droplet-generating system was operated at a backing pressure of 5 MPa. Under these conditions water droplets with diameters of about 20 μm were produced. Fig. 3.11a is a photographic picture of a water droplet illuminated by different laser intensities. For the medium (center picture) and high intensities (lower picture) a BG40 filter was used to suppress the fundamental laser light. For very low intensity only the unperturbed spherical droplet is visible, while at increasingly higher intensities we observe bright light from the front face (towards the laser) of the droplet. Two possible explanations for this finding are:

- (1) Optical breakdown and plasma mirroring of the fundamental laser radiation close to the front face of the droplet or
- (2) plasma emission [144] from a backward directed emission plume of the droplet similar to the one reported in [145].

During first test-runs small stability problems with the water backing pressure were observed. The pressure varied by about 100 kPa within a period of about 1 second. This had the effect of a “heart beat” fluctuation of the droplet jet in relation to the synchronized laser-pulses. Due to this periodic delay the position where the laser hit the droplets moved by about half a droplet diameter. To minimize this fluctuation an additional water reservoir was included after the fluid pump. This could reduce the “beating”-amplitude by about a factor of 5. However a slow, aperiodic drift was still observed over longer time scales (~ 15 minutes). To measure without this slow drift following results were therefore obtained without modulation of the piezo transducer, i.e. the jet was operated in the free-running Rayleigh-Taylor instability regime.

Regarding emission spectra, first results for single laser pulses interacting with the microdroplets are presented in Fig. 3.11b. Employing the spectrometer MC2, strong plasma recombination light emitted from the droplets is detected. Comparison with literature values [146, 147] reveals that the lines can be attributed to highly ionized oxygen (up to O^{5+}). The spectrum can only be observed for wavelengths longer than 17 nm, which is the L-edge of Al. No high-harmonic emission for orders H17 and higher could be observed using a single laser pulse. Switching to spectrometer MC1 without Al filters third-harmonic emission can faintly be observed. Single photon events of the fifth harmonic were recorded on the photomultiplier about each 5000 laser shots. No harmonic signal for higher orders is detected.

This situation changes dramatically when the pulse energy is distributed between two pulses. In a first approach, the Pockels cell of the regenerative amplifier was set to release two pulses spaced by the round-trip time of the laser cavity, which is 10 ns. The material dispersion corresponding to an additional round-trip of the second pulse results in an increase of its pulse duration to about 300 fs and a frequency upchirp. However, by switching from single pulse to this double pulse operation mode a large increase (by about three orders of magnitude) in harmonic generation efficiency could be observed for the third and the fifth harmonic. In Fig. 3.12 the harmonic emission spectra for lower orders (H3-H11) acquired using MC1 are shown.

In order to obtain a deeper insight into the droplet dynamics, a delay stage was set up to control the time delay between pump and driver pulse. For these pump-drive experiments, a noncollinear excitation geometry was used. The pump laser pulse does not enter the

spectrometer directly, while the driver one does. XUV emission characteristics from the water droplets change qualitatively at a certain delay time (about 650 ps), which is shown in Fig. 3.13. At early times, only plasma emission can be observed (in second diffraction order) while at later times HHG is present almost exclusively. At a time delay of about 650 ps, a rapid transition occurs leading to inhibition of plasma emission and promotion of HHG.

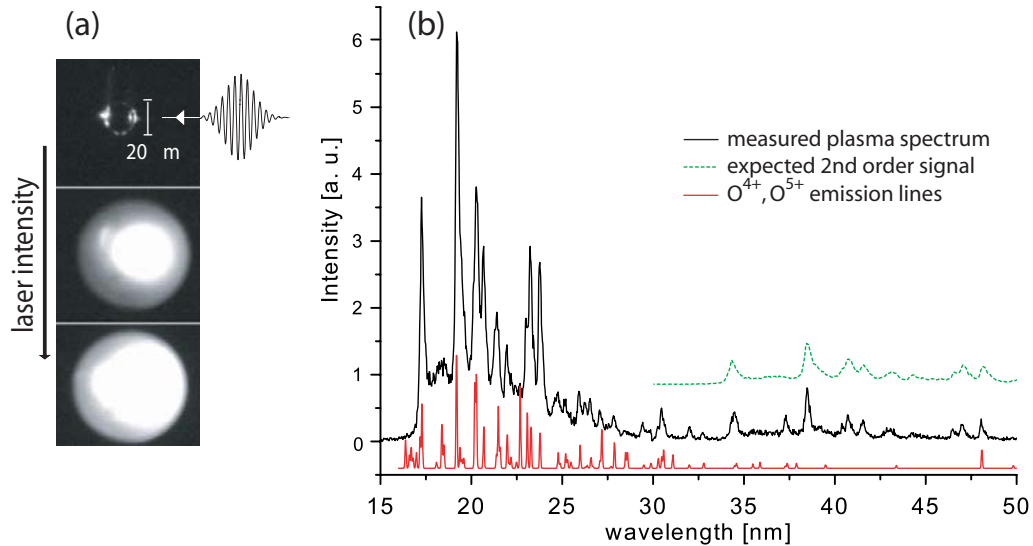


Figure 3.11: (a) Photographic images of water droplets for irradiation with different laser intensities. Laser pulses arrive from the right hand side as indicated. Intensity increases from top to bottom. The top picture shows the unperturbed droplet. The center and bottom picture were taken through a BG40 filter to remove contributions of the fundamental laser radiation. An increasing amount of light is emitted from the laser input side of the droplet. (b) Typical plasma emission spectrum observed in the experiments for short pump-drive pulse delays. Literature values for emission lines of highly ionized oxygen (O^{4+} , O^{5+}) are plotted underneath. The cutoff for frequencies below 17 nm is due to the absorption edge of the aluminum filter. Signal at longer wavelengths is partly caused by the second diffraction order of the spectrometer grating. For better visibility, the detected first order signal has been manually converted to second order (dotted line).

This observed behavior can be explained as follows:

I) The first pulse ionizes the water molecules creating a hot and dense plasma with nearly solid state density. Dense plasmas are well known as efficient emitters of line radiation. If the delay between the two pulses is small both pulses contribute evenly to the heating of the plasma.

II) The hot and dense plasma starts to expand immediately. The second pulse interacts with a less dense plasma resulting in a reduced conversion efficiency. Similar behavior has also been observed using Ar and Kr microdroplets. McNaught et al. [138] have measured a decay time of the plasma emission of a few hundreds of ps, which is in agreement with our observations.

III) After 600 ps the estimated molecular density results in an average distance between atoms that is greater than the classically calculated excursion length of the electron during HHG. This gives the electrons the chance to return to their parent ion without colliding

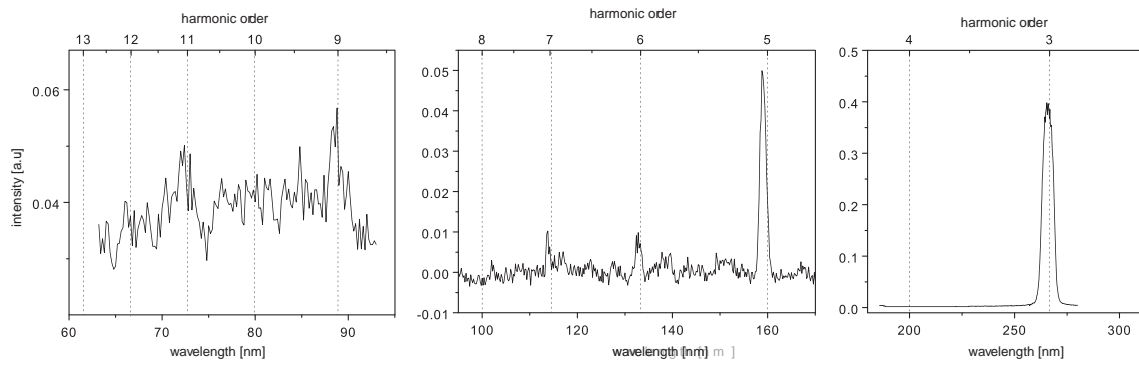


Figure 3.12: Lower-order harmonic emission spectra detected for droplets interacting with a double pulse (see text). Harmonics from order H3 up to H11 can be detected with decreasing emission strengths. The signal close to the sixth harmonic can be attributed to a strong plasma line.

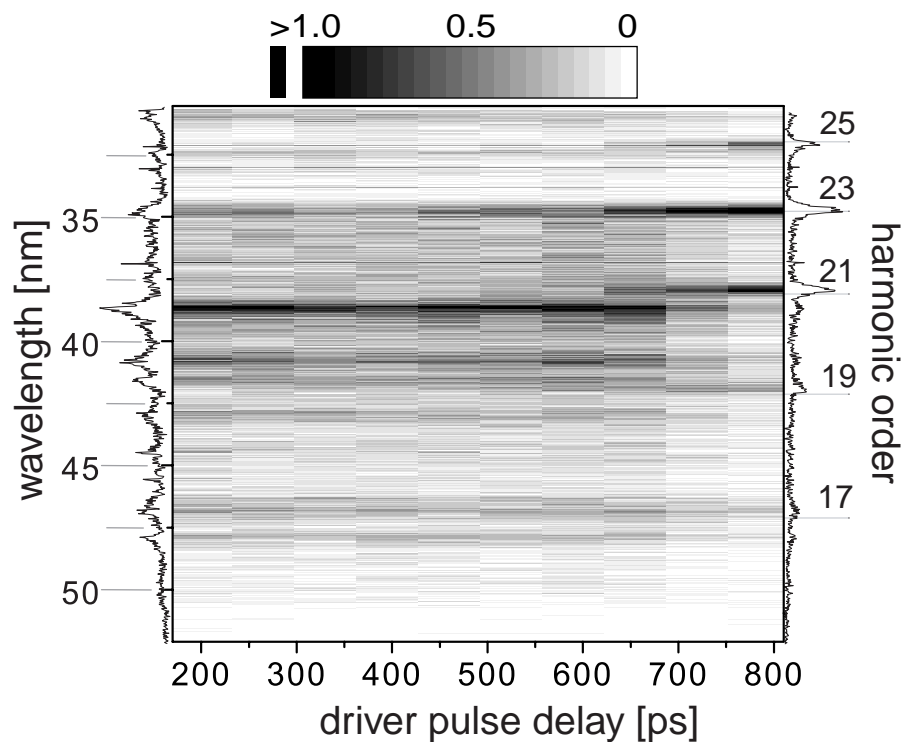


Figure 3.13: Transient XUV-emission spectrum for the pump-drive setup. A transition occurs at ≈ 650 ps from a regime where only plasma luminescence is detected (in second diffraction order) into a different one with high-harmonic generation being the dominant contribution to the spectrum.

with other molecules which would impair the generation of spatially and temporally coherent high-harmonic radiation. Besides the single particle response propagation effects play a major role in HHG.

Therefore a significant spatial and temporal distortion by the existing and newly generated plasma has to be considered.

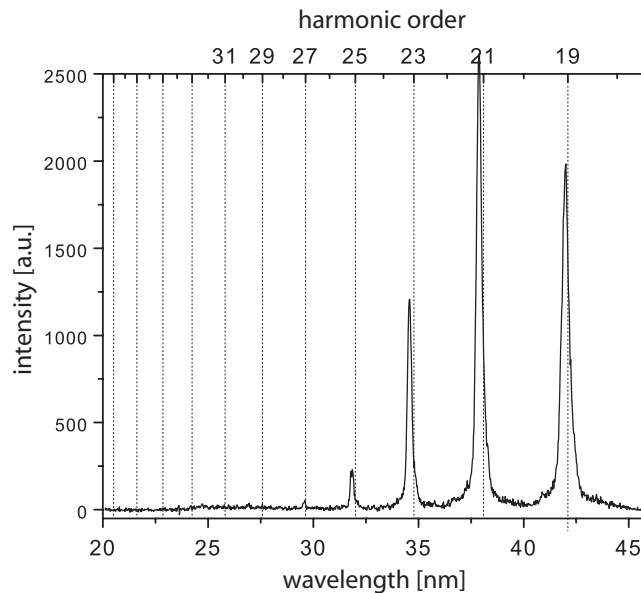


Figure 3.14: High harmonics in the cutoff region of the spectrum acquired at a time delay of ≈ 1 ns.

After about 1 ns the plasma generated by the combined action of the two pulses is subcritical and the generation of higher order harmonics is observed (Fig. 3.14). This explains why the increase in high-harmonic signal at a particular time delay coincides with the decline of plasma line emission, since effective plasma heating by the second pulse rules out its undisturbed propagation through the medium. Additionally, as long as the electron density is too high, phase-matching between the high-harmonic radiation and the fundamental is not possible over significant length scales.

Summary

The observation of high-harmonic radiation up to the 27th order in water microdroplets is reported for the first time [148]. This can be achieved only for slightly expanded droplets, whereas it is absent for laser interaction with unperturbed droplet targets. In the latter case, only plasma luminescence from highly charged states of oxygen (up to O^{5+}) can be observed. These highly ionized oxygen ions have been reported in earlier studies on the explosion of water clusters in intense light fields [149].

Depending on the delay of the driver pulse (generating harmonics) with respect to a pump pulse (expanding the droplet) a sharp transition can be observed from a regime (for short time delays) where only plasma recombination light is emitted into another region (at

longer time delays) where high-harmonic generation takes place with negligible contribution of plasma emission.

Using the pumpdrive setup it is possible to study high-harmonic generation in media of particle densities spanning the entire range from liquid state down to gaseous density. In order to push the conversion efficiency to the maximum, we must acquire knowledge about which are the maximum tolerable particle densities. On the other hand, once limitations to maximum density are encountered, the presented experimental environment will serve as a versatile tool and testbed in finding ways to overcome these problems. These studies will be the subject of future work.

In recent publications Strelkov et al. [150, 151] have calculated HH-spectra for different medium densities. A change in the harmonic properties is seen when the medium density exceeds a certain transition density, where the single-atom response is affected by neighboring ions of the medium analogue to the observed results in the droplet experiments. The transition density differs for the two (shorter and longer) quantum paths by about an order of magnitude. The latter effect leads, for ionic densities in the transition regime, to a shortening of the emitted high-harmonic attosecond pulses.

In comparison to high harmonics generated in the gas-jet setup the overall yield of high harmonics generated in water droplets was increased by over an order of magnitude. This is partly due to lower energies of the driver pulse (pump-probe setup has to be used in the case of microdroplets). The microdroplet setup allows the future study of fragmentation processes or high-harmonic generation for a range of different fluids that have not been investigated so far. The next section will also focus on the generation of high harmonics in more complex systems.

3.5 Optimization Schemes

Compared to other sources of short pulses of x-ray radiation high harmonics still have an unsurpassed quality of coherence. However, in terms of photon energy or peak-brightness large scale facilities with free-electron lasers attract a high number of experimenters. At the moment high-harmonics could just recently surpass the 1 keV energy threshold [103]. The conversion efficiency is still limited to $\eta = 10^{-4}$ [80] or 10^{-5} [81] with dropping values for higher energies. Promising ideas to overcome these limitations are welcome news. As will be seen in the following section, high-harmonics can be successfully applied as “weak” seed pulses in enhanced designs of x-ray lasers or for the the process of high-gain harmonic generation. Biegert et al. even use an attosecond pulse train as seed for enhanced harmonic generation [152]. However, there are still many other possibilities to increase the conversion efficiency.

Raising the number of particles that will emit harmonics will be constrained by the problem of reabsorption in the generating medium. As was shown in Section 3.4.2, this problem also limits the phase-matched generation in gas-filled hollow fibers [130, 121] where long interaction lengths are required for maximal conversion yields. But even if absorption in the medium could be overcome by some means (e.g. using dark resonances), there would be another severe fundamental limitation: Ionization of the medium effectively

extracts energy from the generating laser pulse without contributing to XUV-photon production.

It is not only the density of a medium that is important. Any kind of inner degree of freedom of a particle can be used to control and optimize a process like high-harmonic generation. For example, during the interaction of laser pulses with homopolar but isotopically asymmetric dimers, that have no inversion symmetry, both even and odd order harmonics can be observable [153].

In the case of simple atomic systems the electron always will have to recombine with its parent ion. More extended systems like clusters will have many different recombination centers available. To increase the probability of recombination two different ideas can be approached:

- more complex or extended systems are used as conversion medium, therefore the 'target' for electrons is increased as in the case of clusters or even molecules.
- the spreading of the electron wave function will be reduced to increase the probability that the returning electron will be found at the ionic core. This can be achieved by preparation of the initial electronic state.

This section features these ideas to overcome the limitations of HHG in simple atomic systems. Two theoretical approaches will focus on increased probability of harmonic emission for excited systems or specially prepared molecules. Finally, in a sense of an outlook and transition to the next chapter, the last part contains the possibilities of shaping the driver pulses.

3.5.1 HHG from Excited Electronic States

Here it will be shown that the efficiency of single attosecond pulse generation during atomic ionization by an intense few-optical-cycle laser pulse can be enhanced dramatically when preexcited electronic states are used. This is due to the slowed down spreading of the laser-driven free-electron wave packet.

The use of an extremely short laser pulse as a driver for high harmonic generation in gases [154, 155] is useful for obtaining single attosecond pulses. In these very short pulses the intensity increases significantly in a time comparable to the oscillation period of the electric field. Driven by such laser pulses atoms can be ionized during a short time, in fact within one optical cycle because of the strong dependence of the ionization rate on the magnitude of the electric field. The free-electron wave packet then moves outside the atom, accelerates, and can return to a parent ion and collide with it, giving rise to a single attosecond burst of radiation. The basic limitation for the efficiency of this process stems from the spreading of the free-electron wave packet. As the wave packet spreading rate is basically governed by the extent of its initial delocalization, the efficiency of attosecond pulse generation can be enhanced by choosing an appropriate initial electronic state [156].

Experimentally, the excited states can be populated with close to 100% efficiency by Stark-chirped rapid adiabatic passage (SCRAP [157]). The effect under consideration is illustrated in Fig. 3.15. An electron is ionized from the initial 2s-state of a hydrogen

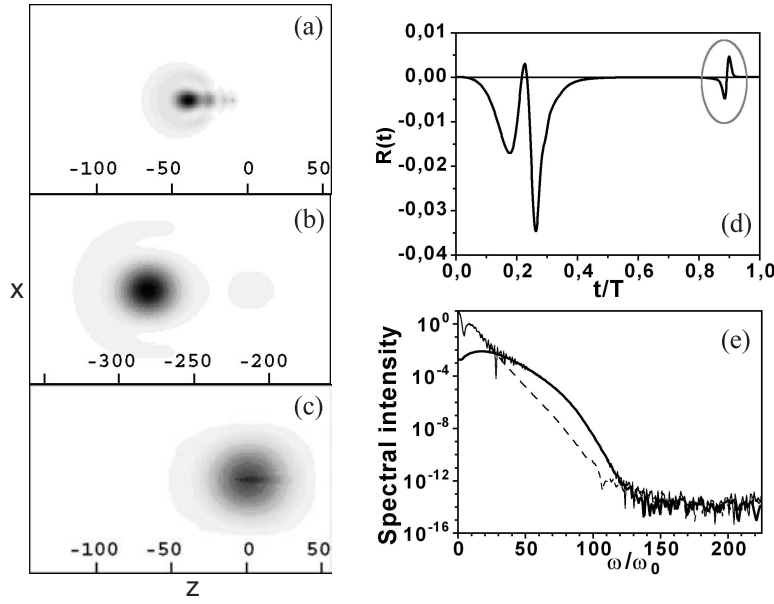


Figure 3.15: (a)-(c) Snapshots of the electron probability distribution in the xz -plane, (d) nonlinear atomic response, and (e) its power spectrum for the H atom ionized from the $2s$ -state by the laser pulse, see Eq. (3.25). Snapshots are taken (a) after ionization, $t = 0.31T$, (b) at the turning point, $t = 0.66T$, and (c) at the time of recollision, $t = 0.90T$ ($T = 2\pi/\omega_0$ is the optical cycle). Encircled region in (d) shows the attosecond pulse. In (e) the full spectrum (thin line) is shown along with the spectra corresponding to the motion before (dashed line) and after (thick line) the turning point.

atom by an optical pulse with linearly polarized electric field along the z -direction. The evolution of the electron wave packet was obtained in a 3D numerical simulation using the dipole approximation. It was performed using a standard split-operator technique with FFT [95]. In these simulations, a moving frame which follows the motion of the wave packet was used to allow a much smaller grid than needed for simulations in the laboratory frame. The electric field, that was used for the simulation is given by (in atomic units):

$$E(t) = 2 \exp[-5(\omega_0 t / 2\pi - 1)^4] \sin \omega_0 t. \quad (3.25)$$

(The frequency of the field $\omega_0 = 0.114$ (≈ 3.1 eV) was chosen to corresponds to the second harmonic of a Ti:sapphire laser). The fast ionization during a small fraction of the optical cycle results in the formation of a single free-electron wave packet having an almost spherically symmetric shape (Fig. 3.15a) that is retained in the course of acceleration and quantum-mechanical diffusion (Figs. 3.15b and 3.15c).

Recollision with the Coulomb center occurs after more than half the optical cycle. The time dependence of the dipole acceleration $\mu(t)$ and its spectrum are plotted in Figs. 3.15d and 3.15e. The attosecond pulse (encircled region in Fig. 3.15d) is produced when the accelerated wave packet passes the parent ion. Figure 3.15e shows the full spectrum along with the partial spectra of the atomic response corresponding to the wave packet motion before and after the turning point. Three frequency domains are visible due to radiation of three different groups of electrons and can be clearly distinguished in the

spectrum.

The low-frequency part of the spectrum (approximately up to the 40-th harmonic) is emitted, primarily, when electrons detach from the atom. The central part of the spectrum (harmonic numbers N ranging from 40 to 120) is due to acceleration of the bulk of the returning electrons. Finally, the hardest radiation (the high-frequency plateau in the region of the harmonics with numbers $N > 120$) is produced by a very small group of electrons in the close vicinity of the Coulomb singularity (i.e. with a small impact parameter), that most strongly interact with the Coulomb potential. In the following, the small contribution to the attosecond pulse that is caused by these strongly scattered electrons will be disregarded.

The shape of the attosecond burst can then be analytically calculated by assuming that the electron is detached from the atom in the regime of fast Coulomb-barrier-suppression ionization [82]. In addition, the amplitude of the electric field (Eq. (3.25)) changes significantly within one optical cycle. Thus, it will be assumed that the Coulomb potential ‘opens’ during a time that is much less than the period of variation of the wave function of the unperturbed atomic state. In the example given above, complete electron detachment occurs during a small fraction of the optical cycle whose frequency $\omega_0 = 0.114$ (≈ 3.1 eV) is comparable to the 2s state intrinsic frequency equal to 0.125. It is then natural to suppose that the electron wave packet outside the atom remains almost unchanged. Note, that this case of high-harmonic generation in a laser pulse with quickly increasing intensity is very much different from the commonly treated high-harmonic regime, in which only a part of the electron wave packet is emitted each half-cycle of the driving field. Here, the high-frequency radiation is not produced via continuum-bound transitions (leading to the cut-off law Eq. (3.3)) but via continuum-continuum transitions [158]. To find the further evolution of the wave packet, the strong-field approximation was used based on the fact that at laser intensities well above those for the multiphoton ionization regime the electron motion is dominated by the laser field. In this case one may neglect the Coulomb field (see, e.g., [159]) [160].

With these assumptions the shape of the wave packet of the excited state n , $\Psi_n(r, t)$, at the time of its recollision with an ion can be calculated (see [161] for full equation).

The electron density in the center of the wave packet $|\Psi_n(0, t)|^2$ in a wide time interval is plotted in Fig. 3.16a for $n = 1, 2$, and 3. Clearly, in a time much shorter than the optical cycle (e.g., at $t \geq 12$ for $n = 2$ and $t \geq 20$ for $n = 3$), the electron density in the center of the wave packet for the ground initial state drops below the one obtained for the excited states. This is due to stronger localization of the ground state resulting in faster spreading of the wave packet moving outside the atom.

This statement is evidently true for Rydberg states also. However, because of small initial electron density in the center of the wave function with $n \gg 1$, the characteristic time in which $|\Psi_1(0, t)|^2$ drops down to $|\Psi_n(0, t)|^2$ may be much longer than the time interval from ionization to recollision. Thus, it can be concluded that for each given laser frequency the most favorable excited atomic state with $n = n^*$ exists to ensure maximal density of the electrons participating in the recollision-induced bremsstrahlung. From Fig. 3.16a it follows that $n^* = 3$ meets this condition when the hydrogen atom is ionized by radiation at the fundamental frequency of a Ti:sapphire laser, and $n^* = 2$ for its second

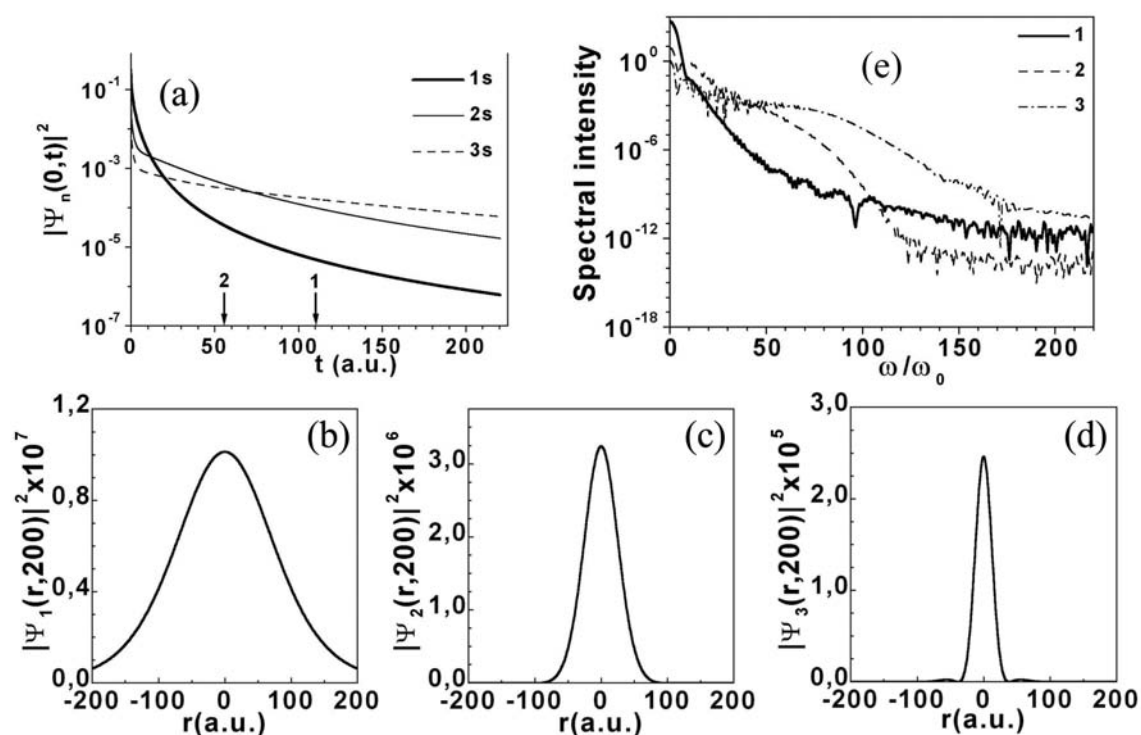


Figure 3.16: (a) Time profile of the electron probability density in the center of the wave packet for $n = 1$ (thick line), $n = 2$ (thin line), and $n = 3$ (dashed line). Arrows indicate the optical period of radiation with (1) $\lambda = 800$ nm and (2) $\lambda = 400$ nm. (b)-(d) Free-electron probability distribution at $t = 200$ a.u. [161]. (e) 3D numerical results for radiation spectra of the H atom ionized by the laser pulse (Eq. (3.25)) from the s-states with $n = 1$ (solid line), $n = 2$ (dashed line), and $n = 3$ (dash-dotted line).

harmonic.

As is seen in Fig. 3.16e, which gives the calculated emission spectra for $n = 1 - 3$, the conversion efficiency can be increased tremendously in certain spectral regions for higher order excited states compared to the emission of the ground state.

3.5.2 HHG in Expanding Molecules

High-order harmonic generation (HHG) is limited by the probability of recombination of the returning electron with the parent ion. The internuclear distance of simplest diatomic molecules, determining differently delocalized initial electronic states, can be used to enhance the HHG conversion efficiency exceeding the atomic one.

Since the process of HHG is understood very well for atomic systems, it is all the less understandable how little is known about HHG in more extended, complex systems. Especially molecular systems can easily replace rare gases in gas-jet setups. They will provide means of optimization of the IR-XUV-conversion process which are beyond the possibilities of their simple atomic counterparts. Orientation and internuclear distance will be additional degrees of freedom.

It has been demonstrated that harmonic generation in molecular media is slightly enhanced by inducing alignment [162, 163]. However, it remained unclear in these works whether molecular media could be any more efficient than atomic ones. There have also been experiments which showed that indeed molecules provide greater conversion efficiencies than atoms in a sense that they show a weaker dependence on the degree of elliptical polarization of the driving field [164, 165].

There are already theoretical studies that HHG in a molecular system is enhanced by an order of magnitude compared to atomic systems. It is known from theory [166] that cross-correlation of an XUV and a strong IR-pulse in a molecule aligned along the electric field vector can drastically increase the HHG efficiency by optimizing the ionization step.

Similar to the idea of the previous section the propagation of the electron in the continuum will be modified to enhance HHG. The conversion efficiency from IR into the XUV can be increased by up to a factor of 10 by manipulating the internuclear distance of a diatomic molecule and thereby influencing its electronic wave function prior to ionization.

As model system H_2^+ was chosen for the reason of simplicity. As a first step, the nuclear degrees of freedom were ignored, i.e. the molecular vibrational and rotational motion was frozen. Since laser pulses of 17 fs duration are used, this approximation is not valid for the H_2^+ molecule but would surely apply for heavier molecules.

Consequently, the Hamiltonian in the dipole approximation and velocity gauge in atomic units ($\hbar = e = m = 1$) is written as:

$$H = \frac{\vec{p}^2}{2} + \vec{p}\vec{A}(t) + V(\vec{r}), \quad (3.26)$$

for an electron under the influence of a stationary molecular potential $V(\vec{r})$ and the time-dependent vector potential $\vec{A}(t)$. The molecular potential was considered to be a two-center softened Coulomb potential

$$V(\vec{r}) = \frac{-1}{\sqrt{x^2 + (y - d/2)^2 + a}} + \frac{-1}{\sqrt{x^2 + (y + d/2)^2 + a}}, \quad (3.27)$$

where the smoothing parameter a was set to 0.5. The molecule was aligned along the y -direction with internuclear distance d .

The time-dependent Schrödinger equation was solved on a two-dimensional grid in spatial coordinates x and y . Propagation in time was again accomplished by means of the split-step operator technique [167, 95]. The grid comprised an area of 410 by 205 atomic units (a.u.) with absorbing boundaries. This size was carefully chosen to keep all relevant trajectories of the electrons within its boundaries. The ponderomotive radius $a_0 = E/\omega^2 = 38.5$ was calculated for the peak electric field strength and is much smaller than the dimensions of the grid. The ground state was propagated in time under the action of the AC electric laser field. The \sin^2 -shaped laser pulses were linearly polarized along x , thus perpendicular to the molecular axis. Their duration (FWHM-intensity) was 722 a.u. (17 fs) with an angular frequency centered around 0.057 a.u. corresponding to 800 nm wavelength. The peak electric field was set to 0.125 a.u. yielding an intensity of $5.5 \times 10^{14} \text{W/cm}^2$.

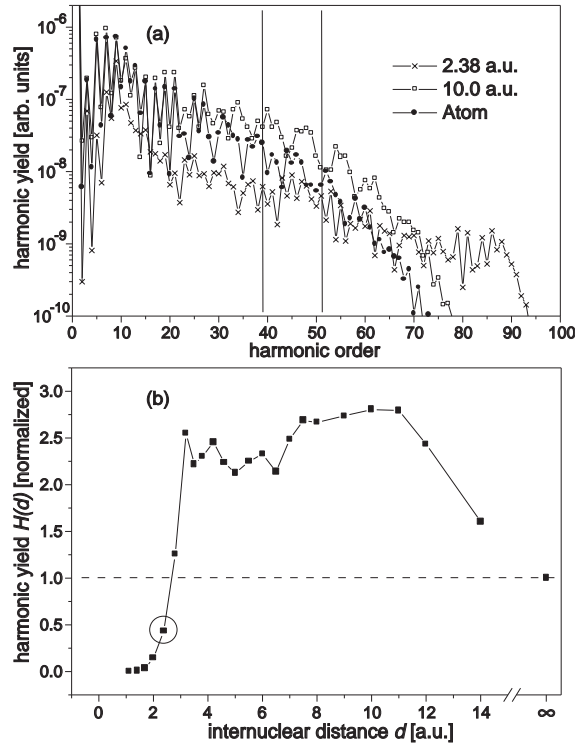


Figure 3.17: Harmonic spectra (a) and integrated XUV-emission (H39 to H51) versus internuclear distance d (b). In a broad range of d , HHG is more efficient by a factor of 3 than for the atomic case ($d = \infty$). Compared to the equilibrium bond length of the molecule (encircled data point) the enhancement is about one order of magnitude.

The nonlinear radiative response $\vec{S}_{nl}(t)$ of the molecule was calculated via the time-dependent dipole acceleration expectation value, using Ehrenfest's theorem [168]. From this quantity, the harmonic emission spectra were obtained by Fourier-transformation into the frequency domain. Fig. 3.17a shows harmonic spectra for various internuclear separations and for the atom in comparison. The high-frequency cutoff positions n_c agree with the analytical result $n_c = I_p + 3.17U_p$, where I_p and U_p are the ionization potential and the ponderomotive potential of the electron, respectively. Fig. 3.17a also shows that in the plateau region of the spectra there are significant differences in HHG yield. The change of cutoff position on the other hand is due to different ionization potentials I_p . When the summed harmonic yield in the indicated interval is plotted versus internuclear distance, a clear enhancement appears for intermediate values of d (Fig. 3.17b). We can explain this behaviour by considering two aspects of the HHG process, namely ionization of the active electron and propagation in the electric field. Since the ionization potential for H_2^+ into H_2^{2+} rapidly decreases for increasing values of $d < 2.5$ a.u., the harmonic yield rises from very small values as a result of increased probability for tunnel ionization with decreasing barrier height.

For larger values of d , the efficiency increases further until it starts to rapidly decrease at internuclear distances greater than 11 a.u. This latter feature can be understood by the following mechanism [156]: During propagation in the continuum, the electronic wave function suffers quantum mechanical dispersion (spreading). However, if the initial

state of the electron at the starting point of its orbit is largely delocalized (as is the case in molecules, particularly in elongated ones), the velocity of spreading will be reduced since the electronic wave packet has a narrower width in momentum space. Hence, a compact wave packet can finally return to the parent molecule and interact more efficiently with the molecular potential to generate bremsstrahlung. The probability for emission of a harmonic photon per ionization act can thus be effectively increased compared to the atom, where the ground state electronic wave function is more localized than in the optimal molecular case. Fig. 3.18 illustrates this behavior for the atomic and different molecular geometries. For one particular internuclear distance, the returning electronic wave packet shows the highest probability density at the positions of the nuclei, hence conversion is maximized. These snapshots of the electronic wave function have been calculated in the barrier-suppressed-ionization (BSI) field-strength regime [82] in order to obtain only a single ionization act and thus a single electronic wave packet for a clear demonstration of the effect. It is directly visible that an increased amount of delocalization of the real space wave function, which is connected to a reduced width of the momentum space wave function carries over to a reduced width of the returning electron wave packet in real space. This is understood from the fact that the electronic wave function is subject to quantum-mechanical dispersion of a free particle while it is moving far away from the ion. This finding directly expresses the necessity of research on molecules with regard to efficient coherent XUV generation. In particular, there are many more ways of optimizing and tailoring the electronic wave function in more complex molecular compounds than simple diatomic media can provide.

Pump-Drive Schemes

Let us now turn towards an idea to experimentally verify these stated predictions. In analogy to the work by Numico et al. [169] the following strategy is proposed: An initially aligned molecular sample [162] is illuminated with two ultrashort laser pulses. The first one serves as the pump pulse preparing a dissociative or vibrational molecular wave packet whereas the second time-delayed pulse is the driver for HHG, probing the non-linear dipole response of the system at different times corresponding to different internuclear distance situations. The time-delay dependence of the HHG yield can then be used to verify the dependence of HHG efficiency on internuclear distance. This ‘pump-drive’ scheme, can be implemented in various ways, two general ones of which are (1) resonant excitation to an excited molecular state or (2) non-resonant single (XUV) photon, multi-photon, or resonance enhanced multi-photon ionization (REMPI) to generate a time-dependent ionic molecular wave packet. In the following, the latter case will be considered.

Based on the given model Hamiltonian the potential energy curve for the model H_2^+ system was calculated. If we assume instantaneous ionization from the neutral H_2 (with a bond length of 1.4 a.u.) to the singly ionized molecule by a broadband ultrashort XUV-pulse, the nuclear wave packet is transferred from the H_2 (vibrational state $\nu=0$) to the H_2^+ potential energy curve. In this case, since the model H_2^+ molecule at an internuclear distance of 1.4 a.u. is a bound system, the wave packet motion succeeding ionization will be purely vibrational, not dissociative. The wave packet evolution $\Phi(d, t)$ on the H_2^+ curve is shown in Fig. 3.19. After ionization (defining time 0 in the wave packet evolution), it

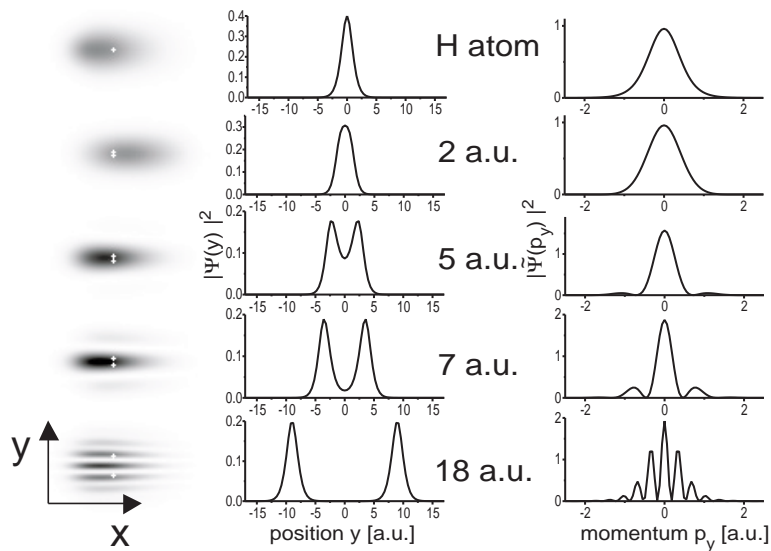


Figure 3.18: Snapshots of the two-dimensional wave function of the ionized and returning electron in a strong laser field (shown in grayscale) at the moment of interaction with the atomic/molecular parent ion. White dots represent the positions of the nuclei. For a particular interatomic separation, the wave function is most compact, indicating most efficient high-harmonic generation. Shown besides are the corresponding electronic wave functions of the field-free ground state of each system in both real space and momentum space. A high degree of delocalization of the electronic ground state leads to a small width of the momentum space distribution, i.e. small velocity of spreading of the electronic wave packet during propagation in the continuum.

takes about 15 fs for the wave packet to travel from the inner turning point to the outer one. Since we excite many vibrational modes (due to the large bandwidth of the XUV pulse) close to the dissociation threshold dephasing occurs very rapidly.

Note that the ultrashort XUV-pulse is only used to accommodate the very fast vibrational dynamics in the H_2^+ molecule. The experiment can be performed in a heavier molecule like Na_2 , Br_2 or similar with pump pulses of duration of the order of tens of femtoseconds. It is only necessary that the exciting pulse is much shorter than the vibrational period. To illustrate this, Fig. 3.19 also shows the wave packet dynamics in Na_2^+ , created by the action of a 25 fs laser pulse at a wavelength of 620 nm. In this case, an almost classical oscillatory behavior is obtained due to the smaller bandwidth of the exciting laser pulse.

To calculate the transient harmonic emission of a sample of H_2 molecules irradiated by the driver pulse after pre-ionization by the pump pulse, the probability distribution function $|\Phi(d, t)|^2$ is multiplied by the harmonic yield $H(d)$ shown in Fig. 3.17. The result is plotted as $\tilde{H}(t)$ in Fig. 3.20. As can be seen, the integrated harmonic signal (H39-H51) shows a very rapid initial increase. This is because the molecule expands from the very inefficient interatomic distance range $d < 2$ a.u. into the more efficient region with $d > 3$ a.u. (Fig. 3.17 and Fig. 3.19). Afterwards, the signal oscillates as a consequence of the molecular vibrational wave packet motion.

In a recent publication by Baker et al. [170] a kind of inversion of this problem was demonstrated. Not the effects of molecular dynamics on high-harmonics is investigated

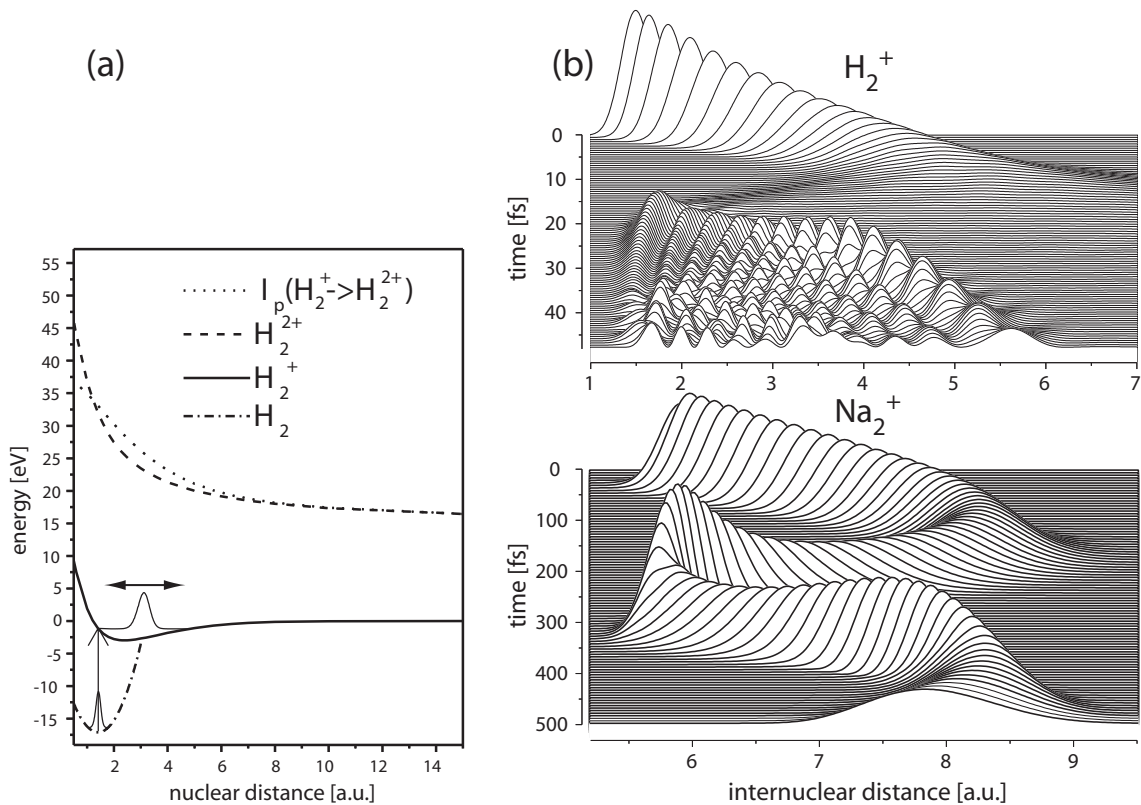


Figure 3.19: (a) Potential energy curve for the model H_2^+ system on which the molecular wave packet is created by ionization of the vibrational ground state of the neutral H_2 molecule (dash-dotted line). The potential energy curve of the H_2^{2+} (dashed line) is the Coulomb repulsion between the naked nuclei. The ionization potential of H_2^+ is shown as dotted line. (b) Vibrational molecular wave packet evolution in our model H_2^+ (top graph) after ultrafast ionization of the neutral H_2 molecule. Since many vibrational levels are excited close to the dissociation threshold, dephasing occurs on a very short time scale. The wave packet dynamics in Na_2^+ is shown below for comparison.

but the inverse effect. By careful analysis of the chirp of high-harmonic output the nuclear dynamics of the H_2^+ molecule was probed with a time resolution of 100 attoseconds.

Summary

Given the results on the design of optimum initial electronic states it is now clear that molecular systems are media which allow more efficient high-harmonic generation than atomic targets [171]. Two promising and new ways to enhance high-harmonic generation were pointed out: First of all, controlling the ground state wave function of the electron to ensure less spreading during continuum propagation and, second, variable choice of the ionization potential to allow perfect matching to the desired soft x-ray frequency range.

Taking all these results into account, it can be stated that using molecules for high-harmonic generation is beneficial to the optimization and control of any of the steps in the three step model, i.e. ionization, propagation and recombination. It should be pointed out that these calculations and experiments were restricted to simplest diatomic molecules.

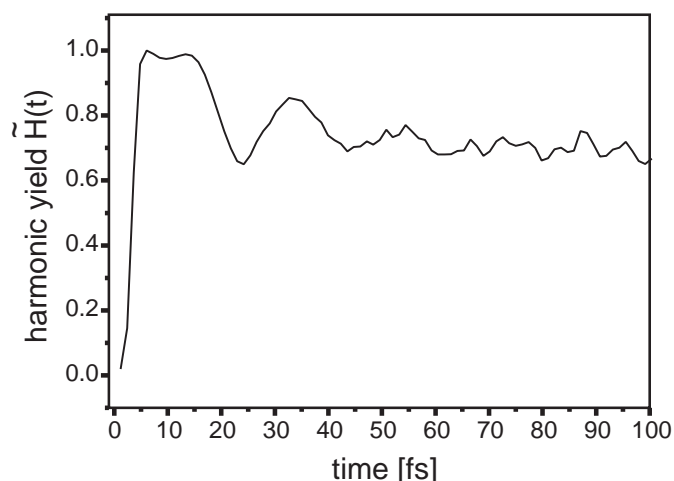


Figure 3.20: Integrated harmonic signal (H39-H51) in our model H_2^+ generated by the second (driver) pulse in a pump-drive scheme. Oscillations are due to molecular vibration (see Fig. 3.19 top graph) after ionization by the first (pump) pulse. A very rapid initial increase of the HHG yield is predicted.

Employing larger scale compounds like organic strings or cyclic-shaped molecules for high-harmonic generation should result in yet higher enhancements after suitable preparation by a controlling laser pulse. Thus, both experimental and theoretical investigations into the direction of molecular high-harmonic generation seem to bear great potential for table-top high-power ultrashort coherent soft-x-ray production.

3.5.3 Outlook: Pulse Shaping

Different methods to optimize the process of high harmonic generation were discussed in this chapter. Up to this point, enhancement of the signal by macroscopic effects like phase-matching were investigated and results in higher densities media like in water microdroplets were presented. To improve the single-atom response well prepared atomic systems in excited states or aligned molecules at fixed internuclear distances are proposed for future experiments. Harmonics will be emitted by electrons that recombine with the parent ion at enhanced probabilities in these systems. At this stage constructive and destructive interference of different quantum paths of the electronic wave function will play a crucial role. Before this step, during propagation, the electron dynamics will be mainly governed by the electric field of the driving pulse. By application of the pulse-shaping techniques presented in Chapter 1 the temporal evolution of the electric field can be manipulated. This will have its influence on the electronic motion during HHG. Specially engineered fields are able to enhance the conversion efficiency as will be shown in the next chapter. These tailored laser pulses will also have their effect on the propagation of the harmonics as they change the refractive index of the medium by a modified plasma-buildup. The results presented in the next chapter suggest that these propagation effects play a dominant role.

3.6 Competitive Sources of Ultrashort EUV and X-Ray Radiation

At the moment there exists no method besides high-harmonic generation that can generate pulses as short as a few hundreds of attoseconds. However, many applications depend on high photon count rates and are not dependent on short pulse durations. Large scale facilities like free electron lasers will unite high photon counts with short pulse durations but they are also VERY expensive to build and to maintain and only a limited number of experiments can be performed at the same time. X-rays have a wide range of applications from holographic imaging of single molecules [172] to the analysis of Beethoven's hair [173]. This section gives a short overview of alternative x-ray sources without any claim of completeness.

Laser-Plasma X-ray Sources

A short pulse of x-ray radiation is emitted after the generation of hot plasma on a solid target (e.g. copper wires) by a strong femtosecond pulse [174]. Their energy ranges between 1 – 10 keV and is emitted isotropically into 2π . Part of the radiation can be collected by a toroidal mirror and pulses down to 100 fs are obtainable [175]. These high energetic incoherent x-rays are ideally suited for time-resolved diffraction experiments [175] or EUV lithography to pattern fast microchips of the next generation.

Table-top X-ray Lasers

X-ray lasers (XRLs) are based on the principle of amplified spontaneous emission (ASE) in extended plasma columns with wavelengths in the range of 50 to 4 nm [176, 177]. Due to limited available optics in this wavelength range they usually have no cavities and work as single-pass amplifiers. XRLs exhibit very high brightness which is of great advantage for imaging small structures [178]. High harmonics can be used to seed the plasma amplifier and x-rays of high quality can be obtained [179].

The process of HHG itself can also be described as an X-ray-Laser. The group of T. Hänsch even designed a cavity version of HHG (XUV-laser [180]). A xenon jet is used as “amplifier” for the generated XUV-radiation in a high finesse cavity. Two Brewster angled sapphire windows, that provide low transmission loss for the resonator mode of the fundamental laser, act as beamsplitter for the collinearly generated XUV radiation. This setup allows efficient HHG up to high repetition rates and can be used to transfer the technique of optical frequency combs (see Section 1.6) into the XUV.

Free Electron Lasers (FEL)

Future applications in structural biology anticipate the need for pulses with much shorter duration (femtoseconds) and much higher energy (millijoules) than those delivered by conventional synchrotrons. These pulses can be provided by free electron lasers (FELs) like the planned x-ray FEL (XFEL [181]).

The optical amplification is achieved in an undulator, fed with high energy (relativistic) electrons from an electron accelerator. In the undulator electrons will emit high energy x-ray radiation during their oscillation and start to group to small “bunches”. The radiation

will amplify itself during the flight as it will be emitted coherently (see also the effect of “quasi-phasematching” in Section 3.4.2). Based on this principle X-ray free-electron lasers are expected to deliver enough x-ray photons in one shot to be able to even resolve the structure of single molecules (see [181] for expected specifications).

The FEL will start lasing on its own, based on the principle of self-amplified spontaneous emission (SASE) [182]. This generally results in chaotic shot-to-shot fluctuations with limited temporal coherence and leads to synchronization problems for external experiments using fs-pulses for pump-probe studies. A solution to these problems and an extension of basic FELs is the use of a seed laser. The method of high-gain harmonic generation (HG HG [183]) uses a seed laser to impose a small energy modulation on the electron beam that can be transferred into a density modulation. The “microbunched” electrons can afterwards efficiently emit the n -th harmonic of the seed laser field. In 2003 Yu et al. could demonstrate the first HG HG for the ultraviolet [184].

Chapter 4

Adaptive Optimization of High Harmonics

The idea of using shaped driver fields to influence or even control the process of high harmonic generation will now be tested. The electric field that interacts with the conversion medium will determine how the different electron quantum-paths will interfere (Section 3.1.2) and can influence the chirp of harmonics [93, 94]. It also influences the amount of ionization and changes phase-matching conditions by generating different amounts of free electrons. By propagation in hollow fibers with long interaction length these effects become even more pronounced. In these waveguides the spatial intensity distribution of the traveling mode will be an additional parameter.

The control will be performed using the spectral structure of the generated harmonics as feedback. The evolutionary algorithm defined in Chapter 1 will be used to find optimal pulse shapes to enhance and control HHG.

The first control of high-harmonic generation was demonstrated in 2000 by Bartels et al. [93]. A significant enhancement of high harmonic output could be observed. The optimized laser pulse was not merely bandwidth-limited or linearly chirped and had to be found iteratively by the algorithm.

If it becomes possible to control the temporal profile of harmonics will this be a possible way to shape attosecond pulses? The direct transfer of pulse shaping techniques developed in the optical wavelength range to the soft x-ray regime is not feasible. Existing devices either require spectral dispersion (e.g. liquid-crystal or acousto-optical spatial light modulators, deformable mirrors) or extensive passage through material (acousto-optic programmable dispersive filter, Dazzler [185]) which precludes their applicability in the soft x-ray spectral range due to small diffraction efficiencies for spectral dispersion and high absorption. Therefore it would be advantageous to directly generate a shaped soft x-ray pulse by shaping the fundamental laser pulse prior to the conversion process than after its production.

In the following it will be shown that this is indeed possible! The soft x-ray spectrum can be manipulated in a very general sense, far beyond earlier results on the control of particular spectral properties such as conversion efficiency and line width [93, 186] or the blueshift of harmonics [187]. This is the topic of Section 4.2 where it is shown that it is

possible to selectively generate certain extended parts of the HHG spectrum while keeping other harmonic orders at low intensity. Isolated harmonics at different wavelengths can be selectively generated with high contrast ratio. It is feasible to suppress single harmonic orders while neighboring ones are generated, which has not been observed before.

The control of high-harmonic generation (HHG) in hollow fibers using adaptive pulse shaping techniques is the topic of this chapter. Temporal-only shaping experiments with a deformable mirror are presented in Section 4.2 that includes both the free focusing and the waveguide geometry. The shaping capabilities of the two-dimensional LCD-based spatial light modulator (SLM) are demonstrated by the excitation of specific fiber modes inside a hollow fiber with a helium-neon laser in Section 4.3. Spatially shaped ultrashort pulses are used to generate phase-matched high-harmonic radiation in a fiber. By controlling the mode structure, the spatial and spectral properties of the generated harmonics can be manipulated.

4.1 Optimization Setup

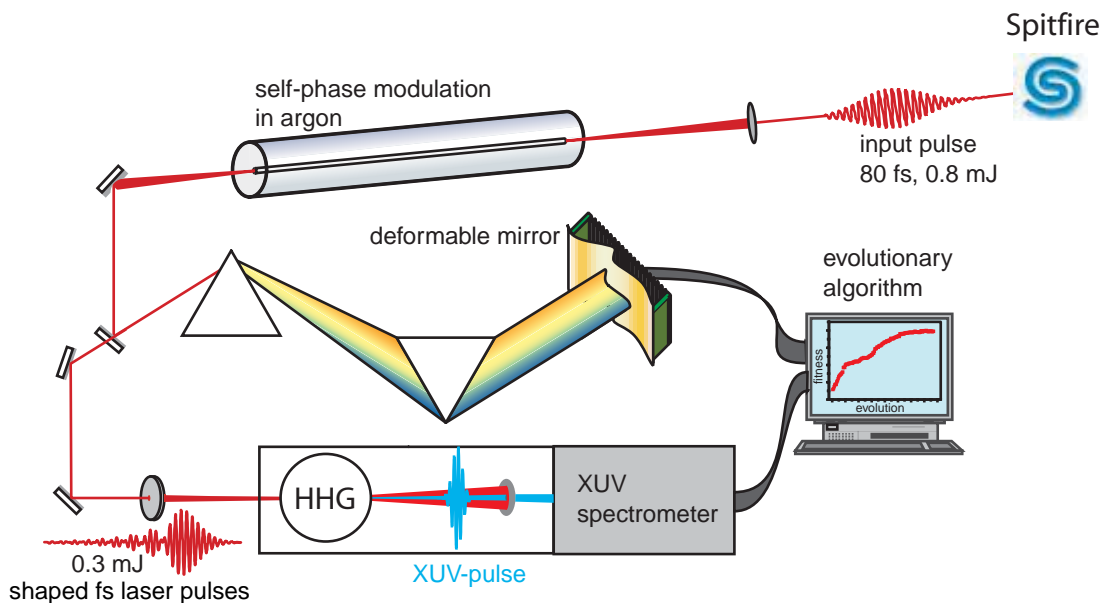


Figure 4.1: Experimental pulse-shaping setup used for adaptive femtosecond laser-pulse compression. The pulses are sent through an argon gas filled hollow core fiber in order to broaden the spectrum. Afterwards, they are spectrally shaped in a prism compressor that has an addressable deformable mirror in its Fourier-plane. These modulated pulses will then interact with the high-harmonic conversion medium placed inside a vacuum system. The generated radiation is analyzed by a XUV-spectrometer and evaluated by an evolutionary algorithm.

For the optimization experiments presented in this chapter the regeneratively amplified Ti:sapphire laser system of Spectra Physics is used again. Its output pulses are spectrally broadened by self-phase modulation in a gas-filled hollow fiber similar to the setup of

Section 2.1. The fiber is about 0.6 m long with an inner diameter of 250 μm . It is filled with argon at a pressure of about 1 bar.

The laser pulse then passes a pulse shaping setup based on the design described in Section 1.5.1. Basically, it consists of a prism compressor, in which the retroreflecting mirror is exchanged by a deformable membrane mirror. Applying voltages to the nineteen linearly arranged control electrodes placed behind the membrane results in slight deformations of the mirror surface. The spatial modulations translate into spectral phase modulations because the impinging laser pulses are spectrally dispersed. A computer is used to control the high voltage levels. Due to the limited number of degrees of freedom of the deformable mirror (19 controllable actuators) the evolutionary algorithm can converge much faster compared to the case of the two-dimensional SLM-device of Chapter 2. The population size was therefore increased to 50.

The prism compressor of the pulse shaper is used to shorten the pulses to about 20 fs duration for a flat phase on the deformable mirror. The laser pulses have an energy of about 0.3 mJ when they are focused into the vacuum system for high-harmonic generation. In the following section high harmonics will be generated and optimized in the gas-jet setup (already described in Section 3.4.1). In Section 4.2.2 the hollow-fiber setup will be used.

After interaction with the generation medium the 800 nm fundamental laser pulse and the lower-order harmonics are blocked by a 0.3 μm thick aluminum filter. The transmitted soft-x-ray radiation is characterized with an extreme-ultraviolet (XUV) CCD-camera-based spectrometer (grazing-incidence monochromator (Jobin-Yvon, LHT30) with back-illuminated CCD (Princeton Instruments Digital CCD System, SX-400/TE)). The distance of the high-harmonic source and the spectrometer slit is about one meter and the beam divergence ranges from about 3 to 12 mrad. The recorded spectra are evaluated by a fitness function, and an evolutionary algorithm is applied to optimize the spectral shape of the generated radiation.

The closed-loop optimization iteratively shapes the laser pulse with the deformable mirror and the obtained spectrum is measured with the CCD camera. The fitness value for each shaped laser pulse is derived from the HHG spectrum by integration of the spectral intensity in different regions. A population size of 50 is used for the evolutionary algorithm throughout this chapter.

4.2 Controlling the Spectral Shape of High Harmonics

4.2.1 Gas-Jet Setup

The description of the gas-jet setup is already given in Section 3.4.1. The harmonic spectrum for generation in the gas-jet that was shown in Chapter 2 (Fig. 3.6b) can be regarded as reference spectrum and was obtained for a flat surface of the deformable mirror. The prism compressor was adjusted to yield the highest harmonic output. Here a 0.8 μm aluminum filter was used to block the fundamental beam.

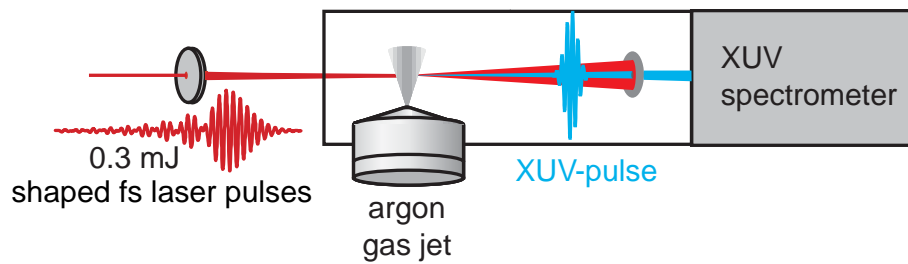


Figure 4.2: Setup for the experiments on control of high-harmonic generation produced in the gas jet. Temporally shaped laser pulses are focused into a gas jet produced by a pulsed valve operating at the repetition rate of 1 kHz.

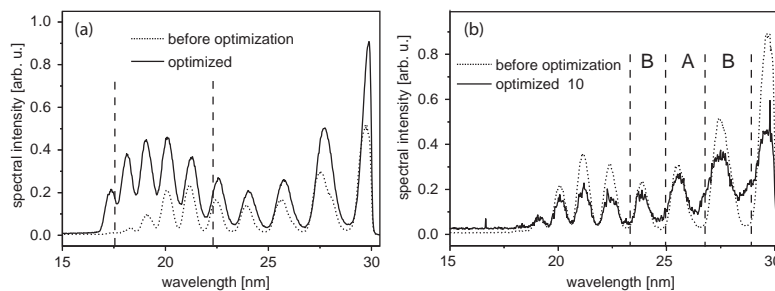


Figure 4.3: (a) Optimization of the cut-off position of high-harmonic generation. The evolutionary algorithm was able to shift the cut-off position by several harmonic orders. The emission of even higher orders is prevented by absorption of the Al-filter. (b) Optimization of an isolated harmonic (region A) while neighboring harmonics are suppressed (region B). No significant enhancement over the neighborhood can be observed, in contrast to the waveguide geometry (next section). The overall signal strength decreased as a consequence of not being included in the fitness function.

Cut-off Extension

In a first experiment it was tested if the cut-off of the high-harmonics could be extended to higher frequencies. This would be expected for a higher peak intensity of the laser pulses. The spectral phase of the laser pulses that is obtained during self-phase modulation inside the hollow fiber can not be completely compensated by the prism compressor alone. In a recent optimization experiment with the deformable mirror it was possible to increase the SHG signal of the laser pulses [188]. This can be taken as clear indication that the peak intensity of the pulses could be increased by compensation of the residual higher-order phase with the deformable mirror. Equivalent behavior is expected as result of the optimization of the high-harmonic cutoff.

The fitness was designed as the integrated yield within the spectral regions indicated by the dashed lines of Fig. 4.3a. As can be seen in Fig. 4.3a, the cut-off of the optimized spectrum could indeed be shifted by more than four harmonic orders. The overall harmonic intensity was increased at the same time. The emission of even higher orders is prevented by absorption of the Al-filter. It is therefore possible that the cutoff was indeed shifted by a larger amount.

Similar results have already been obtained by several groups [125]. It was shown that

the position of the high-harmonic cut-off can be shifted with shaped laser pulses and the overall yield could be increased [189, 187]. It could be also shown that the spectral position of the harmonics are tunable [187]. This is explained by an increasing amount of blue-shift due to enhanced ionization of the medium.

Isolation of a Single Harmonic

In a next step the fitness was defined to isolate the enhancement of a single plateau-harmonic near the cut-off. According to the spectral regions defined in Fig. 4.3b the fitness $F = A/(A + B)$ was used with A and B denoting the integrated yield in corresponding spectral regions. This fitness was also designed to suppress the neighboring harmonics. The optimized result (Fig. 4.3b) shows no enhancement compared to the reference signal (similar results have also been found in [187]). In fact, the overall signal decreased as it was not included in the fitness. In the next section similar optimizations are performed with the hollow-fiber setup with much more promising results.

4.2.2 Hollow-Fiber Setup

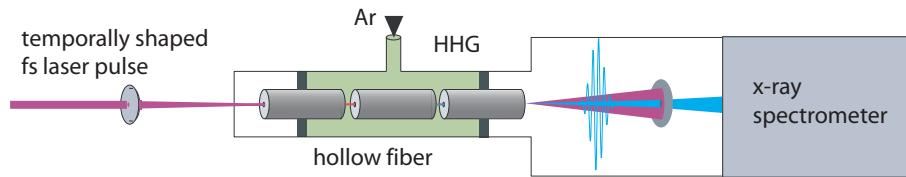


Figure 4.4: Setup for the experiments on control of high-harmonic generation produced in a gas-filled hollow fiber.

Now, the shaping techniques are applied using the hollow-fiber designed that is described in Section 3.4.2. In comparison to the gas-jet setup now phase matching effects will narrow the range for harmonic generation and increase their efficiency.

The fiber is filled with argon of a pressure of about 100 mbar. Here high-harmonic generation takes place. The visible laser pulse and the lower order harmonics are blocked by a $0.3 \mu\text{m}$ thick aluminum filter [190]. The laser intensity in the hollow fiber is $2 \times 10^{14} \text{ W/cm}^2$. For the estimated peak intensity and argon as the nonlinear medium ($I_p = 15.8 \text{ eV}$) a cut-off near the 29th order is expected, which is in agreement with the experimental findings.

First of all, selectivity of coherent soft x-ray radiation over a wide spectral range is demonstrated. The spectrum is divided into two parts containing three to four harmonic orders each (see region denoted as I, II in Fig. 4.5b). The fitness function was defined as the difference of integrated spectral yields in parts (I) and (II). At the end of the optimization the harmonic signal in one part could be suppressed while the other part was maximized as shown in Fig. 4.5a-c. While selective generation of the lower-order part of the spectrum can be readily understood by considering reduced peak intensity in a chirped generating pulse, it is not clear yet what causes the enhancement of higher orders while simultaneously suppressing lower order harmonics almost completely.

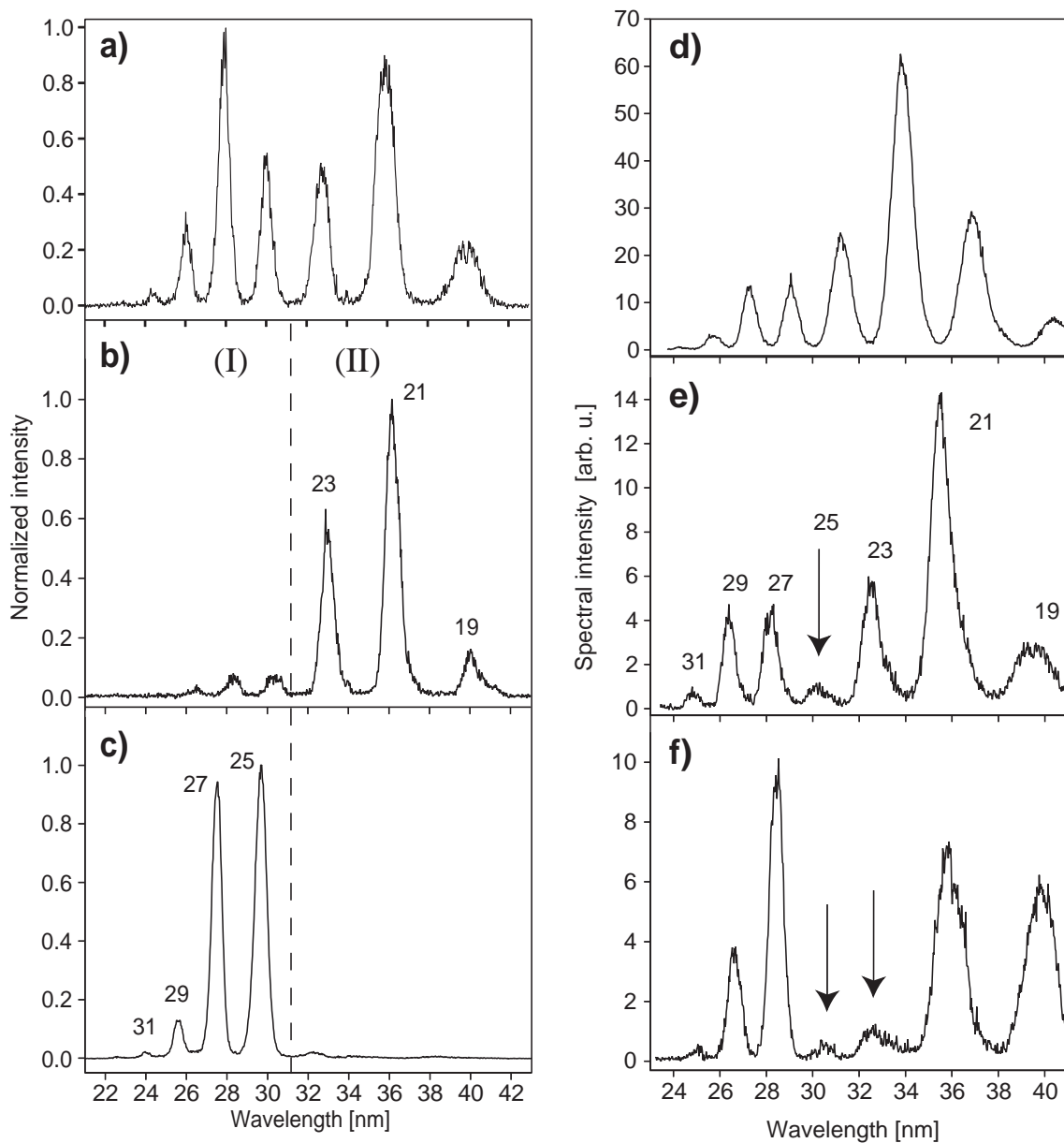


Figure 4.5: (a-c) Selective control of high-harmonic generation. An extended frequency region is selected and optimized with respect to the remainder of the spectrum using an adaptive closed-loop optimization algorithm. (a) Reference spectrum obtained with an unmodulated laser pulse. (b) Optimization of the low-frequency spectral part while simultaneously reducing the high-frequency part and vice versa. (c) These results demonstrate that it is possible to solve the problem of harmonic selection for attosecond pulse generation without employing additional optical components such as multilayer mirrors. (d-f) Suppression of harmonics while generating adjacent ones at about one order of magnitude higher efficiency. (d) Typical harmonic emission in the plateau region, (e) one suppressed harmonic order, (f) two suppressed harmonic orders. The high degree of controllability of soft-X-ray spectral shape over a large range of photon energies (≈ 10 eV) implies major modifications of the corresponding temporal shape on a sub-femtosecond time scale.

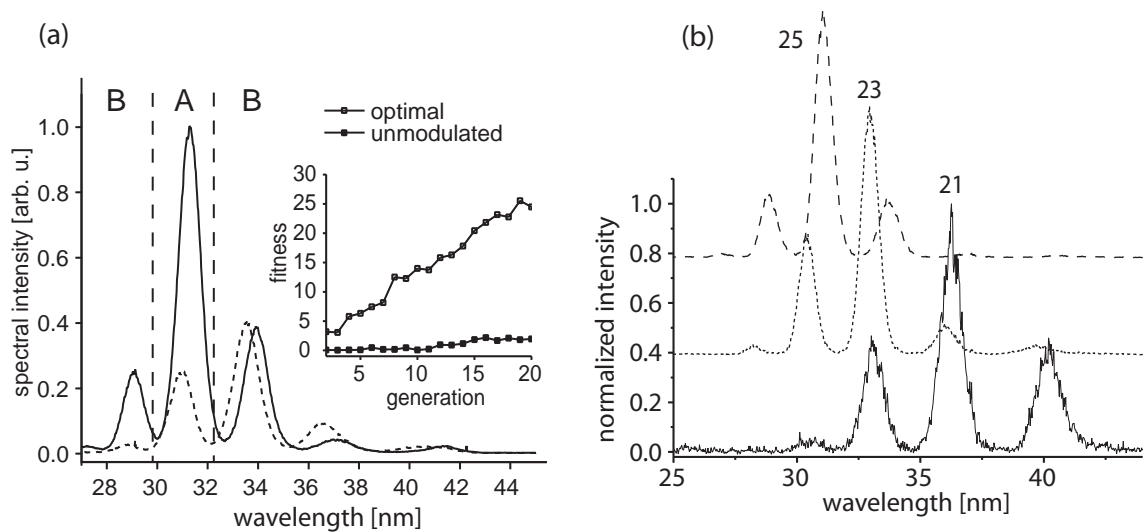


Figure 4.6: (a) Optimization of a single harmonic. The graph shows results for the optimization of the 25th harmonic both absolute and relative to the neighboring orders (solid line: optimized result, dashed line: initial spectrum (unmodulated laser pulse)). The fitness function to be maximized by the evolutionary algorithm is defined as A^2/B . During the run of the optimization experiment the fitness increases (see inset). The soft x-ray spectra obtained for unmodulated (filled squares) and optimal (open squares) laser pulses are presented. (b) Generation of a narrow-band harmonic spectrum for different selected single harmonics. The selectivity demonstrated in our results displays a high contrast ratio. The tunable coherent soft x-ray radiation is useful for femtosecond time-resolved photoelectron spectroscopy with high spectral resolution, preventing an increase in pulse duration that occurs when using monochromators.

The level of control over the process of harmonic generation becomes yet more evident in spectra where one or two harmonics in the plateau region are suppressed (Fig. 4.5d-f). Fig. 4.5d shows a typical phase-matched harmonic spectrum. Nearly equally intense harmonics were observed implying that the displayed range lies in the plateau. Fig. 4.5e and f display the spectra after running the adaptive feedback loop with the goal to suppress one and two adjacent harmonics, respectively. The selected harmonic orders were “switched off” while neighboring peaks are nearly unaffected.

The selective generation of single harmonic orders at different frequencies while simultaneously keeping neighboring orders at low intensity was also successful. Fig. 4.6a shows an unprecedented contrast ratio between the desired harmonic and the remaining ones. Only relatively weak direct neighbors are present while emission at other harmonic orders is negligibly small. To define the fitness function for this optimization, the spectrally integrated intensity of the desired harmonic was divided by the integrated spectrum of the other harmonic orders to favor the relative yield of the selected harmonic. The number of photons per XUV-pulse of the isolated peak was estimated to be about 10^6 corresponding to a conversion efficiency of $\eta \approx 10^{-8}$.

To shed light onto the physical processes responsible for the observed spectral modifications the one-dimensional Schrödinger equation was numerically integrated in an arbitrarily shaped laser field. The HHG spectra were obtained by Fourier transformation of

the time-dependent expectation value of the electric dipole acceleration like explained in Section 3.1.2 [168]. This simple model only describes the single atom response without considering propagation effects. It was implemented into the same evolutionary algorithm as the one used in the experiment. The simulation was able to achieve both enhancement and suppression of the selected harmonic order, however, to a much lower extent as observed in the experiment [127, 191].

In comparison to the results of the gas-jet optimizations in the previous section these findings point to the importance of considering both the single-atom response and additional spatial effects determined by the waveguide geometry in order to efficiently control HHG. In contrast to a gas jet where any spatial modification of the laser focus is only present over a very small distance, the capillary waveguide allows to sustain this change over an extended interaction length and influences the propagation of the fundamental and harmonic radiation through the waveguide modes. In agreement with previous work [94], the simulation shows that the temporal profiles of fundamental pulse shapes are only slightly different for harmonic spectra that differ substantially.

A direct comparison of the pulse shapes found as results in the simulations with the experimental results was not feasible because only the pulse shape on the entrance of the hollow fiber could be measured. Before and during the process of HHG the laser pulse experiences substantial spatial and temporal reshaping making a quantitative comparison with theoretical results meaningless.

The selective generation of a part of the harmonic spectrum is a possible solution to single out the spectral region, where the harmonics have a fixed relative phase resulting in a train of attosecond pulses. According to recent work [97], selecting a suitable region of contributing harmonic frequencies allows to control the temporal shape of the attosecond pulse produced.

The demonstrated pulse shaping technique enables the selection of a range of harmonics where the relative phases support the shortest attosecond pulse possible. In addition, the possibility to shift the range of harmonics now provides a way to tune the wavelength of the resulting attosecond pulses or pulse trains.

Narrow-band HHG spectra (major contribution from just one harmonic) now allow for time-resolved spectroscopy in the soft x-ray region. Improved experimental results are expected for extended capabilities of the driving laser (e.g. stabilized carrier envelope phase [192]) or the pulse shaping device (higher number of degrees of freedom).

Full control over the shape of the soft x-ray spectrum has a major impact on energy-resolved spectroscopy and paves the way to the control of electron dynamics.

Is comprehensive control of the coherent HHG spectrum possible that allows engineering of the spectral properties and possibly the temporal evolution of the emerging sub-femtosecond pulses or pulse trains? Suppressing one or two harmonics as shown in Figs. 4.5e and f effectively produces a bimodal spectral distribution, with a mode spacing of approximately seven times the fundamental frequency. This results in a sub-half-cycle beating in the temporal response with a period of about one seventh of the optical period. This example demonstrates the potential of extending pulse shaping into the attosecond regime.

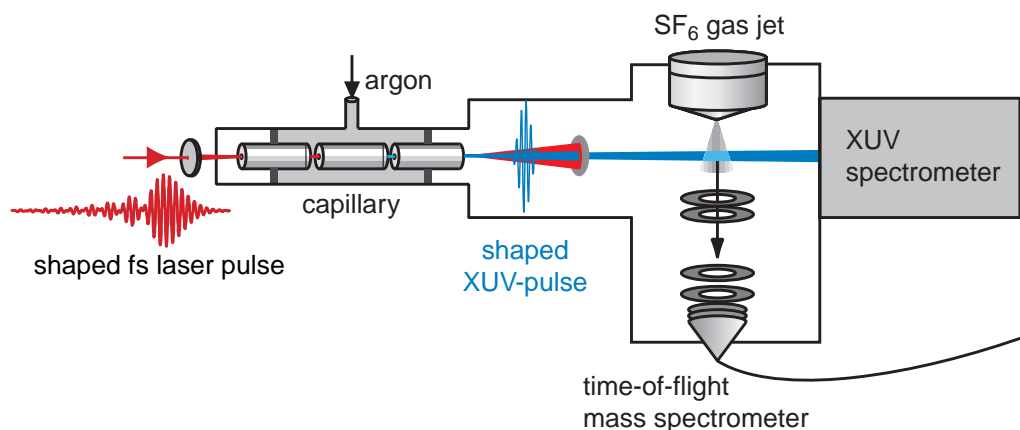


Figure 4.7: Setup for the experiments on adaptive control of photochemistry by high-harmonic spectral engineering. The high-harmonic radiation output from the capillary is used to induce dissociative ionization in SF_6 gas. The fragments are detected with a linear time-of-flight mass spectrometer. The spectral shape of the soft-x-ray pulses can be measured in parallel, since only a small fraction of the harmonic light is absorbed by the SF_6 gas.

Optimization of the Photodissociation of SF_6

Finally, a short experimental application of the adaptive XUV-spectra was designed.

The available vacuum-setup for high-harmonic generation only allowed to focus the high-harmonic radiation efficiently. In a test-setup a focal-spot inside a gas-jet was generated by usage of two gold-coated mirrors (a plane mirror for deflection by 90 degrees and a concave mirror for focusing (see [193] for geometry of vacuum setup)), but only few percent of the initial XUV-radiation reached the target [123].

Using SF_6 (sulfur hexafluoride) as target gas only very low ion count rates could be detected making this setup unattractive for optimizations. Exchange of the low efficient gold-coated optics by high efficient multilayer-mirrors [194] was not chosen as an option because of limited availability of multilayer optics in the required wavelength range of about 25 to 35 nm. The most common MoSi multilayer mirrors are mainly designed for high reflectivities at 13.6 nm and have generally only small bandwidths of few nanometers [122].

However, it was still possible to design an experiment to influence the fragmentation behaviour of SF_6 with spectrally shaped high-harmonics (see also [195] or [191]) by placing the interaction region with the SF_6 gas jet “directly” after the exit of the HHG-fiber (in a distance of about 10 cm to the exit of the fiber). SF_6 has an ionization potential of 15.32 eV [196] and is a well-studied system for photofragmentation. Different positively charged ions are generated during fragmentation processes as explained by dissociative photoionization [197–200].

Different positively charged ionic fragments are easily detected and distinguished in a linear time-of-flight (TOF) mass spectrometer (home-built TOF of the Wiley-McLaren type was used [201, 202]). The mass spectrometer is equipped with a microsphere-plate detector (MSP) that is able to work up to pressures of 10^{-5} mbar.

In the context of quantum control with soft-x-ray/XUV (extreme ultraviolet) light, the re-

cent theoretical study by Palacios et al. [203] should be pointed out, who examined control of dissociative ionization in a H_2 molecule. They reported a significant dependence of the ionization mechanism on the pulse duration even for very moderately intense XUV pulse intensities.

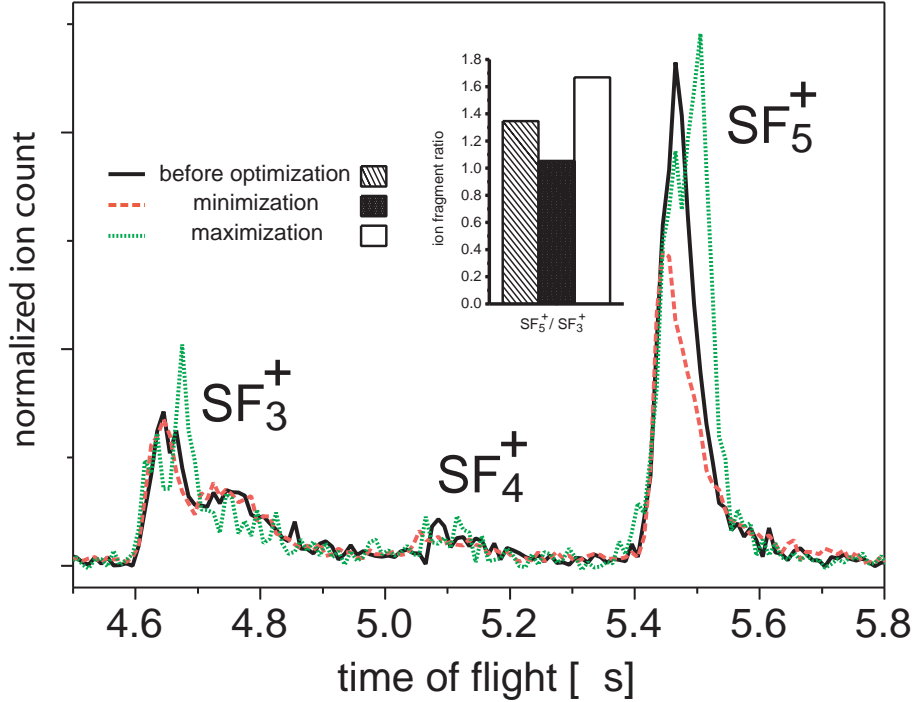


Figure 4.8: Time-of-flight mass spectra for the interaction of SF_6 with tailored high-harmonic radiation for the case of maximization and minimization of the SF_5^+ versus SF_3^+ branching ratio. The two mass-spectra are normalized to the integral ion yield of the SF_3^+ peak area to visualize the relative changes on the SF_5^+ peak. The changing fine structure of the peaks are indicative of differences in the fragmentation dynamics.

Choosing a pressure of 100 mbar argon inside the hollow-fiber, high harmonics were generated and interacted with the jet of SF_6 molecules (backing pressure of 2 bar). High ion count rates from SF_1^+ to SF_5^+ could be detected [195]. Since the beam is only negligibly absorbed in the jet due to the low gas density, this setup is capable of recording the ionic mass spectra and the photon-energy spectra at the same time. This gives the opportunity to compare qualitative changes in the mass spectra, e.g. the changing branching ratios, directly to changes in the soft-x-ray spectra of the light.

The signal of the ion fragments vanished for a low pressure inside the fiber (no harmonics generated). To exclude a possible influence of the fundamental radiation, a $0.3 \mu\text{m}$ aluminum filter was placed between the fiber exit and the interaction region. The integrated ion yields for each fragmentation process could be isolated using a boxcar integrator. Following fitness function was designed for the control experiment:

$$F = \frac{\text{yield}(\text{SF}_5^+)}{\text{yield}(\text{SF}_3^+)} \quad (4.1)$$

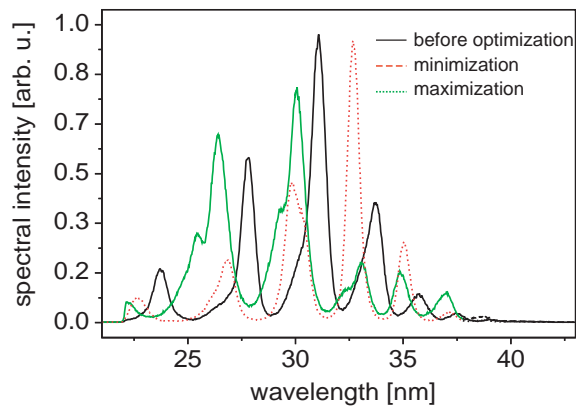


Figure 4.9: Soft-x-ray spectra of shaped harmonic emission to optimize photofragmentation of SF_6 . Optimal harmonic spectra are shown that maximize (dotted lines) or minimize (dashed lines) the two branching ratios SF_5^+ versus SF_3^+ . The unmodulated reference harmonic spectrum before optimization is also given for comparison.

Fig. 4.8 shows the result of a maximization and subsequent minimization of the fitness F . The relative product yields could be maximized and minimized with respect to the reference yield obtained for the unmodulated spectrum prior to optimization. The soft-x-ray spectra recorded for the case of maximization and minimization of the ion yield, along with the spectrum before optimization are presented in Fig. 4.9. Due to the combined effects of absorption by the argon gas used for HHG and the aluminum filter the recorded spectra contain the full spectral intensity information about the light used in the experiment. The spectrum before optimization (unmodulated spectrum) is typical for phase-matched harmonic generation in a capillary. For the maximization case (SF_5^+ versus SF_3^+), a pronounced shift of the overall spectral mean towards lower frequencies is visible. In contrast, the minimization leads to a spectral distribution the spectral mean of which is shifted towards higher soft-x-ray photon energies. Additionally, both optimized spectra exhibit the same amount of (ionization-induced) blueshift of the harmonic peaks with respect to the unmodulated spectrum. The substructure of some harmonic peaks is also modified in the spectra that correspond to different optimization goals.

The shifting of the peaks in the mass spectra of Fig. 4.8 could be caused by a difference in fragmentation dynamics resulting in different fragment energies. In fact, changes in the distribution of the fragment kinetic energy with XUV pulse duration were observed in the recent theoretical study by Palacios et al. [203] for the simple case of H_2 . In dissociative ionization, the fragments are produced at different kinetic energies, depending on the particular high-lying excited electronic states populated prior to fragmentation. Not only the energy can be different but there is also an angular dependence of the ionization process with respect to the polarization direction of the linearly polarized high-harmonic light. It is known from earlier studies [199, 200] that a pronounced anisotropy of the fragmentation process of SF_6 prevails for exciting photon energies in the range of interest here. A comparable optimization was also performed using $F = \text{yield}(\text{SF}_4^+)/\text{yield}(\text{SF}_2^+)$ as fitness with similar results (see [195]).

This study can be understood as a demonstration of the versatility and stability of the

adaptive coherent soft-x-ray source for this type of experiments. Even though the experimental findings are hard to interpret due to a poorly defined interaction volume (interaction of SF₆ gas jet with unfocused high-harmonics) and lack of angular resolved data, the optimization setup was able to enhance different experimental results under reproducible conditions. In future experiments soft x-rays can be particularly useful in this context to obtain selectivity in chemical reactions as they provide a means for site-specific electronic excitation in molecules [204].

4.3 Spatial Control of High-Harmonic Generation in Hollow Fibers

So far, only the pressure inside the gas-filled hollow fiber was adjusted to select the spectral region where phase-matching applies [128], but one can see from Eq. (3.23) that the excited fiber mode(s) are also of importance. The excitation of different fiber modes changes the phase velocity of the driving pulse and leads to different intensity distributions inside the fiber. The excitation of more than one mode at a time favors harmonics of different spectral regions (for each fiber mode u_{nm} a different frequency satisfies the phase-matching condition in Eq. (3.9)). Furthermore the phase relationship between different modes will possibly influence the phase structure of the harmonics generated under these circumstances. Which fiber modes are excited after the driving laser has been coupled into the fiber is determined by the spatial amplitude and phase profile of the driving laser pulse at the entrance of the fiber.

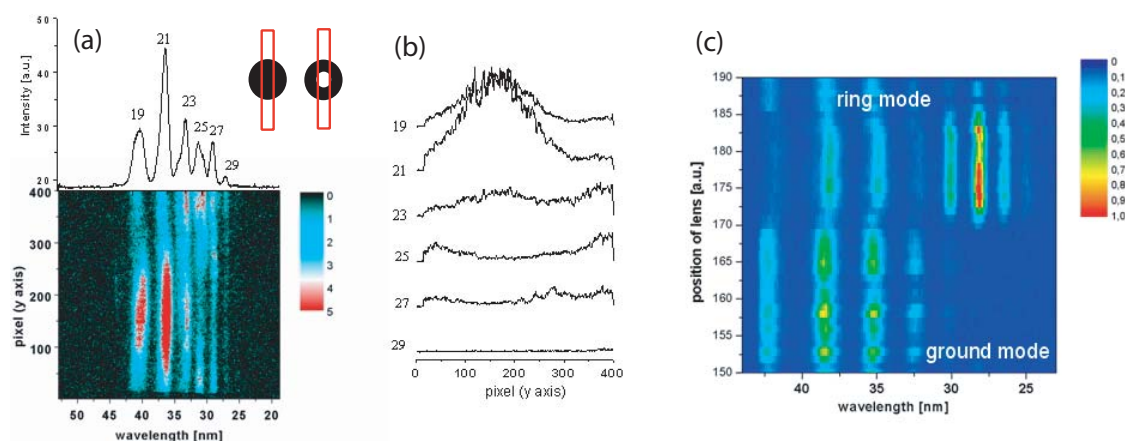


Figure 4.10: (a) Spatially resolved high-harmonic spectra (spatial distribution along entrance slit of the spectrometer). Different spatial intensity profiles are observed for different harmonics. H19 to H23 display Gaussian-shaped profile while H25 and H27 have intensity distributions explainable by a ring-mode profile (b). (c) shows the influence of imperfect fiber-coupling for HHG. Misalignment of the setup results in excitation of higher-order fiber modes leading to modifications of the spectral shape of high-harmonics.

First indications of an influence of different fiber modes on the spatial profile of high-harmonics were obtained during the temporal optimization experiments of the previous

section. During those experiments spatially resolved snapshots of high-harmonics with the two-dimensional chip of the x-ray detector were taken (Fig. 4.10). Different divergence behaviour for different high harmonic orders was observed that manifests itself in different spatial intensity distributions along the entrance slit of the x-ray spectrometer. This spatial distribution is imaged spectrally resolved onto the two-dimensional CCD-chip of the detector. As can be seen in Fig. 4.10 harmonics H25 and H27 have a non-Gaussian intensity distribution. It is possible that these harmonics have been generated by a ring-like fiber mode (low intensity in center, high intensity in outer regions), while the others are generated by the Gaussian-shaped ground mode.

The deformable mirror predominantly shapes the temporal profile of laser pulses (horizontal axis) and has intentionally limited ability to spatially deform the pulse profile (vertical axis (see Section 1.5.1.1)). However, it will be able to slightly deflect the laser pulses and therefore can change the coupling into the hollow-fiber.

If imperfect fiber-coupling has influence on the generation of high-harmonics was tested manually by a slow scan of the horizontal position of the focusing lens (Fig. 4.10c). This scan changes the position of the laser focus with respect to the fiber entrance and slightly changes the coupling-angle. This will lead to imperfect coupling conditions of the laser into the fiber and excitation of higher order fiber modes is expected. The scan reveals two different regimes for different positions of the lens with different spectral structure of high harmonics. This is an indication that excitation of higher order fiber modes can indeed influence high-harmonic generation.

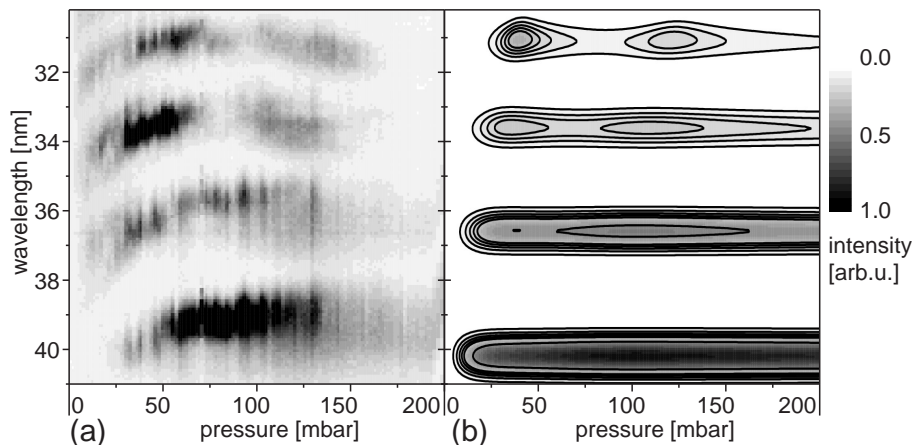


Figure 4.11: Pressure dependence of HHG in hollow fibers for excitation of two fiber modes. (a): experiment, (b) simulation. Emission at lower pressures is caused by the EH_{11} mode, at higher pressures by the EH_{12} mode. The simulation provides additional confidence by reproducing the shift of the intensity maximum for each mode to higher pressures with decreasing wavelength.

Phase-matching in hollow fibers is dependent on the mode of propagation (u_{nm} in Eq. (3.23)). Therefore it is possible to phase-match different spectral regions for a fixed gas pressure if different modes are excited at the same time. Fig. 4.11a shows the pressure dependence of the high-harmonic output in the case of two excited fiber modes. The harmonics H23 and H25 are phase-matched at a pressure of 40 mbar and 120 mbar. A

simulation was carried out in order to evaluate the experimental result. Inserting the experimental parameters and assuming reasonable ionization yields on the order of a few percent [101], Fig. 4.11b is obtained, which shows good agreement with the experimental findings. In particular, the shift of the maximum yield to higher pressures with harmonic order is reproduced by the simulation.

Interestingly the spectrum at a pressure of about 75 mbar in Fig. 4.11a also has a spectral hole at the position of the 23rd harmonic. In comparison to the results of Fig. 4.5e, this is an indication that the ability to suppress harmonics may be also partly due to spatial shaping effects.

The PAL-SLM (see Chapter 2 and Appendix A) will be used in this section to spatially shape the laser pulses. It will be placed after the exit of the temporal shaping setup with the deformable mirror.

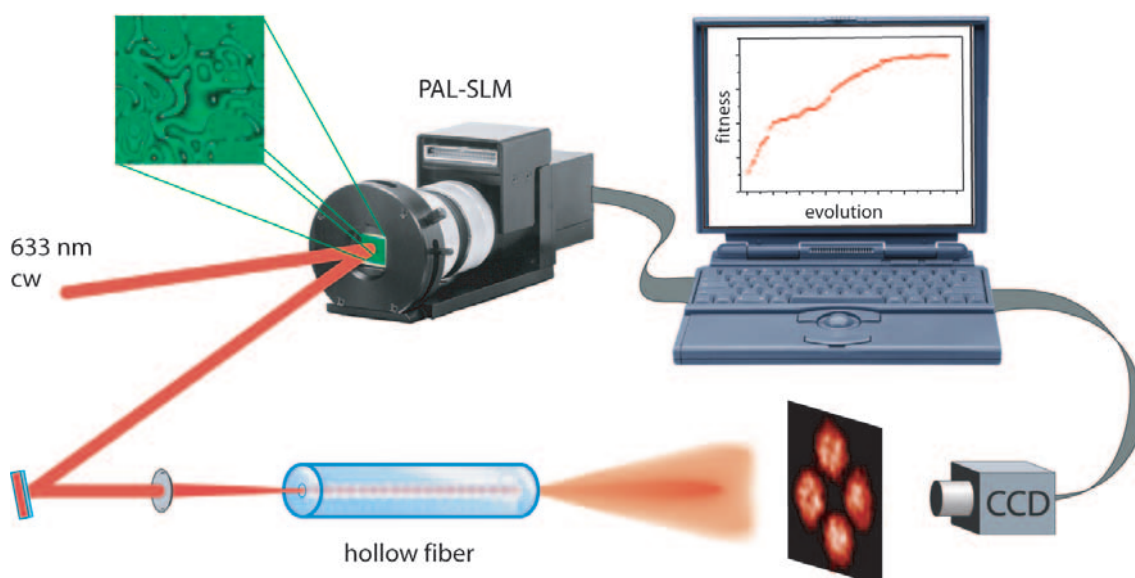


Figure 4.12: Setup used to test the shaping capabilities of the PAL-SLM. A spatially shaped laser beam is optimized to excite a distribution of fiber modes. The optimization goal was a predefined intensity distribution on a CCD camera.

Optimization of fiber modes

To test the shaping capabilities of the PAL-SLM the active area of the pulse shaper was homogeneously illuminated with a helium-neon laser (Fig. 4.12). The spatially shaped reflection was focused into a 10 cm long hollow fiber (140 μm inner diameter), equivalent to the fiber that is used for the optimization experiments of the high harmonics. The fiber output was recorded by a CCD camera and read out by a computer. This computer also controlled the phase modulation of the PAL-SLM so that the feedback-looped evolutionary algorithm could be applied. To be able to optimize the fiber output the fitness function was defined as the integral overlap between the picture on the CCD camera and a predefined bitmap mask which was used as the optimization goal. The higher the fitness, the higher is the correspondence of the fiber output with the bitmap mask.

The evolutionary algorithm starts with a fixed number of random phase patterns as a first generation. The phase patterns are represented by a square array of $n \times n$ pixel blocks (the pixels of the PAL-SLM are grouped together to limit the number of effective parameters to speed up the optimization process). Each pixel block represents a gene that is used by the algorithm to obtain the fittest phase pattern. As the active area of the PAL-SLM takes about 400 ms to change its phase front, the optimization process can take several hours to converge.

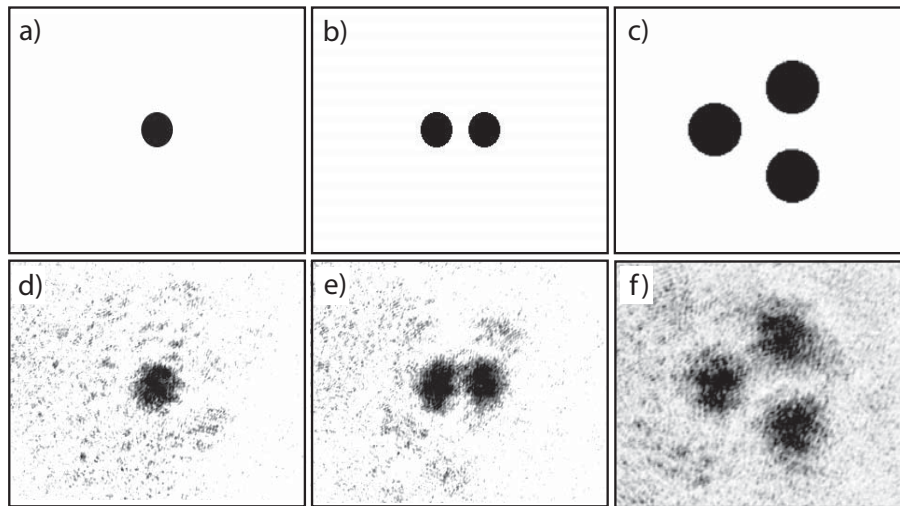


Figure 4.13: Three optimized fiber outputs next to their corresponding target masks (top row). From left to right: fundamental mode (a), (d); double mode (b), (e); triple mode (c), (f).

Prior to each optimization run, the coupling into the fiber was adjusted manually with a flat phase profile on the PAL-SLM until a complex superposition of fiber modes was achieved resulting in a rather complex intensity distribution on the CCD camera. This was used as the starting point for the optimization.

The first target masks represented the fundamental fiber mode (Fig. 4.13(a)), a double mode (Fig. 4.13(b)) and a triple mode (Fig. 4.13(c)) as a result of interfering lower-order modes. The corresponding optimized fiber outputs can be seen below the target masks (Fig. 4.13(d)-(f)). After the optimal phase profiles for different fiber modes have been found it is possible to switch between them without the need for additional optimization runs.

The optimization to a more complex EH_{12} ring mode is shown in Fig. 4.14. Next to the fiber output obtained for a flat phase profile of the PAL-SLM (Fig. 4.14(b)) there is an additional snapshot of an already slightly optimized result (Fig. 4.14(c)) where most of the parts of the ring structure (Fig. 4.14(c)) are already reproduced.

Under the assumption of an initially flat phase profile of the laser beam and a gaussian radial intensity distribution it can be estimated how the spatial pulse shaper affects the beam. Figure 4.15 shows the intensity (Fig. 4.15(a)) and phase distribution (Fig. 4.15(b)) at the fiber entrance (indicated by the circle) obtained by Fourier transforming the modulated spatial beam profile corresponding to the phase pattern that couples into the ring mode (fiber output of Fig. 4.14(d)). The intensity has its maximum in the center of the entrance

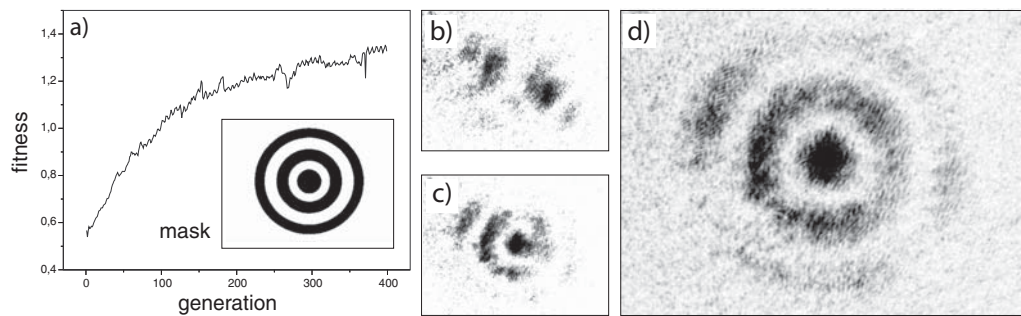


Figure 4.14: The optimization of the fiber output to a ring mode (target mask as inset in (a)). (b) shows the fiber output prior to the optimization and (c) a snapshot during the optimization process. The optimized result is (d). The graph in (a) shows the rise of the maximum fitness as a function of generation number.

hole and shows a more or less radially symmetric distribution (waist size of about $0.16a$). The corresponding phase profile in (Fig. 4.15(b)) is relatively flat (-0.5 ± 0.3 rad) in the region of high intensity. The ideal waist size that is needed to couple most efficiently into the fundamental hybrid mode, EH_{11} , of the fiber is given by $w_0 = 0.64a$ [205]. The smaller waist size of Fig. 4.15(a) is more suited to excite a higher order radially symmetric mode (Fig. 4.14(d)).

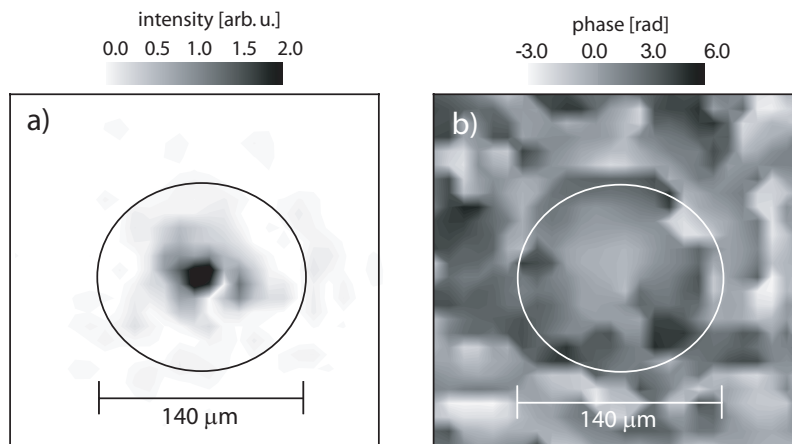


Figure 4.15: Calculated intensity distribution (a) and corresponding phase profile (b) at the fiber entrance found as the fittest phase profile of the PAL-SLM of the ring-mode optimization (Fig. 4.14). The size of the entrance hole is indicated by a circle.

The estimated intensity and phase distributions of the triple mode (Fig. 4.13f) are shown in Fig. 4.16. The intensity is divided into three different regions analogous to the distribution of the fiber output. The corresponding phase profile consists of a plateau-like structure. In each of the three high-intensity regions the phase varies only slightly but the phase offsets are different (left region 0.8 ± 1.0 rad, upper right region 3.4 ± 0.4 rad, lower right region -1.6 ± 0.4 rad).

These optimization results look promising enough to take the next step: target masks with

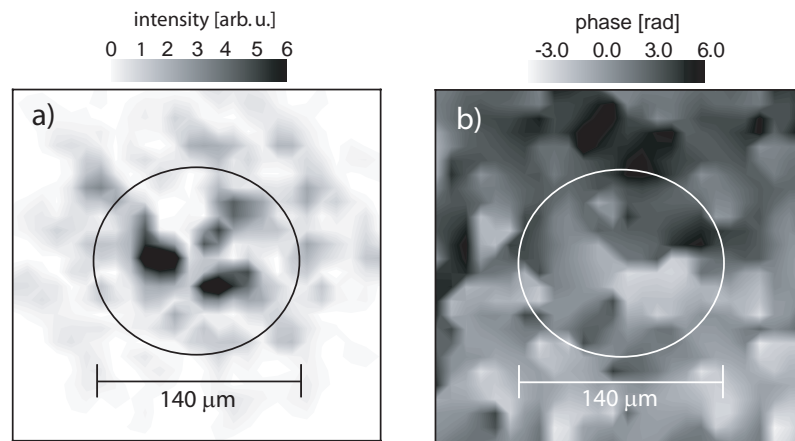


Figure 4.16: Calculated intensity distribution (a) and corresponding phase profile (b) at the fiber entrance of the fittest phase profile of the PAL-SLM of the triple-mode optimization (Fig. 4.13(f)).

arbitrarily placed spots that can not be easily constructed as a superposition of only a few low-order modes (Fig. 4.17).

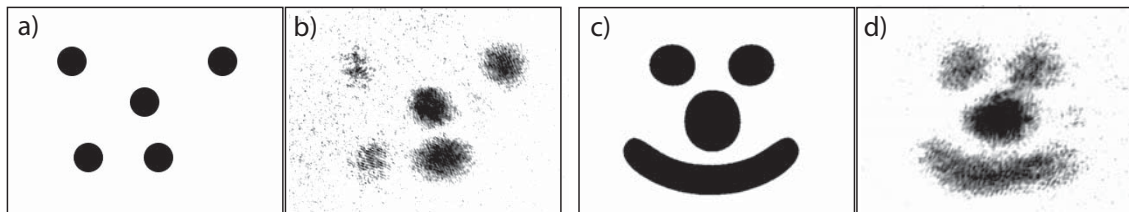


Figure 4.17: Two more complex target masks (a,c) and the corresponding optimized results (b,d). This final test proves that a suitable superposition of a large number of different fiber modes can be excited. These optimizations took about 300 generations of 40 individual pulse shapes per generation to complete.

The selective excitation of specific fiber modes and complex combinations thereof clearly shows that the PAL-SLM works excellently to influence the electric field distributions inside the fiber. During each optimization the laser focus did not miss the fiber entrance. Therefore there will be minimal or no damage done to the fiber by application of ultrashort pulses under comparable experimental conditions. In the next section this technique will be applied to shape ultrashort 800 nm femtosecond laser pulses to exert control over high-harmonic generation in a hollow fiber.

Optimization of high-harmonic generation

The laser pulses hit the active area of the PAL-SLM that was set to work with a 15×15 pixel block pattern. With a beam diameter of about 10 mm approximately 60 of these pixel blocks are illuminated with a peak intensity of about 10^{10} W/cm². The reflected

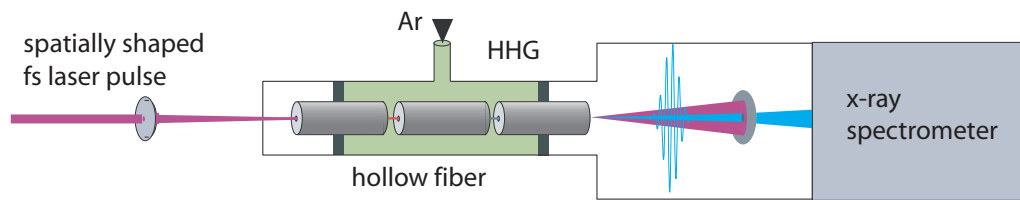


Figure 4.18: Setup used to generate high-harmonic radiation by spatially modulated ultrashort laser pulses.

beam ($300 \mu\text{J}$) is then focused through a flat AR-coated window inside a vacuum chamber into the gas-filled hollow fiber (Fig. 4.18).

Near the critical power of self-focusing inside the fiber [206,207] different fiber modes do not longer travel independently and start to mix (see Section 4). Therefore an optimization algorithm is needed that is able to manipulate the spatial properties of the driving laser. It will help to fulfill the phase-matching condition Eq. (3.9) at a certain point inside the fiber for efficient HHG.

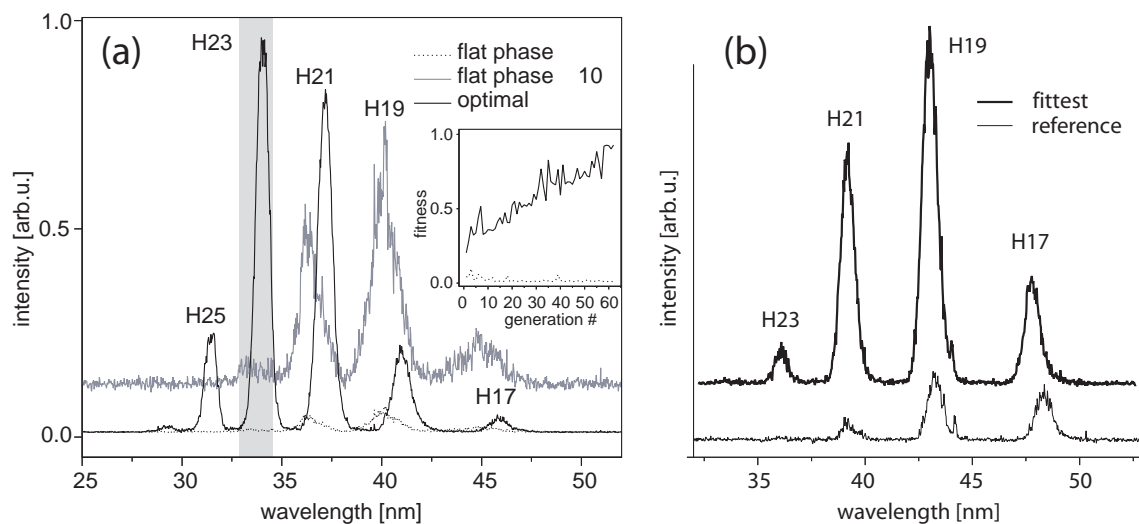


Figure 4.19: (a) Spatial laser pulse shape optimization of selective harmonic emission in a single harmonic (23rd harmonic order, see text for details). The signal in H23 is enhanced by more than two orders of magnitude, whereas the overall signal increases about tenfold. The inset shows the normalized fitness versus generation number of the evolutionary optimization. One generation was acquired in 100 seconds. (b) Optimization of the high harmonic yield with spatially shaped laser pulses. The overall signal could be increased by about a factor of 5 (upper graph; shifted by an offset for better separation) compared to the reference signal that was obtained for a flat phase profile on the PAL-SLM (lower graph).

As a first step the overall harmonic yield was used as fitness function to optimize the spatial phase of the laser pulse. The fitness function was defined as the integrated yield over the harmonic orders 17 through 23. Prior to each optimization run the setup was adjusted manually for maximum harmonic output. The reference signal was again obtained with a flat phase profile on the PAL-SLM and optimal manual adjustment of the laser focusing

point within the hollow fiber. The overall harmonic yield after running the evolutionary algorithm increased by a factor of about 5 compared to the yield of the reference signal (Fig. 4.19). The phase profile on the PAL-SLM converged to a nontrivial structure that can not be achieved by means of conventional optical components.

The pulse shaper changes the spatial intensity and phase profile of each pulse at the entrance of the fiber, changing the modes propagating inside the fiber. At high intensities the initially excited modes will start to interact more and more with each other and couple nonlinearly making a theoretical approach exceedingly difficult. An estimate of the excited fiber modes is difficult since the fiber modes that are excited at the entrance or at the exit of the fiber do not have to be the same ones that are present in the middle part of the fiber where high harmonics are predominantly generated. Therefore the spatial structure of the generated high-harmonic radiation is used as an alternative method to draw conclusions about the mode structure inside the fiber at the point where the harmonics are generated. The full two-dimensional area of the x-ray CCD camera inside the spectrometer is used to image the spatial structure of the high harmonics at the spectrometer entrance slit. Figure 4.20 shows the spatially resolved spectra of an optimization of the 23rd harmonic [208]. Due to the limited size of the x-ray CCD, only the spatial upper part of the spectra can be recorded at a time.

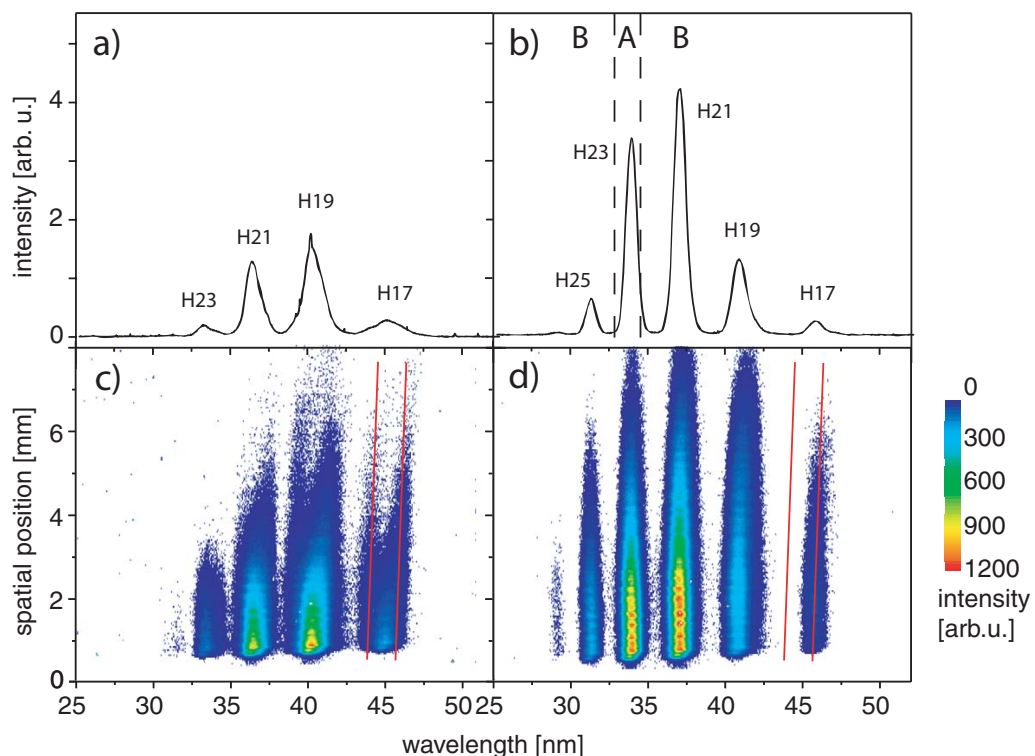


Figure 4.20: Spectra of high harmonics before (a), (c) and after (b), (d) an optimization of the signal of the 23rd harmonic (see region A in (b)) recorded at a pressure of 170 mbar. (c) and (d) show the spatially resolved data and (a) and (b) the integrated signal along the spatial coordinate. Notice the bimodal structure only visible in (c). The optimized spectrum in (d) was recorded with a factor of 10 less integration time compared to (c).

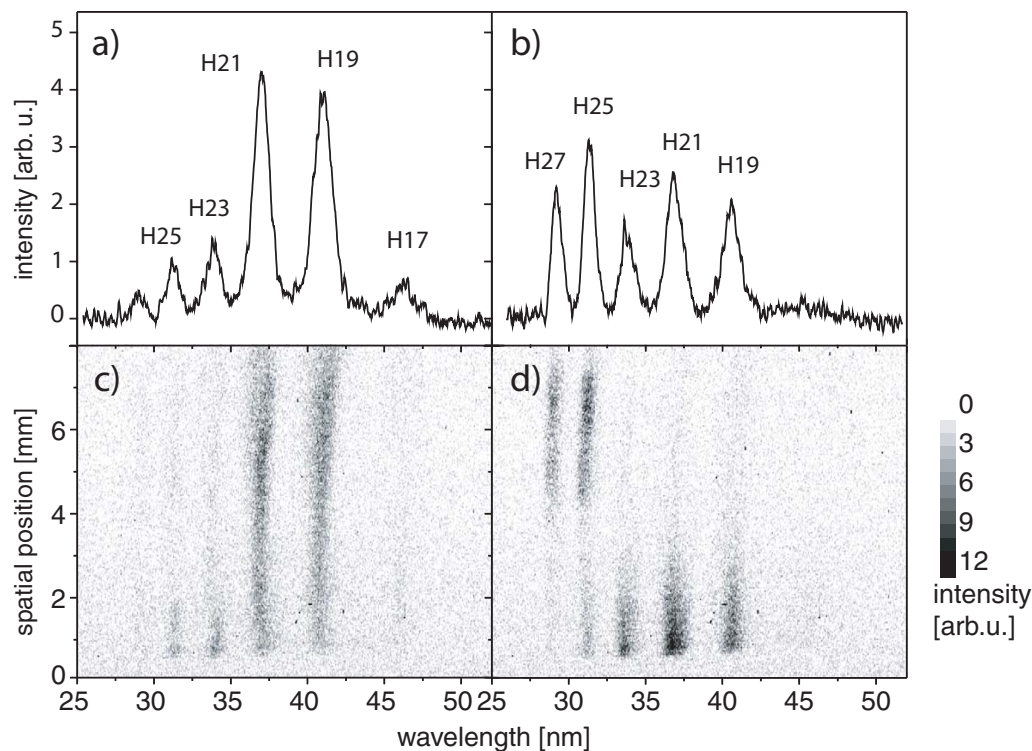


Figure 4.21: The spatially resolved harmonic spectrum obtained for the same spatial pulse profiles used in Fig. 4.20 was recorded again for a much lower pressure of 20 mbar (before (a), (c) and after (b), (d) the optimization). Here it is evident that different harmonics have different spatial profiles presumably originating from different fiber modes excited by the 800 nm driving pulse.

In Fig. 4.20(c) a bimodal structure is visible that was obtained at a pressure of 170 mbar by manually coupling into the fiber (flat phase profile on PAL-SLM). Each harmonic is split in two with different center wavelengths. This can be explained by assuming that two different fiber modes generate harmonics with different amounts of blueshift [209, 208]. This situation was taken as a starting point for a new optimization of the output of the 23rd harmonic. To check the level of possible control over the spectral shape of the harmonic spectrum the fitness function was changed to A^2/B (compare Ref. [127]), where A denotes the yield of the 23rd harmonic (region A in Fig. 4.20(b)) and B the integrated yield of the neighboring harmonic orders (region B in Fig. 4.20(b)). The 23rd harmonic could be enhanced by about two orders of magnitude, but the neighboring orders are still significantly present.

The corresponding optimization of the previous section with temporally shaped femtosecond laser pulses revealed far better results (Fig. 4.6a) indicating that additional temporal pulse shaping will be crucial for complete control of HHG. The bimodal structure disappeared indicating a clear single mode harmonic output beam. To rule out the effect that just the laser intensity inside the fiber was increased simply by an improvement of the coupling into the fiber it can be stated that there is less blueshift in the optimized spectrum compared to the unoptimized one. Therefore the enhancement of the cutoff is not due to the single-atom response alone where an increased intensity would also lead to the production of higher harmonic orders.

The unoptimized and optimized phase profiles of the PAL-SLM that were used to obtain the results of Fig. 4.20 were used again to generate harmonics at a much lower argon pressure (20 mbar) inside the hollow fiber. The corresponding spatially resolved spectra are shown in Fig. 4.21(c) and (d). At this low pressure phase-matching effects are not important and nonlinear mode coupling effects become negligible so that spatial changes in the generating pulse directly carry over to the harmonic beam. The harmonic output is low, but substantial differences in the beam shape between neighboring harmonics and corresponding orders of Fig. 4.21(c) and (d) can be seen indicating the influence of different fiber modes during the high-harmonic generation process.

The results of Fig. 4.20 suggest that it is clearly advantageous to have all laser intensity concentrated in one mode at the point where harmonics are generated inside the fiber. As has already been mentioned before, the excited fiber mode distribution changes as it propagates inside the fiber due to nonlinear mode coupling effects, being a complex function of the propagation coordinate z and the initial beam profile of the incoming laser pulse [210]. Under these circumstances adaptive pulse shaping represents a convenient method as an adaptive fiber mode filter to find the correct initial mode distribution that eventually transforms into the desired single fiber mode.

Summary and Outlook

Attosecond pulses that are generated during the process of high-harmonic generation are the fundamental tool to observe and control the electronic motion in simple atoms or more complex systems. Control of the time structure of these pulses is possible by controlling the process of high-harmonic generation with spatially or temporally tailored femtosecond light pulses.

This work developed a comprehensive approach to engineer the electric field of ultrashort laser pulses to optimize high-harmonic spectra. It also includes various techniques to enhance the conversion efficiency by designing ideal states of matter for the conversion medium. This opens the door to a wide range of possible applications of time-resolved x-ray spectroscopy and the new field of optimal quantum control in the attosecond soft x-ray region.

The temporal and spatial shaping capabilities of a high-resolution pulse shaping setup were demonstrated by adaptive compression of ultrashort laser pulses near to their bandwidth limit. Femtosecond laser pulses with durations ranging between 11 and 15 fs were generated with different optical setups on minimal time scale. Adaptive compression experiments with a hollow-fiber setup and the novel technique of filamentation were studied in detail. Next to pulse durations other important experimental parameters like stability and energy throughput of those setups were investigated with additional concern for the spatial quality of the compressed pulses.

An enhanced version of the evolutionary algorithm was developed that is able to converge up to very high resolutions in short time and can take advantage of all degrees of freedom of the pulse shaping device.

High harmonic generation in both the free-focusing and guided geometry was studied. Both the gas phase and the liquid phase were explored in experiment and theory. High harmonics in water microdroplets up to the 27th order were observed for the first time. A transition between the dominant laser soft-x-ray conversion mechanisms could be observed, identifying plasma-breakdown as the fundamental limit of high-density high-harmonic generation.

Different optimization schemes were investigated that predict enhancement of the conversion efficiency for specifically designed target media. High harmonic generation can be increased for the excited H-atom. The conversion process will also be enhanced by increasing the internuclear distance of an H_2^+ molecule. Both of these schemes have the maximization of the overlap of the returning electron wave function with the atomic core in common that maximizes the recombination probability of the electron with the ionic

core.

These simple atomic and molecular systems serve only as exemplary model systems. Similar effects are expected for more complex atoms and molecules that elude theoretical description at this time. A pump-drive scheme was proposed to excite a vibrational wave packet in of a Na_2^+ molecule to prepare the system for enhanced HHG.

Using adaptive pulse shaping techniques the temporal and spatial properties of ultrashort laser pulses were optimized to increase high-harmonic generation efficiency. In a hollow-fiber setup it was possible to qualitative shape the spectral response of the process. The selection and suppression of single harmonics were demonstrated. It was also possible to enhance or suppress larger regions of several harmonics. Excitation of specific fiber modes for high harmonic generation is possible that influence the spatial and spectral properties of the radiation. This level of control will allow to influence the outcome of experiments in the soft x-ray spectral region.

As proof of principle experiment the optimization of the branching ratio of particular fragmentation channels during the photodissociation reaction of SF_6 molecules was demonstrated even though the underlying mechanisms remain unclear.

It was also demonstrated that the degree of control over the soft x-ray shape depends on the high-harmonic generation geometry. Experiments performed in the gas jet could not reproduce optimization results that have been obtained in the waveguide geometry. The results identify propagation effects to be mainly responsible for the high degree of controllability observed in capillaries, answering long-standing debates in the field.

Controlling the spectral shape of coherent soft x-rays means that also the temporal shape of generated attosecond pulses can be engineered. New experimental equipment (an electron time-of-flight spectrometer (eTOF [211]) and a high-harmonic vacuum setup using a grazing-incidence toroidal mirror for efficient focusing of XUV-radiation [120]) is available to characterize the time structure of generated attosecond pulses (realization of an XFROG setup). This has the potential to demonstrate the first realization of an attosecond pulse shaping setup. Spectrally shaped harmonics can be applied in further experiments and it should be possible to control quantum systems on an attosecond time scale with tailored high harmonics.

Zusammenfassung und Ausblick

Attosekundenpulse, die während der Erzeugung Hoher Harmonischer entstehen, sind von fundamentaler Bedeutung zur Beobachtung oder Steuerung der Elektronendynamik in einfachen Atomen oder komplexen Systemen. Kontrolle über die Zeitstruktur dieser Pulse erhält man hierbei, indem man direkt den Erzeugungsprozess der hohen Harmonischen durch räumlich oder zeitlich geformte Femtosekundenlaserpulse beeinflusst.

In dieser Arbeit wurden verschiedene Methoden präsentiert, mit denen man durch Manipulation des elektrischen Feldes von ultrakurzen Laserpulsen das Spektrum der erzeugten hohen Harmonischen beeinflussen kann. Zusätzlich wurden Möglichkeiten gezeigt die Harmonischenausbeute durch Optimierung des Konversionsmediums zu steigern. Eine effiziente und flexible Quelle weicher Röntgenstrahlung ist für verschiedenste Anwendungen zeitaufgelöster Röntgenspektroskopie—und insbesondere dem neuen Feld der Quantenkontrolle mit Attosekunden im weichen Röntgenbereich—von großen Nutzen.

Die zeitlichen- und räumlichen Formungsmöglichkeiten eines zweidimensionalen Pulsformers, der eine sehr hohe Auflösung unterstützt, wurden demonstriert, indem ultrakurze Laserpulse bis in die Nähe ihres Bandbreitenlimits komprimiert wurden. Mit unterschiedlichen optischen Aufbauten wurden Pulsdauern zwischen 11 und 15 fs erreicht. Die adaptive Pulskompression mithilfe eines Hohlfaseraufbaus und die neue Methode der Filamentierung wurden genauer untersucht. Neben den minimal erreichbaren Pulsdauern waren dabei Strahlstabilität und Energiedurchsatz von Bedeutung. Insbesondere wurde dabei auch das räumliche Strahlprofil des komprimierten Laserpulses analysiert. Eine Verbesserung des evolutionären Algorithmus wurde speziell dafür entwickelt. Die neue Version kann in kurzer Zeit zu einem Optimierungsergebnis mit hoher Auflösung konvergieren und dadurch alle Freiheitsgrade des Pulsformers nutzen.

Die Erzeugung hoher Harmonischer wurde sowohl im einfachen Gasstrahl als auch in einer gasgefüllten Hohlkapillare, in der der Laser geführt wird, untersucht. In der flüssigen Phase konnten erstmalig Hohe Harmonische bis zur 27ten Ordnung in Wasser-Mikrotröpfchen nachgewiesen werden und der Erzeugungsmechanismus wurde grob modelliert. Neben der Plasma-Rekombinationsstrahlung, die bei hoher Teilchendichte dominiert, entstehen hohe Harmonische erst bei einer niedrigeren Dichte bei der es gerade noch nicht zum Plasma-Durchbruch kommt.

Verschiedene theoretische Modelle wurden untersucht, die versprechen die Ausbeute an hohen Harmonischen zu steigern. Dies ist möglich, falls das Erzeugungsmedium entsprechend präpariert wird. Eine Möglichkeit die Konversionseffizienz zu steigern, ist mit optisch angeregten H-Atomen zu arbeiten, eine andere, den internuklearen Abstand

von H_2^+ Molekülen zu erhöhen. In beiden Fällen wurde gezeigt, dass das Wellenpaket des Elektrons während der Propagation im Vakuum schwächer divergiert und dass es einen Zustand gibt, bei dem die Wellenfunktion der zurücklaufenden Elektronen maximalen Überlapp mit dem Atomkern hat, wodurch die Rekombinationswahrscheinlichkeit maximiert wird.

Ähnliches Verhalten wird bei komplexeren Systemen erwartet, die sich aber aufgrund ihrer Komplexität einer genaueren theoretischen Untersuchung entziehen. Die Anregung eines Wellenpakets in Na_2^+ , das als experimentell zugängliches Modellsystem fungieren könnte, wurde vorgeschlagen.

Mithilfe adaptiver Pulsformung wurde die zeitliche und räumliche Struktur von ultrakurzen Laserpulsen moduliert, um die Erzeugungseffizienz hoher Harmonischer zu optimieren. Im Hohlfaseraufbau war es möglich das erzeugte Spektrum der Harmonischen qualitativ zu manipulieren. Die selektive Verstärkung und Unterdrückung einzelner Harmonischer und einer Gruppe mehrerer Harmonischer wurde gezeigt. Die Anregung spezieller Hohlfasermodes beeinflusst die räumlichen und spektralen Eigenschaften der erzeugten weichen Röntgenstrahlung. Die erzielbare Kontrolle ist stark genug, dass man erwarten kann, dass sich dadurch Experimente in diesem Spektralbereich beeinflussen lassen.

Als kleines Testexperiment wurden ausgewählte Fragmentationskanäle von SF_6 mittels adaptiver Röntgenstrahlung gegeneinander maximiert. Dieser erste Test verlief erfolgreich, auch wenn der zugrundeliegende Kontrollmechanismus nicht aufgeklärt wurde.

Durch eine Vergleichsmessung wurde herausgefunden, dass bei der Erzeugung hoher Harmonischer im einfachen Gasstrahl nicht ein ähnlich hohes Maß an Kontrolle über die erzeugten Spektren möglich ist im Vergleich zur Wellenleitergeometrie. Dieses Ergebnis legt nahe, dass die Propagationseffekte im Wellenleiter hauptsächlich als die Ursache dafür verantwortlich gemacht werden können, was für längere Zeit zuvor noch umstritten war.

Die Form des Spektrums kohärenter Röntgenstrahlung zu steuern, heißt gleichzeitig auch, dass man damit die Zeitstruktur der dazugehörigen Attosekundenpulse modifiziert. Neue experimentelle Ausstattung (ein Elektronenflugzeitspektrometer (eTOF [211]) und eine Vakuumkammer, in der XUV-Strahlung effizient mittels streifenden Einfalls fokussiert werden kann [120]) ist verfügbar, um die Zeitstruktur der erzeugten Attosekundenpulse zu vermessen (mittels eines XFROG-Aufbaus). Dadurch steht eine Demonstration der ersten Realisation eines Attosekundenpulsformeraufbaus in greifbarer Nähe. Spektral geformte Harmonische können für zukünftige Experimente genutzt werden und es sollte dann möglich sein, Quantensysteme auf Attosekundenzeitskala zu manipulieren.

Appendix A

Programmable Phase Modulator Hamamatsu X8267

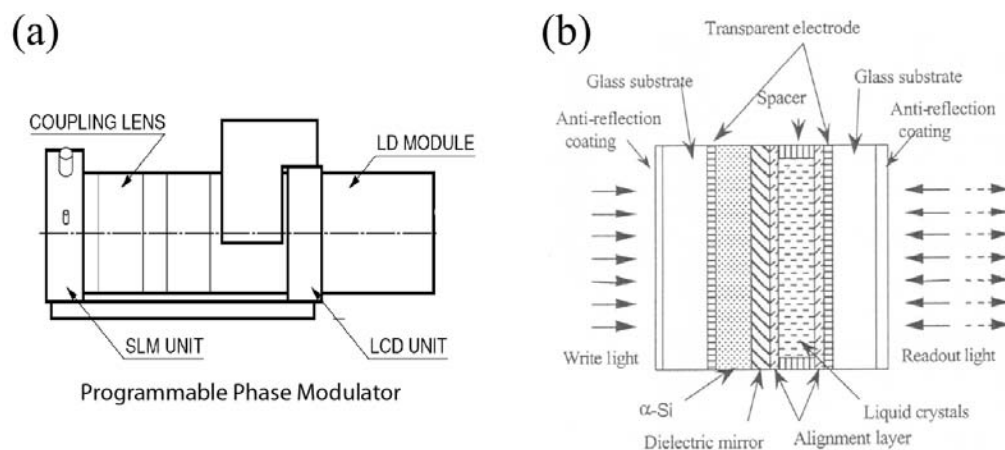


Figure A.1: (a) Schematic overview of the LCD coupled PAL-SLM module [212]. (b) “Sandwich”-structure of the PAL-SLM.

The Programmable Phase Modulator X8267 from Hamamatsu consists of parallel-aligned nematic liquid crystal spatial-light modulator (PAL-SLM) that is controlled by an internal XGA liquid crystal display (LCD with 1024×768 pixels) (Fig. A.1). “Write light” of a laser diode passes the internal LCD that works in amplitude modulation. The inner area (768×768 pixels) of two-dimensional intensity pattern of the LCD is imaged onto a photoconducting layer of hydrogenated amorphous silicon (a-Si:H). A driving voltage is applied between two transparent conductive electrodes. By illumination of the a-Si:H layer with the write light, voltage is supplied to the liquid crystal layer. The liquid crystals are aligned parallelly to each other. On application of a voltage, the molecules simply tilt with essentially no rotation about the optical axis. Therefore they will modulate the readout light for linear polarization along the original polarization of the liquid-crystals [51].

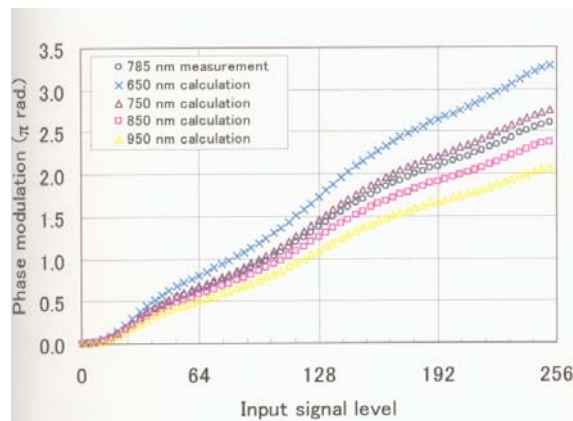


Figure A.2: Achievable phasemodulation as function of the input signal level for different wavelengths.

Working principle

Due to the imaging there are no gaps between neighboring pixels and the phase pattern will be smeared out by about 2 to 3 pixel. Therefore, there will be no energy loss caused by a limited aperture size and no diffraction noise due to a pixelated structure.

The modulation area of the PAL-SLM has a size of $20 \times 20 \text{ mm}^2$ and a reflectivity of more than 90% between 630 nm and 980 nm. The phase of each of the 768×768 pixels can be set in a range of 0 and 2π with a stepsize of $\pi/100$ at 800 nm (Fig. A.2). The PAL-SLM is easily addressable by the green value of the RGB-monitor-output (XGA) of commonly personal computers. The wavefront distortion of the unbiased PAL-SLM was measured in an interferometric setup and can be stated to be about $\lambda/10$. The response time of the modulation area is estimated to be 350 ms.

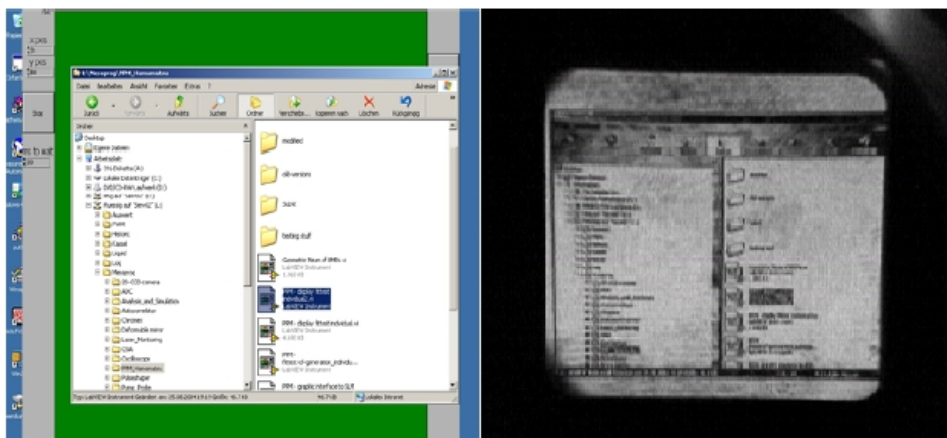


Figure A.3: Intensity modulation (b) of the picture of a windows-explorer window (a). Even small details are visible directly on the modulation area. The limiting factor of the resolution of (b) is actually the low resolution of the CCD-camera.

The device will perform phase-only modulation when the polarization direction of the read light is parallel to the orientation of the liquid crystals, but can also be operated in an intensity modulation mode. At an angle of 45 degrees only one polarization component

will get phase-modulated while the orthogonal polarization is unaffected. Using polarizers intensity modulation will be observed. To achieve complete polarization shaped pulses, laser pulses have to pass two times the modulation area at angles of 45 and -45 degrees.

Fig. A.3 gives an example of the resolution of the device in its intensity mode taken with a black-and-white CCD camera. To suppress the effect of interference speckles a rotating diffuser was placed in front of the CCD.

The PAL-SLM has a wide range of possible applications. In the course of this work it was used as monochromatic LCD-projector or as simple concave mirror with a minimal achievable focal length of about 80 cm [213]. It was even possible to realize a Shack-Hartmann wavefront sensor by subdivision of the modulation area into an array of 5×5 concave mirrors [214].

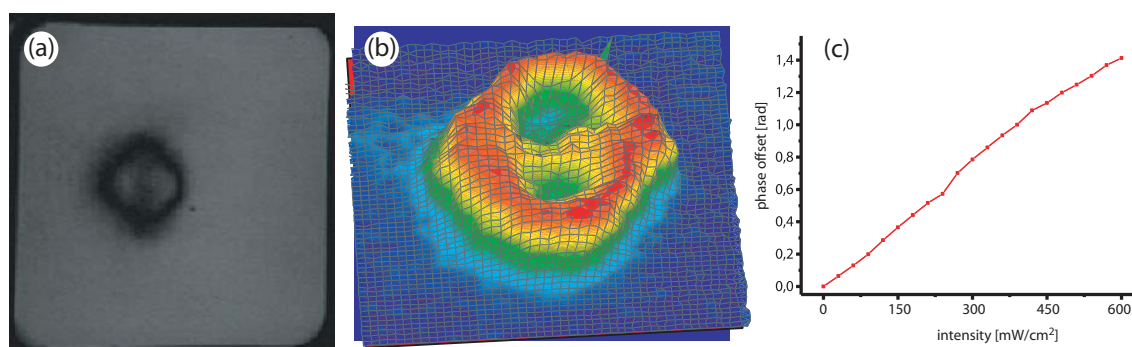


Figure A.4: “Self-phase modulation” of the PAL-SLM by high-intensity laser pulses. (a,b) Intensity modulation of the modulation area by the intensity profile of the laser pulse action that acts as “write-light”. (c) Phase-offset as function of laser intensity.

Application Notes

Spatial shaping with liquid-crystal based devices has only limited potential. The refractive index of the material can be controlled with high resolution but it is not possible to control the spatial phase profile for the full spectrum of broadband laser pulses due to dispersion (Fig. A.2). This generally will cause problems if a phase jump of 2π has to be realized in a spatial shaping setup. Only the phase of one wavelength (usually the central wavelength of 800 nm) will be shifted by 2π , all other frequencies are shifted by slightly higher or lower amounts. This inevitably causes distortions in the spatial phase profile of the laser pulse.

Another problem is connected to the parameterizing of the modulation area. If the PAL-SLM is addressed with a phase pattern that includes sharp phase jumps between neighboring pixels (phase-step of more than ≈ 0.3 rad) this step-structure will be smoothed by the device (see above). This causes unwanted steep phase gradients that will deflect part of the laser beam. This can lead to “holes” in the spectral (temporal shaping configuration) or spatial (spatial shaping configuration) intensity distribution (see Fig. A.5).

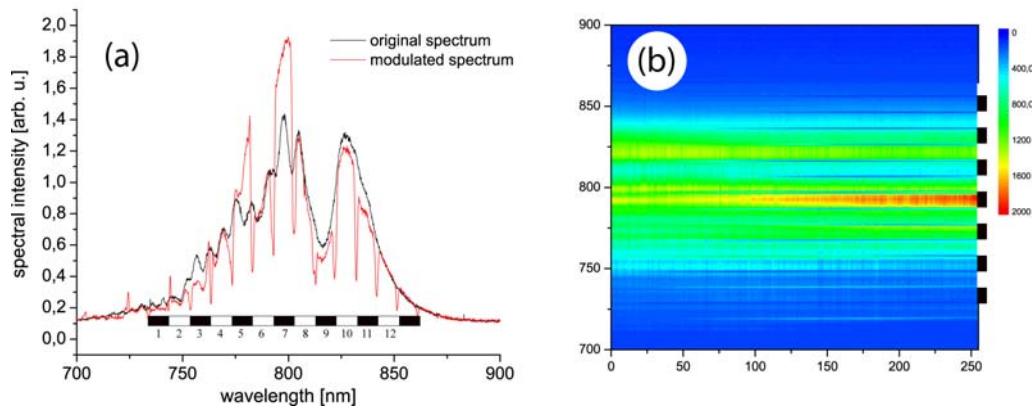


Figure A.5: (a) Effects of a stripe pattern on the PAL-SLM on the spectrum of intense laser pulses (temporal shaping configuration). Spectral holes are present at equal distances, corresponding to steep phase gradients at each phase jump of the stripe pattern. Effects on the spectral intensity within stripe number 5 and 7 are contributed to a change of polarization of the laser pulse during the interaction with the modulation area. (b) shows the corresponding evolution of the spectrum as function of the modulation depth.

Undocumented and unexpected behaviour was observed during the work with the PAL-SLM in its phase-only modulation configuration. It can be generally summarized to originate from the interaction of intense ultrashort pulses (readout light) with the orientation of the liquid crystals inside the device. Due to high peak intensities the laser pulses act as write light and can alter the original modulation pattern of the device.

As was already reported in [52] impinging laser light changes the phase offset of the modulation area without reduction of the maximal modulation depth (Fig. A.4). In the temporal shaping configuration this offset is generally compensated during a high resolution optimization, as individual phase values of pixels or group of pixels can adapt to the laser intensity. However, as already stated above, corresponding effects on the spatial beam profile (Fig. A.4a,b) in a spatial shaping configuration will cause distortions that cannot be compensated.

A new effect was discovered that also influences the polarization of impinging laser pulses. Fig. A.5 shows the unmodulated spectrum of a spectrally broadened laser pulse. Using a stripe pattern (inset of Fig. A.5a at the bottom of the spectra) as modulation signal, different effects can be observed. The grey curve of Fig. A.5a gives the spectrum that is obtained for maximal modulation depth (white stripes: input signal level 0; black stripes: input signal level 255. This corresponds to a phase difference of about 3π on the modulation area for neighboring stripes). This spectrum has been influenced. Corresponding to each of the phase jumps of the stripe-pattern spectral holes are present (consequence of steep phase-gradients as described above). More interestingly the measured intensity increased for parts of the spectrum (stripe number 5 and 7). This effect is contributed to a change of polarization of the laser pulse during the interaction with the modulation area and therefore reduced transmission through the pulse shaping setup. This effect is strongest if the internal write light (built-in laserdiode) has no effect (input signal level 0). In this case the strong readout-laser will act alone as write light and affect the PAL-SLM

(polarization changed). For an input signal level of 255 the strong readout-laser acts only partly as write light, the effect of the internal lasediode dominates (polarization (nearly) unaffected).

No permanent damage of the modulation area was observed during the experiments, therefore the damage threshold for the interaction with 30 fs pulses is estimated being at least above $3.5 \times 10^{10} \text{ W/cm}^2$.

Appendix B

Two-dimensional Implementation of the Evolutionary Algorithm

To be able to run optimizations on a reasonable time scale (\approx one hour) the gigantic parameter set of 768×768 pixels with a phase resolution of 8 bit has to be reduced. An intuitive approach is the subdivision of the modulation area into an quadratic array of $n \times n$ blocks of grouped pixels that have a constant phase value. It is easy to increase the number of degrees of freedom of the system by further subdivision of large blocks into smaller ones during the optimization. However, this implementation has its limitations due to sharp phase jumps between neighboring blocks (see Appendix A). In the beginning this problem was solved by applying a smoothing filter over the two-dimensional image of the sharp-edged block-structure before it was sent to the pulse-shaping device [52]. However, this introduces a coupling of neighboring pixel blocks as the smoothing procedure has to consider phase-amplitudes of multiple blocks to calculate the smoothed profile at a specific position. This coupling mechanism distorts the progress of the evolutionary algorithm (especially the process of crossover) and has to be avoided.

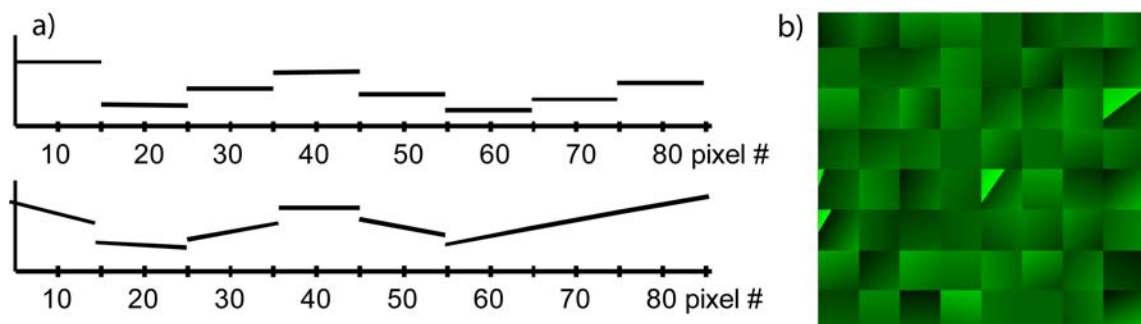


Figure B.1: (a): One-dimensional comparison of the grouping of 10 pixels to blocks of constant phase values (upper graph) with the grouping to tiltable planes (lower graph). (b) Phase-profile constructed with a matrix of 8×8 tiltable planes.

The solution of this problem is to work with pixel groups that have nonconstant phase values. The most simple realization are pixel groups that represent tilted planes that enable smooth transitions to neighboring structures (Fig. B.1). Signal limiting “holes” in the

intensity distribution (see Appendix A) can now be automatically prevented by the optimization algorithm by realization of a smooth phase surface (see for example Fig. 2.11).

In the beginning all pixels of the spatial light modulator are grouped to one big quadratic array of pixels to work as a plane surface. The only parameters that can be influenced at this stage are the tilt angles, offset position of this plane and an additional parameter that controls the phase value at which a 2π phase jump will occur.

With this reduced set of parameters the algorithm will reach a local maximum after a limited number of generations. To be able to continue the optimization at an higher resolution, additional degrees of freedom are introduced by breaking all grouped pixels of larger planes into smaller planes that will start to be tilted independently in future generations. This procedure can be repeated until a optimal phase profile is found. Thus, complicated two-dimensional phase profiles can be found as optimization results.

To maximize the speed of optimizations the phase profile of subsequent individuals are already prepared during the time of data collection for one individual. Depending on the noise level of the feedback signal the acquired laser signal was averaged over a period of 0.1 to 0.5 seconds (corresponds to an average of 100 to 500 laser pulses). For feedback-signals with low noise the dominant time limitation is the response time of the pulse shaper. The modulation area takes at least 350 ms to apply a new phase profile.

To still be able to finish optimizations with hundreds of generation on the order of few hours, the population size was drastically reduced. Only 10 individuals are used per generation. This limits the genetic pool size dramatically. However, this also limits the probability to reach the global maximum of the optimization problem. Most likely the algorithm will converge into a local maximum. This was accepted as a trait-off to minimize the time needed for optimizations.

An additional optimization parameter was introduced that could even “guide” the algorithm to a phase pattern with a smoothed profile. This is realized by influencing the mutation process. The orientation of neighboring pixel-planes is considered every time the orientation of an individual pixel-plane is changed to minimize the amount of phase jumps.

Different parameters like the mutation rate and the maximal mutation amplitude have to be chosen with care or adaptively varied during optimizations. During the compression of ultrashort laser pulses with the spatiotemporal configuration of the pulse shaping setup (Section 2.1.2) a striking drop of the fitness function was realized each time after the number of degrees of freedom of the system was doubled. This was caused by large mutation rates that changed the overall phase profile at higher degrees for higher resolutions. Fluctuations in the recorded experimental feedback signal can cause a misinterpretation during the evaluation routine of the algorithm that determines the fitness of each individual. It can happen that mutated child-individuals of one generation are wrongful chosen as fittest individuals for the next generation due to a fluctuation of the experimental feedback signal to higher fitness. The original fittest individuals will then be removed from the genetic pool. The average fitness of those “lucky” children (that now serve as new parents) may be much lower than the average fitness of their own parents. Therefore the maximal fitness can drop as function of generation number if the integration time of the feedback signal is too low and only a limited number of parent individuals are available per generation (only 2 parents were available for a generation size of 10 individuals).

Possible improvements:

At the moment, human interaction is still required to estimate “the right time” to increase the number of degrees of freedom of the optimization during its operation and to lower the mutation parameters. The ideal time to double (or multiply) the number of individual tiltable planes was estimated to be after the phase profile of a lower resolution is no longer visible as substructure of a higher resolution. It is possible to automate this process in future implementations.

Bibliography

- [1] J.-C. Diels and W. Rudolph.
Ultrashort Laser Pulse Phenomena.
Academic Press, London (1996).
- [2] R. Hellwarth.
Theory of the Pulsation of Fluorescent Light from Ruby.
Phys. Rev.Lett. **6** (1961).
- [3] A. J. DeMaria, C. M. Ferrar, and J. G. E. Danielson.
MODE LOCKING OF A Nd^{3+} -DOPED GLASS LASER.
Appl. Phys. Lett. **8**, 22–24 (1966).
- [4] J. D. Jackson.
Classical Electrodynamics, 3rd Edition.
John Wiley & Sons, Inc., New York (1999).
- [5] G. G. Paulus, F. Grasbon, H. Walther, P. Villorosi, M. Nisoli, S. Stagira, E. Priori, and S. D. Silvestri.
Absolute-phase phenomena in photoionization with few-cycle laser pulses.
Nature **414** (2001).
- [6] D. B. Milosevic, G. Paulus, and W. Becker.
Phase-Dependent Effects of a Few-Cycle Laser Pulse.
Phys. Rev. Lett. **89** (2002).
- [7] P. Agostini and L. F. DiMauro.
The physics of attosecond light pulses.
Rep. Prog. Phys. **67**, 813–855 (2004).
- [8] T. Brabec and F. Krausz.
Intense few-cycle laser fields: Frontiers of nonlinear optics.
Rev. Mod. Phys. **72**, 545–591 (2000).
- [9] C. V. Shank and E. P. Ippen.
Self-phase modulation of picosecond pulses in optical fibers.
Appl. Phys. Lett. **24**, 190–192 (1974).
- [10] P. F. Moulton.
Spectroscopic and laser characteristics of $Ti:Al_2O_3$.
J. Opt. Soc. Am. B **3**, 125 (1986).
- [11] D. E. Spence, P. N. Kean, and W. Sibbett.
60-fs Pulse Generation from a Self-Mode-Locked $Ti:Sapphire$ Laser.
Opt. Lett. **16** (1991).
- [12] J. M. Hopkins and W. Sibbett.
Ultrashort-pulse lasers: Big payoffs in a flash.
Scientific American **283**, 72–79 (2000).
- [13] D. Strickland and G. Mourou.
Compression of Amplified Chirped Optical Pulses.

- Opt. Commun. **56**, 219–221 (1985).
- [14] L. Bergmann and C. Schaefer.
Optik, volume 3 of *Lehrbuch der Experimentalphysik*.
9th edition. Walter de Gruyter, Berlin (1993).
- [15] E. T. J. Nibbering, P. F. Curley, G. Grillon, B. S. Prade, M. A. Franco, F. Salin, and A. Mysyrowicz.
Conical emission from self-guided femtosecond pulses in air.
Opt. Lett. **21**, 62 (1996).
- [16] A. Couairon.
Filamentation length of powerful laser pulses.
Appl. Phys. B **76**, 789–792 (2003).
- [17] *Wikipedia (2006)*
<http://www.wikipedia.org>.
- [18] M. Nisoli and S. De Silvestri und O. Svelto.
Generation of high energy 10 fs pulses by a new pulse compression technique.
Appl. Phys. Lett. **68**, 2793–2795 (1996).
- [19] M. Nisoli, S. D. Silvestri, O. Svelto, R. Szipöcs, K. Ferencz, C. Spielmann, S. Sartania, and F. Krausz.
Compression of high-energy laser pulses below 5 fs.
Opt. Lett. **22**, 522–524 (1997).
- [20] A. Braun, G. Korn, X. Liu, D. Du, J. Squier, and G. Mourou.
Self-channeling of high-peak-power femtosecond laser pulses in air.
Opt. Lett. **20**, 73 (1995).
- [21] E. Sidick, A. Knoesen, and A. Dienes.
Ultrashort-Pulse Second-Harmonic Generation. I. Transform-Limited Fundamental Pulses.
J. Opt. Soc. Am. B **12**, 17041712 (1995).
- [22] R. Trebino, K. W. DeLong, D. N. Fittinghoff, J. N. Sweetser, M. A. Krumbugel, B. A. Richman, and D. J. Kane.
Measuring ultrashort laser pulses in the time-frequency domain using frequencyresolved optical gating.
Rev. Sci. Instrum. **68**, 32773295 (1997).
- [23] P. Baum, S. Lochbrunner, L. Gallmann, G. Steinmeyer, U. Keller, and E. Riedle.
Real-time characterization and optimal phase control of tunable visible pulses with a flexible compressor.
Appl. Phys. B **74**, 219–224 (2002).
- [24] C. Iaconis and I. A. Walmsley.
Spectral phase interferometry for direct electric-field reconstruction of ultrashort optical pulses.
Opt. Lett. **23**, 792–794 (1998).
- [25] D. Eimerl, L. Davis, S. Velsko, E. K. Graham, and A. Zalkin.
Optical, Mechanical, and Thermal-Properties of Barium Borate.
J. Appl. Phys. **62**, 1968–1983 (1987).
- [26] T. Brixner, B. Kiefer, and G. Gerber.
Problem complexity in femtosecond quantum control.
Chem. Phys. **267**, 241–246 (2001).
- [27] T. Brixner, G. Krampert, P. Niklaus, and G. Gerber.
Generation and characterization of polarization-shaped femtosecond laser pulses.
Appl. Phys. B **74**, S133–S144 (2002).
- [28] A. M. Weiner, D. E. Leaird, A. Patel, and J. R. W. II.
Programmable shaping of femtosecond optical pulses by use of 128-element liquidcrystal phase modulator.
IEEE J. Quantum Electron. **28**, 908–920 (1992).

- [29] M. M. Wefers and K. A. Nelson.
Analysis of programmable ultrashort waveform generation using liquid-crystal spatial light modulators.
J. Opt. Soc. Am. B **12**, 1343-1362 (1995).
- [30] R. S. Judson and H. Rabitz.
Teaching lasers to control molecules.
Phys. Rev. Lett. **68**, 1500–1503 (1992).
- [31] T. Wilhelm, J. Piel, and E. Riedle.
Sub-20-fs pulses tunable across the visible from a blue-pumped single-pass noncollinear parametric converter.
Opt. Lett. **22**, 1494–1496 (1997).
- [32] A. McPherson, G. Gibson, H. Jara, U. Johann, T. S. Luk, I. A. McIntyre, K. Boyer, and C. K. Rhodes.
Studies of multiphoton production of vacuum-ultraviolet radiation in the rare gases.
J. Opt. Soc. Am. B **4**, 595–600 (1987).
- [33] M. Ferray, A. L'Huillier, X. F. Li, L. A. Lompré, G. Mainfray, and C. Manus.
Multiple-harmonic conversion of 1064 nm radiation in rare gases.
J. Phys. B **21**, L31–L35 (1988).
- [34] A. Assion, M. Geisler, J. Helbing, V. Seyfried, and T. Baumert.
Femtosecond pump-probe photoelectron spectroscopy: Mapping of vibrational wave-packet motion.
Phys. Rev. A **54**, R4605–R4608 (1996).
- [35] H. Ihee, J. Cao, and A. H. Zewail.
Ultrafast electron diffraction: structures in dissociation dynamics of Fe(CO)(5).
Chem. Phys. Lett. **281**, 10–19 (1997).
- [36] E. D. Potter, J. L. Herek, S. Pedersen, O. Liu, and A. H. Zewail.
Femtosecond laser control of a chemical reaction.
Nature **355**, 66–68 (1992).
- [37] B. Kohler, V. V. Yakovlev, J. Che, J. L. Krause, M. Messina, K. R. Wilson, N. Schwentner, R. M. Whitnell, and Y. J. Yan.
Quantum control of wave-packet evolution with tailored femtosecond pulses.
Phys. Rev. Lett. **74**, 3360–3363 (1995).
- [38] A. Assion, T. Baumert, J. Helbing, V. Seyfried, and G. Gerber.
Coherent control by a single phase shaped femtosecond laser pulse.
Chem. Phys. Lett. **259**, 488–494 (1996).
- [39] P. Gross, H. Singh, H. Rabitz, K. Mease, and G. M. Huang.
Inverse quantum-mechanical control: A means for design and a test of intuition.
Phys. Rev. A **47**, 4593–4604 (1993).
- [40] V. I. Prokhorenko, A. M. Nagy, A. W. S. L. S. Brown, R. R. Birge, and R. J. D. Miller.
Coherent Control of Retinal Isomerization in Bacteriorhodopsin.
Science **313**, 1257–1261 (2006).
- [41] R. Williams, J. Shear, W. Zipfel, S. Maiti, and W. Webb.
Mucosal Mast Cell Secretion Processes Imaged Using Three-photon Microscopy of 5-Hydroxytryptamine Autofluorescence.
Biophys. J. **76**, 1835–1846 (1999).
- [42] D. Huang, E. A. Swanson, C. P. Lin, J. S. Schuman, W. G. Stinson, W. Chang, M. R. Hee, T. Flotte, K. Gregory, C. A. Puliafito, and J. G. Fujimoto.
Optical Coherence Tomography.
Science **254**, 1178–1181 (1991).

- [43] C. N. Danson, P. A. Brummitt, R. J. Clarke, J. L. Collier, G. Fell, A. J. Frackiewicz, S. Hancock, S. Hawkes, C. Hernandez-Gomez, P. Holligan, M. H. R. Hutchinson, A. Kidd, W. J. Lester, I. O. Musgrave, D. Neely, D. R. Neville, P. A. Norreys, D. A. Pepler, C. J. Reason, W. Shaikh, T. B. Winstone, R. W. W. Wyatt, and B. E. Wyborn.
Vulcan petawatt - an ultra-high-intensity interaction facility.
Nucl. Fusion 44 **44**, 239–249 (2004).
- [44] T. Tajima and J. M. Dawson.
Laser Electron Accelerator.
Phys. Rev. Lett. **43**, 267–270 (1979).
- [45] T. Katsouleas.
Electrons hang ten on laser wake.
Nature **431**, 515 (2004).
- [46] G. Pretzler, A. Saemann, A. Pukhov, D. Rudolph, T. Schätz, U. Schramm, P. Thirolf, D. Habs, K. Eidmann, G. D. Tsakiris, J. M. ter Vehn, and K. J. Witte.
Neutron production by 200 mJ ultrashort laser pulses.
Phys. Rev. E **58**, 1165–1169 (1998).
- [47] M. Li, M. Ishizuka, X. Liu, Y. Sugimoto, N. Ikeda, and K. Asakawa.
Nanostructuring in submicron-level waveguides with femtosecond laser pulses.
Opt. Commun. **212**, 159–163 (2002).
- [48] A. Vorobyev and C. Guo.
Femtosecond laser nanostructuring of metals.
Opt. Expr. **14**, 2164 (2006).
- [49] T. Udem, R. Holzwarth, and T. W. Hänsch.
Optical frequency metrology.
Nature **416**, 233–237 (2002).
- [50] *Parametric Aligned Nematic Liquid Crystal Spatial Light Modulator X7665.*
HAMAMATSU Photonics K.K., <http://www.hamamatsu.com>, info@hamamatsu.de.
- [51] Y. Kobayashi, Y. Igasaki, N. Yoshida, H. T. N. Fukuchi, T. Hara, and M. H. Wu.
Compact High-efficiency Electrically-addressable Phase-only Spatial Light Modulator.
Diffractive/Holographic Technologies and Spatial Light Modulators VII, Proceedings of SPIE **3951**, 158–165 (2000).
- [52] R. Kemmer.
Adaptive räumliche und zeitliche Formung von ultrakurzen Laserpulsen.
Diplomarbeit, Universität Würzburg (2005).
- [53] D. Walter, S. Eyring, J. Lohbreier, R. Spitzenpfeil, and C. Spielmann.
Two-dimensional evolutionary algorithm designed for high resolutions.
in preparation (2006).
- [54] F. Dimler.
Adaptive Formung von Laserpuls-Spektren im mittleren Infrarot.
Diplomarbeit, Universität Würzburg (2005).
- [55] M. Nisoli, E. Priori, G. Sansone, S. Stagira, G. Cerullo, S. DeSilvestri, C. Altucci, R. Bruzzese, C. de Lisio, P. Villoresi, L. Poletto, M. Pascolini, and G. Tondello.
High-brightness high-order harmonic generation by truncated Bessel beams in the sub-10-fs regime.
Phys. Rev. Lett. **88**, 033902 (2002).
- [56] K. Yamane, Z. G. Zhang, K. Oka, R. Morita, M. Yamashita, and A. Suguro.
Optical pulse compression to 3.4 fs in the monocycle region by feedback phase compensation.
Opt. Lett. **28**, 2258–2260 (2003).
- [57] B. Schenkel, J. Biegert, U. Keller, C. Vozzi, M. Nisoli, G. Sansone, S. Stagira, S. DeSilvestri, and O. Svelto.

- Generation of 3.8-fs pulses from adaptive compression of a cascaded hollow fiber supercontinuum.*
Opt. Lett. **28**, 1987–1989 (2003).
- [58] N. L. Wagner, E. A. Gibson, T. Popmintchev, I. P. Christov, M. M. Murnane, and H. C. Kapteyn.
Self-Compression of Ultrashort Pulses through Ionization-Induced Spatiotemporal Reshaping.
Phys. Rev. Lett. **93**, 173902 (2004).
- [59] R. Szipocs, K. Ferencz, C. Spielmann, and F. Krausz.
Chirped Multilayer Coatings for Broad-Band Dispersion Control in Femtosecond Lasers.
Opt. Lett. **19**, 201–203 (1994).
- [60] S. K. M. Batzer.
Entwurf und Umsetzung eines steuerbaren Spiegelhalters.
Projektpraktikum, Universität Würzburg (2006).
- [61] L. Wöste, C. Wedekind, H. Wille, P. Rairoux, B. Stein, S. Nikolov, C. Werner, S. Niedermeier,
H. Schillinger, and R. Sauerbrey.
Femtosecond Atmospheric Lamp.
Laser Optoelektron. **29**, 51 (1997).
- [62] A. Couairon, J. B. J., C. P. Hauri, W. Kornelis, F. W. Helbing, U. Keller, and A. Mysyrowics.
Self-compression of ultra-short laser pulses down to one optical cycle by filamentation.
J. Mod. Opt. **53**, 75–85 (2006).
- [63] A. Guandalini, P. Eckle, M. Anscombe, P. Schlup, J. Biegert, and U. Keller.
5.1 fs pulses generated by filamentation and carrier envelope phase stability analysis.
J. Phys. B **39**, 257–264 (2006).
- [64] C. Hauri, W. Kornelis, F. Helbing, A. Heinrich, A. Couairon, A. Mysyrowicz, J. Biegert, and
U. Keller.
Generation of intense, carrier-envelope phase-locked few-cycle laser pulses through filamentation.
Appl. Phys. B **79**, 673677 (2004).
- [65] M. Mäder.
Nonlinear Frequency Conversion of Ti:Sapphire Laser Pulses for Spectroscopy.
Diplomarbeit, Universität Würzburg (2006).
- [66] S. Chin, A. Talebpour, J. Yang, S. Petit, V. Kandidov, O. Kosareva, and M. Tamarov.
Filamentation of femtosecond laser pulses in turbulent air.
Appl. Phys. B. **74**, 67–76 (2002).
- [67] H. Schroeder and S. L. Chin.
Visualization of the evolution of multiple filaments in methanol.
Opt. Commun. pp. 399–406 (2004).
- [68] M. Mlejnek, M. Kolesik, J. Moloney, and E. Wright.
Optically Turbulent Femtosecond Light Guide. in Air.
Phys. Rev. Lett. **83**, 2938 (1999).
- [69] A. Hosseini, Q. Luo, B. Ferland, W. Liu, S. L. Chin, O. G. Kosareva, N. A. Panov, N. Akozbek,
and V. P. Kandidov.
Competition of multiple filaments during the propagation of intense femtosecond laser pulses.
Phys. Rev. A **70** (2004).
- [70] W. Liu, S. A. Hosseini, Q. Luo, B. Ferland, S. L. Chin, O. G. Kosareva, N. A. Panov, and V. P.
Kandidov.
*Experimental observation and simulations of the self-action of white light laser pulse propagating
in air.*
New Journal of Physics **6**, 6 (2004).
- [71] M. Centurion, Y. Pu, M. Tsang, , and D. Psaltis.
Dynamics of filament formation in a Kerr medium.
Phys. Rev. A **71**, 063811 (2005).

- [72] O. Kosareva, V. P. Kandidov, A. Brodeur, C. Y. Chien, and S. L. Chin.
Conical emission from laser plasma interactions in the filamentation of powerful ultrashort laser pulses in air.
Opt. Lett. **22**, 1332–1334 (1997).
- [73] B. Prade, M. Franco, A. Mysyrowics, A. Couairon, H. Buersing, B. Eberle, M. Krenz, D. Seiffer, and O. Vasseur.
Spatial mode cleaning by femtosecond filamentation in air.
Opt. Lett. **31**, 2601–2603 (2006).
- [74] T. Pfeifer, L. Gallmann, M. J. Abel, D. M. Neumark, and S. R. Leone.
Circular phase mask for control and stabilization of single optical filaments.
Opt. Lett. **31**, 2326–2328 (2006).
- [75] P. B. Corkum.
Plasma Perspective on Strong-Field Multiphoton Ionization.
Phys. Rev. Lett. **71**, 1994–1997 (1993).
- [76] K. C. Kulander, K. J. Schafer, and J. L. Krause.
Dynamics of short-pulse excitation and ionization and harmonic generation, pp. 95–110.
Plenum Press, New York (1993).
- [77] M. Hentschel, R. Kienberger, C. Spielmann, G. A. Reider, N. Milosevic, T. Brabec, P. Corkum, U. Heinzmann, M. Drescher, and F. Krausz.
Attosecond metrology.
Nature **414**, 509–513 (2001).
- [78] P. M. Paul, E. S. Toma, P. Breger, G. Mullot, F. Augé, P. Balcou, H. G. Muller, and P. Agostini.
Observation of a Train of Attosecond Pulses from High Harmonic Generation.
Science **292**, 1689–1692 (2001).
- [79] B. Sheehy, J. D. D. Martin, L. F. DiMauro, P. Agostini, K. J. Schafer, M. B. Gaarde, and K. C. Kulander.
High Harmonic Generation at Long Wavelengths.
Phys. Rev. Lett. **83**, 5270–5273 (1999).
- [80] J.-F. Hergott, M. Kovacev, H. Merdji, C. Hubert, Y. Mairesse, E. Jean, P. Breger, P. Agostini, B. Carré, and P. Salières.
Extreme-ultraviolet high-order harmonic pulses in the microjoule range.
Phys. Rev. A **66**, 021801(R) (2002).
- [81] S. Kazamias, D. Douillet, F. Weihe, C. Valentin, A. Rousse, S. Sebban, Grillon, F. Augé, D. Hulin, and P. Balcou.
Global Optimization of High Harmonic Generation.
Phys. Rev. Lett. **90**, 193901 (2003).
- [82] S. Augst, D. D. Meyerhofer, D. Strickland, and S. L. Chin.
Laser ionization of noble gases by Coulomb-barrier suppression.
J. Opt. Soc. Am. B **8**, 858–867 (1991).
- [83] L. V. Keldysh.
Ionization in the field of a strong electromagnetic wave.
Soviet Physics JETP **20**, 1307–1314 (1965).
- [84] M. Lewenstein, P. Balcou, M. Y. Ivanov, A. L’Huillier, and P. B. Corkum.
Theory of high-harmonic generation by low-frequency laser fields.
Phys. Rev. A **49**, 2117–2132 (1994).
- [85] K. J. Schafer, B. Yang, L. F. DiMauro, and K. C. Kulander.
Above Threshold Ionization Beyond the High Harmonic Cutoff.
Phys. Rev. Lett. **70**, 1599–1602 (1993).
- [86] L. D. Landau.
Quantum Mechanics.

- Pergamon, New York (1964).
- [87] N. B. Delone and V. P. Krainov.
Atoms in Strong Fields.
Springer-Verlag, Heidelberg (1985).
- [88] P. Salières, B. Carré, L. L. Déroff, F. Grasbon, G. G. Paulus, H. Walther, R. Kopold, W. Becker, D. B. Milošević, A. Sanpera, and M. Lewenstein.
Feynman's Path-Integral Approach for Intense-Laser-Atom Interactions.
Science **292**, 902–905 (2001).
- [89] M. B. Gaarde, F. Salin, E. Constant, P. Balcou, K. J. Schafer, K. C. Kulander, and A. L'Huillier.
Spatiotemporal separation of high harmonic radiation into two quantum path components.
Phys. Rev. A **59**, 1367–1373 (1999).
- [90] P. Balcou, A. S. Dederichs, M. B. Gaarde, and A. L'Huillier.
Quantum-path analysis and phase matching of high-order harmonic generation and high-order frequency mixing processes in strong laser fields.
J. Phys. B **32**, 2973–2989 (1999).
- [91] D. G. Lee, J. H. Kim, K. H. Hong, and C. H. Nam.
Coherent control of high-order harmonics with chirped femtosecond laser pulses.
Phys. Rev. Lett. **8724**, 243902 (2001).
- [92] H. T. Kim, D. G. Lee, K. H. Hong, J. H. Kim, I. W. Choi, and C. H. Nam.
Continuously tunable high-order harmonics from atoms in an intense femtosecond laser field.
Phys. Rev. A **67**, 051801 (2003).
- [93] R. Bartels, S. Backus, E. Zeek, L. Misoguti, G. Vdovin, I. P. Christov, M. M. Murnane, and H. C. Kapteyn.
Shaped-pulse optimization of coherent emission of high-harmonic soft-X-rays.
Nature **406**, 164–166 (2000).
- [94] I. P. Christov, R. Bartels, H. C. Kapteyn, and M. M. Murnane.
Attosecond Time-Scale Intra-atomic Phase Matching of High Harmonic Generation.
Phys. Rev. Lett. **86**, 5458–5461 (2001).
- [95] M. D. Feit, J. A. Fleck, Jr., and A. Steiger.
Solution of the Schrödinger equation by a spectral method.
J. Comput. Phys. **47**, 412–433 (1982).
- [96] P. M. Paul, E. S. Toma, P. Breger, G. Mullot, F. Audebert, P. Balcou, H. G. Muller, and P. Agostini.
Science **292**, 1689 (2001).
- [97] Y. Mairesse, A. de Bohan, L. J. Frasinski, H. Merdji, L. C. Dinu, P. Monchicourt, P. Breger, M. Kovačev, R. Taïeb, B. Carré, H. G. Muller, P. Agostini, and P. Salières.
Attosecond synchronization of high-harmonic soft x-rays.
Science **302**, 1540–1543 (2003).
- [98] R. Lopez-Martens, K. Varjù, P. Johnsson, J. Mauritsson, Y. Mairesse, P. Salières, M. B. Gaarde, K. J. Schafer, A. Persson, S. Svanberg, C.-G. Wahlström, and A. L'Huillier.
Amplitude and Phase Control of Attosecond Light Pulses.
Phys. Rev. Lett. **94** (2005).
- [99] P. Siffalovic, M. Drescher, M. Spieweck, T. Wiesenath, Y. C. Lim, R. Weidner, A. Elizarov, and U. Heinzmann.
Laser-based apparatus for extended ultraviolet femtosecond time-resolved photoemission spectroscopy.
Rev. Sci. Instr. **72**, 30–35 (2001).
- [100] D. Oron, Y. Silberberg, N. Dudovich, and D. M. Villeneuve.
Efficient polarization gating of high-order harmonic generation by polarization-shaped ultrashort pulses.
Phys. Rev. A **72**, 063816 (2006).

- [101] Z. H. Chang, A. Rundquist, H. W. Wang, M. M. Murnane, and H. C. Kapteyn.
Generation of Coherent Soft X Rays at 2.7 nm Using High Harmonics.
Phys. Rev. Lett. **79**, 2967–2970 (1997).
- [102] E. Seres, J. Seres, F. Krausz, and C. Spielmann.
Generation of Coherent Soft-X-Ray Radiation Extending Far Beyond the Titanium L Edge.
Phys. Rev. Lett. **92**, 163002 (2004).
- [103] J. Seres, E. Seres, A. J. Verhoef, G. Tempea, C. Strelti, P. Wobrauschek, V. Yakovlev, A. Scrinzi, C. Spielmann, and F. Krausz.
Laser technology: Source of coherent kiloelectronvolt X-rays.
Nature **433**, 596 (2005).
- [104] R. Kienberger, M. Hentschel, M. Uiberacker, C. Spielmann, M. Kitzler, A. Scrinzi, M. Wieland, T. Westerwalbesloh, U. Kleineberg, U. Heinzmann, M. Drescher, and F. Krausz.
Steering attosecond electron wave packets with light.
Science **297**, 1144–1148 (2002).
- [105] E. M. Kosik, L. Corner, A. S. Wyatt, E. Cormier, I. A. Walmsley, and L. F. DiMauro.
Complete characterization of attosecond pulses.
J. Mod. Opt. **52**, 361–378 (2005).
- [106] P. Tzallas, D. Charalambidis, N. A. Papadogiannis, K. Witte, and G. D. Tsakiris.
Direct observation of attosecond light bunching.
Nature **426**, 267–271 (2003).
- [107] M. Drescher, M. Hentschel, R. Kienberger, G. Tempea, C. Spielmann, G. A. Reider, P. B. Corkum, and F. Krausz.
X-ray Pulses Approaching the Attosecond Frontier.
Science **291**, 1923–1927 (2001).
- [108] T. Sekikawa, T. Katsura, S. Miura, and S. Watanabe.
Measurement of the intensity-dependent atomic dipole phase of a high harmonic by frequency-resolved optical gating.
Phys. Rev. Lett. **88**, 193902 (2002).
- [109] J. Itatani, F. Quéré, G. L. Yudin, M. Y. Ivanov, F. Krausz, and P. B. Corkum.
Attosecond streak camera.
Phys. Rev. Lett. **88**, 173903 (2002).
- [110] H. G. Muller.
Reconstruction of attosecond harmonic beating by interference of two-photon transitions.
Appl. Phys. B **74**, 17–21 (2002).
- [111] L. C. Dinu, H. G. Muller, S. Kazamias, G. Mullot, F. Augé, P. Balcou, P. M. Paul, M. Kovačev, P. Breger, and P. Agostini.
Measurement of the subcycle timing of attosecond XUV bursts in high-harmonic generation.
Phys. Rev. Lett. **91**, 063901 (2003).
- [112] Y. Mairesse, O. Gobert, P. Breger, H. Merdji, P. Meynadier, P. Monchicourt, M. Perdrix, P. Salières, , and B. Carre.
High Harmonic XUV Spectral Phase Interferometry for Direct Electric-Field Reconstruction.
Phys. Rev. Lett. **94** (2005).
- [113] R. Zerne, C. Altucci, M. Bellini, M. B. Gaarde, T. W. Hänsch, C. L. A. L’Huillier, and C.-G. Wahlström.
Phase-Locked High-Order Harmonic Sources.
Phys. Rev. Lett. **79**, 1006–1009 (1997).
- [114] A. Flettner, J. Günther, M. B. Mason, U. Weichmann, R. Düren, and G. Gerber.
High harmonic generation at 1 kHz repetition rate with a pulsed valve.
Appl. Phys. B **73**, 129–132 (2001).

- [115] B. Shan and Z. Chang.
Dramatic extension of the high-order harmonic cutoff by using a long-wavelength driving field.
Phys. Rev. A **65** (2001).
- [116] P. Antoine, A. L’Huillier, and M. Lewenstein.
Attosecond Pulse Trains Using High-Order Harmonics.
Phys. Rev. Lett. **77**, 1234–1237 (1996).
- [117] P. Salières, A. L’Huillier, and M. Lewenstein.
Coherence Control of High-Order Harmonics.
Phys. Rev. Lett. **74**, 3776–3779 (1995).
- [118] Y. Mairesse, A. de Bohan, L. J. Frasinski, H. Merdji, L. C. Dinu, P. Monchicourt, P. Breger, M. Kovacev, T. Auguste, B. Carre, H. Muller, P. Agostini, and P. Salières.
Optimization of Attosecond Pulse Generation.
Phys. Ref. Lett. **93** (2004).
- [119] M. Bellini, C. Lyngå, A. Tozzi, M. Gaarde, T. Hänsch, A. L’Huillier, and C.-G. Wahlström.
Temporal Coherence of Ultrashort High-Order Harmonic Pulses.
Phys. Rev. Lett. **81**, 297–300 (1998).
- [120] S. Eyring.
Konstruktion und Bau eines Spektrometers für den XUV-Bereich zur Charakterisierung von Hohen Harmonischen.
Diplomarbeit, Universität Würzburg (2006).
- [121] M. Schnürer, Z. Cheng, M. Hentschel, G. Tempea, P. Kalman, T. Brabec, and F. Krausz.
Absorption-Limited Generation of Coherent Ultrashort Soft-X-Ray Pulses.
Phys. Rev. Lett. **83**, 722–725 (1999).
- [122] M. Schnürer, Z. Cheng, M. Hentschel, F. Krausz, T. Wilhein, D. Hambach, G. Schmahl, M. Drescher, Y. Lim, and U. Heinzmann.
Few-cycle-driven XUV laser harmonics: generation and focusing.
Appl. Phys. B **70**, S227–S232 (2000).
- [123] *X-Ray Interactions With Matter (2006)*
http://www-cxro.lbl.gov/optical_constants/.
- [124] C. Altucci, R. Bruzzese, C. de Lisio, S. S. M. Nisoli, S. D. Silvestri, O. Svelto, A. Boscolo, P. Ceccherini, L. Poletto, G. Tondello, and P. Villorosi.
Tunable soft-x-ray radiation by high-order harmonic generation.
PRA **61** (2000).
- [125] P. Villorosi, S. Bonora, M. Pascolini, and G. L. Poletto.
Optimization of high-order harmonic generation by adaptive control of a sub-10-fs pulse wave front.
Opt.Lett **29**, 207–209 (2004).
- [126] D. Yoshitomi, J. Nees, N. M. T. Sekikawa, T. Kanai, G. Mourou, and S. Watanabe.
Phase-matched enhancements of high-harmonic soft X-rays by adaptive wave-front control with a genetic algorithm.
Appl. Phys. B pp. 275–280 (2004).
- [127] T. Pfeifer, D. Walter, C. Winterfeldt, C. Spielmann, and G. Gerber.
Adaptive engineering of coherent soft x-rays.
Appl. Phys. B **80**, 277–280 (2005).
- [128] A. Rundquist, C. G. Durfee III, Z. Chang, C. Herne, S. Backus, M. M. Murnane, and H. C. Kapteyn.
Phase-Matched Generation of Coherent Soft X-rays.
Science **280**, 1412–1415 (1998).
- [129] E. A. J. Marcatili and R. A. Schmelzter.
Hollow Metallic and Dielectric Waveguides for Long Distance Optical Transmission and Lasers.

- The Bell System Techn. J. **43**, 1783–1809 (1964).
- [130] E. Constant, D. Garzella, P. Breger, E. Mevel, C. Dorrer, C. LeBlanc, F. Salin, and P. Agostini.
Optimizing High Harmonic Generation in Absorbing Gases: Model and Experiment.
Phys. Rev. Lett. **82**, 1668–1671 (1999).
- [131] E. A. Gibson, A. Paul, N. Wagner, R. Tobey, D. Gaudiosi, S. Backus, I. P. Christov, A. Aquila, E. M. Gullikson, D. T. Attwood, M. M. Murnane, and H. C. Kapteyn.
Coherent Soft X-ray Generation in the Water Window with Quasi-Phase Matching.
Science **302**, 95–98 (2003).
- [132] X. Zhang, A. R. Libertun, A. Paul, E. Gagnon, S. Backus, I. P. Christov, M. M. Murnane, H. C. Kapteyn, R. A. Bartels, Y. Liu, and D. T. Attwood.
Highly coherent light at 13 nm generated by use of quasi-phase-matched high-harmonic generation.
Opt. Lett. **29**, 1357–1359 (2004).
- [133] P. A. Norreys, M. Zepf, S. Moustazis, A. P. Fews, J. Zhang, P. Lee, M. Bakarezos, C. N. Danson, A. Dyson, P. Gibbon, P. Loukakos, D. Neely, F. N. Walsh, J. S. Wark, and A. E. Dangor.
Efficient Extreme UV Harmonics Generated from Picosecond Laser Pulse Interactions with Solid Targets.
Phys. Rev. Lett. **76**, 1832–1835 (1996).
- [134] K. Z. Hatsagortsyan and C. H. Keitel.
X-ray amplification by laser controlled coherent bremsstrahlung.
Phys. Rev. Lett. **86**, 2277–2280 (2001).
- [135] J. Zheng, W. Hsieh, . Shu-chi Chen, and R. K. Chang.
Laser-induced breakout and detonation waves in droplets. I. Experiments.
J. Opt. Soc. Am. B **8**, 319–329 (1991).
- [136] J. C. Carls, Y. Seo, and J. R. Brock.
Laser-induced breakout and detonation waves in droplets. II. Model.
J. Opt. Soc. Am. B **8**, 329–337 (1991).
- [137] S. Düsterer, H. Schwoerer, W. Ziegler, C. Ziener, and R. Sauerbrey.
Optimization of EUV radiation yield from laser-produced plasma.
Appl. Phys. B **73**, 693–698 (2001).
- [138] S. J. McNaught, J. Fan, E. Parra, and H. M. Milchberg.
A pump–probe investigation of laser-droplet plasma dynamics.
Appl. Phys. Lett. **79**, 4100–4102 (2001).
- [139] T. D. Donnelly, T. Ditmire, K. Neuman, M. D. Perry, and R. W. Falcone.
High-Order Harmonic Generation in Atom Clusters.
Phys. Rev. Lett. **76**, 2472 (1996).
- [140] T. Ditmire, T. Donnelly, R. W. Falcone, and M. D. Perry.
Strong X-Ray Emission from High-Temperature Plasmas Produced by Intense Irradiation of Clusters.
Phys. Rev. Lett. **75**, 3122 (1995).
- [141] T. Ditmire, T. Donnelly, A. M. Rubenchik, R. W. Falcone, and M. D. Perry.
Interaction of intense laser pulses with atomic clusters.
Phys. Rev. A **53**, 3379–3402 (1996).
- [142] A. Flettner.
Erzeugung von XUV Strahlung an Mikrotröpfchen und Interferenzen von freien Elektronen-Wellenpaketen.
Diplomarbeit, Universität Würzburg (2002).
- [143] R. Keenan, C. L. S. Lewis, J. Wark, and E. Wolfrum.
Measurements of the XUV transmission of aluminium with a soft x-ray laser.
J. Phys. B **35**, 447–451 (2002).

- [144] C. Favre, V. Boutou, S. C. Hill, W. Zimmer, M. Krenz, H. Lambrecht, J. Yu, R. K. Chang, L. Woeste, and J. P. Wolf.
White-Light Nanosource with Directional Emission.
Phys. Rev. Lett. **89**, 035002 (2002).
- [145] J. H. Eickmans, W.-F. Hsieh, and R. K. Chang.
Laser-induced explosion of H₂O droplets: spatially resolved spectra.
Opt. Lett. **12**, 22–24 (1987).
- [146] A. N. Zaidel', V. K. Prokof'ev, S. M. Raiskii, V. A. Slavnyi, and E. Y. Shreider.
Tables of Spectral Lines.
IFI/Plenum, New York-London (1970).
- [147] *NIST, Atomic Spectra Database (2003)*
<http://physics.nist.gov/PhysRefData/ASD/index.html>.
- [148] A. Flettner, T. Pfeifer, D. Walter, C. Winterfeldt, C. Spielmann, and G. Gerber.
High-harmonic generation and plasma radiation from water microdroplets.
Appl. Phys. B **77**, 747–751 (2003).
- [149] V. Kumarappan, M. Krishnamurthy, and D. Mathur.
Explosions of water clusters in intense laser fields.
Phys. Rev. A **67**, 063207 (2003).
- [150] V. V. Strelkov, V. T. Platonenko, and A. Becker.
High-harmonic generation in a dense medium.
Phys. Rev. A **71** (2005).
- [151] V. V. Strelkov, V. T. Platonenko, and A. Becker.
Generation of Attosecond Pulses in a Dense Medium.
Laser Physics **6**, 799 (2005).
- [152] J. Biegert, A. Heinrich, C. P. Hauri, W. Kornelis, P. Schlup, M. P. Anscombe, M. B. Gaarde, K. J. Schafer, and U. Keller.
Control of high-order harmonic emission using attosecond pulse trains.
Journal of Modern Optics **53**, 87–96 (2006).
- [153] T. Kreibich, M. Lein, V. Engel, and E. K. U. Gross.
Even-Harmonic Generation due to Beyond-Born-Oppenheimer Dynamics.
Phys. Rev. Lett. **87**, 103901 (2001).
- [154] I. P. Christov, M. M. Murnane, and H. C. Kapteyn.
High-harmonic generation of attosecond pulses in the "single-cycle" regime.
Phys. Rev. Lett. **78**, 1251–1254 (1997).
- [155] C. Spielmann, N. H. Burnett, S. Sartania, R. Koppitsch, M. Schnürer, C. Kan, M. Lenzner, P. Wobrauschek, and F. Krausz.
Generation of Coherent X-rays in the Water Window Using 5-Femosecond Laser Pulses.
Science **278**, 661–664 (1997).
- [156] M. Y. Emelin, M. Y. Ryabikin, A. M. Sergeev, M. D. Chernobrovvtseva, T. Pfeifer, D. Walter, and G. Gerber.
Attosecond Burst and High-Harmonic Generation in Molecular Ionization by Ultrashort Laser Pulses.
JETP Lett. **77**, 212–216 (2003).
- [157] T. Rickes, L. P. Yatsenko, S. S. T. Halfmann, B. W. Shore, N. V. Vitanov, and K. Bergmann.
Efficient adiabatic population transfer by two-photon excitation assisted by a laser-induced Stark shift.
J. Chem. Phys. **113**, 534–546 (2000).
- [158] J. B. Watson, A. Sanpera, K. Burnett, and P. L. Knight.
Wave-packet recollision and pulse-shape effects in high-harmonic generation.
Phys. Rev. A **55**, 1224 (1997).

- [159] M. Protopapas, C. H. Keitel, and P. L. Knight.
Atomic physics with super-high intensity lasers.
Rep. Prog. Phys. **60**, 389–486 (1997).
- [160] L. D. Landau and E. M. Lifshitz.
Quantum Mechanics, volume 3 of *Course of theoretical physics*.
Third edition. Pergamon Press, Oxford (1977).
- [161] M. Y. Emelin, M. Y. Ryabikin, M. D. Chernobrovtsseva, A. M. Sergeev, T. Pfeifer, D. Walter, and G. Gerber.
High-efficiency generation of attosecond pulses during atomic ionization from excited electronic states.
Europhys. Lett. **69**, 913–919 (2005).
- [162] R. Velotta, N. Hay, M. B. Mason, M. Castillejo, and J. P. Marangos.
High-Order Harmonic Generation in Aligned Molecules.
Phys. Rev. Lett. **87**, 183901 (2001).
- [163] M. Lein, N. Hay, R. Velotta, J. P. Marangos, and P. L. Knight.
Role of the intramolecular phase in high-harmonic generation.
Phys. Rev. Lett. **88**, 183903 (2002).
- [164] A. Flettner, J. König, M. B. Mason, T. Pfeifer, U. Weichmann, R. Düren, and G. Gerber.
Ellipticity dependence of atomic and molecular high harmonic generation.
Europ. Phys. J. D **21**, 115–119 (2002).
- [165] A. Flettner, J. König, M. B. Mason, T. Pfeifer, U. Weichmann, and G. Gerber.
Atomic and molecular high-harmonic generation: A comparison of ellipticity dependence based on the three-step model.
J. Mod. Opt. **50**, 529–537 (2003).
- [166] A. D. Bandrauk and N. H. Shon.
Attosecond control of ionization and high-order harmonic generation in molecules.
Phys. Rev. A **66**, 031401(R) (2002).
- [167] J. A. Fleck, Jr., J. R. Morris, and M. D. Feit.
Time-Dependent Propagation of High-Energy Laser-Beams Through Atmosphere.
Appl. Phys. **10**, 129–160 (1976).
- [168] K. Burnett, V. C. Reed, J. Cooper, and P. L. Knight.
Calculation of the background emitted during high-harmonic generation.
Phys. Rev. A **45**, 3347–3349 (1992).
- [169] R. Numico, P. Moreno, L. Plaja, and L. Roso.
High-order harmonic generation after photodissociation.
J. Phys. B **31**, 4163–4171 (1998).
- [170] S. Baker, S. Robinson, C. A. Haworth, H. Teng, R. A. Smith, C. C. Chirila, M. Lein, J. W. G. Tisch, and J. P. Marangos.
Probing Proton Dynamics in Molecules on an Attosecond Time Scale.
Science **312**, 424 (2006).
- [171] T. Pfeifer, D. Walter, G. Gerber, M. Y. Emelin, M. Y. Ryabikin, M. D. Chernobrovtsseva, and A. M. Sergeev.
Transient Enhancement of High-Harmonic Generation in Expanding Molecules.
Phys. Rev. A **70**, 013805 (2004).
- [172] S. Eisebitt, J. Lüning, W. F. Schlotter, M. Lörger, O. Hellwig, W. Eberhardt, and J. Stöhr.
Nature **432**, 885 (2004).
- [173] *APS Analysis of Beethoven Hair Sample Yields Clues to Composer’s Life and Death (2000)*
http://www.aps.anl.gov/News/APS_News/2000/20001017.htm.

- [174] A. Rousse, P. Audebert, J. P. Geindre, F. Fallies, J. C. Gauthier, A. Mysyrowics, G. Grillon, and A. Antonetti.
Efficient $K\alpha$ x-ray source from femtosecond laser-produced plasmas.
Phys. Rev. E **50**, 2200–2208 (1994).
- [175] C. Rischel, A. Rousse, I. Uschmann, P. Albouy, J. Geindre, P. Audebert, J. Gauthier, E. Förster, J. Martin, and A. Antonetti.
Femtosecond time-resolved X-ray diffraction from laser-heated organic films.
Nature **390**, 490 (1997).
- [176] R. London.
Development of coherent x-ray lasers.
Phys. Fluids B **5**, 2707–2713 (1993).
- [177] J. J. Rocca.
Table-top soft x-ray lasers.
Rev. Sci. Inst. **70**, 3799–3827 (1999).
- [178] L. B. D. Silva, B. J. MacGowan, S. Mrowka, J. A. Koch, R. A. London, D. L. Matthews, and J. H. Underwood.
Power Measurements of a Saturated Yttrium X-Ray Laser.
Opt. Lett. **18**, 1174 (1993).
- [179] P. Zeitoun, G. Faivre, S. Sebban, T. Mocek, A. Hallou, M. Fajardo, D. Aubert, P. Balcou, F. Burgy, D. Douillet, S. Kazamias, G. de Lachèze-Murel, T. Lefrou, S. le Pape, P. Mercère, H. Merdji, A. S. Morlens, J. P. Rousseau, and C. Valentin.
A high-intensity highly coherent soft X-ray femtosecond laser seeded by a high harmonic beam.
Nature **431**, 426 (2004).
- [180] C. Gohle, T. Udem, M. Herrmann, J. Rauschenberger, R. Holzwarth, H. A. Schuessler, F. Krausz, and T. W. Hänsch.
A frequency comb in the extreme ultraviolet.
Nature **436**, 03851 (2005).
- [181] *The European X-Ray Laser Project XFEL (2006)*
<http://www.xfel.net/XFELpresse/en/hintergrund/index.html>.
- [182] S. V. Milton, E. Gluskin, N. D. Arnold, C. Benson, W. Berg, S. G. Biedron, M. Borland, Y.-C. Chae, R. J. Dejus, P. K. D. Hartog, B. Deriy, M. Erdmann, Y. I. Eidelman, M. W. Hahne, Z. Huang, K.-J. Kim, J. W. Lewellen, Y. Li, A. H. Lumpkin, O. Makarov, E. R. Moog, A. Nassiri, V. Sajaev, R. Soliday, B. J. Tieman, E. M. Trakhtenberg, G. Travish, I. B. Vasserman, N. A. Vinokurov, X. J. Wang, G. Wiemerslage, and X. Yang.
Exponential Gain and Saturation of a Self-Amplified Spontaneous Emission Free-Electron Laser.
Science **292**, 2037–2041 (2001).
- [183] L. H. Yu, M. Babzien, I. B. Zvi, L. F. DiMauro, A. Doyuran, W. Graves, E. Johnson, S. Krinsky, R. Malone, I. Pogorelsky, J. Skaritka, G. Rakowsky, L. Solomon, X. J. Wang, M. Woodle, V. Yakimenko, S. G. Biedron, J. N. Galayda, E. Gluskin, J. Jagger, V. Sajaev, and I. Vasserman.
High-gain harmonic-generation free-electron laser.
Science **289**, 932–934 (2000).
- [184] L. H. Yu, L. DiMauro, A. Doyuran, W. S. Graves, E. D. Johnson, R. Heese, S. Krinsky, H. Loos, J. B. Murphy, G. Rakowsky, J. Rose, T. Shaftan, B. Sheehy, J. Skaritka, X. J. Wang, and Z. Wu.
First ultraviolet high-gain harmonic-generation free-electron laser.
Phys. Rev. Lett. **91**, 074801 (2003).
- [185] F. Verluise, V. Laude, Z. Cheng, C. Spielmann, and P. Tournais.
Amplitude and phase control of ultrashort pulses by use of an acousto-optic programmable dispersive filter: pulse compression and shaping.
Opt. Lett. **25**, 575–577 (2000).
- [186] R. Bartels, S. Backus, I. Christov, H. Kapteyn, and M. Murnane.
Attosecond time-scale feedback control of coherent X-ray generation.

- Chem. Phys. **267**, 277–289 (2001).
- [187] D. H. Reitze, S. Kazamias, F. Weihe, G. Mullot, D. Douillet, F. Augé, O. Albert, V. Ramanathan, J. P. Chambaret, D. Hulin, and P. Balcou.
Enhancement of high-order harmonic generation at tuned wavelengths through adaptive control.
Opt. Lett. **29**, 86–88 (2004).
- [188] T. Pfeifer, U. Weichmann, S. Zipfel, and G. Gerber.
Compression and shaping of a self-phase-modulated laser pulse with a deformable mirror device.
J. Mod. Opt. **50**, 705–710 (2003).
- [189] C. Altucci, R. Bruzzese, C. de Lisio, M. Nisoli, S. Stagira, S. D. Silvestri, O. Svelto, A. Boscolo, P. Ceccherini, L. Poletto, G. Tondello, and P. Villorosi.
Tunable soft-x-ray radiation by high-order harmonic generation.
Phys. Rev. A **61** (1999).
- [190] W. R. Hunter.
Windows and Filters, volume 31 of *Experimental Methods in the Physical Sciences*, chapter 16, pp. 305–3346.
First edition. Academic Press, San Diego (1998).
- [191] T. Pfeifer.
Adaptive Control of Coherent Soft X-Rays.
Dissertation, Universität Würzburg (2004).
- [192] A. Baltuška, T. Udem, M. Uiberacker, M. Hentschel, E. Goulielmakis, C. Gohle, R. Holzwarth, V. S. Yakovlev, A. Scrinzi, T. W. Hänsch, and F. Krausz.
Attosecond control of electronic processes by intense light fields.
Nature **421**, 611–615 (2003).
- [193] U. Weichmann.
Erzeugung hoher Harmonischer von Femtosekunden-Laserpulsen.
Dissertation, Universität Würzburg (2001).
- [194] E. Spiller.
Reflecting Optics: Multilayers, volume 31 of *Experimental Methods in the Physical Sciences*, chapter 14, pp. 271–288.
First edition. Academic Press, San Diego (1998).
- [195] T. Pfeifer, F. Dimler, R. Spitzenpfeil, D. Walter, C. Winterfeldt, C. Spielmann, and G. Gerber.
Towards optimal control with shaped soft-x-ray light.
Opt. Expr. (2007).
- [196] NIST, *Chemistry Web Book (2006)*
<http://webbook.nist.gov/>.
- [197] K. Mochiji, K. Lee, C. I. Ma, D. Y. Kim, M. Mahalingam, and D. M. Hanson.
Photodissociation of SF₆ Near the F 1s Absorption-Edge.
J. Vac. Sci. Technol. A **12**, 216–218 (1994).
- [198] D. S. Peterka, M. Ahmed, C. Y. Ng, and A. G. Suits.
Dissociative photoionization dynamics of SF₆ by ion imaging with synchrotron undulator radiation.
Chem. Phys. Lett. **312**, 108–114 (1999).
- [199] M. Ono and K. Mitsuke.
Anisotropy of fragment ions from SF₆ by photoexcitation between 23 and 210 eV.
Chem. Phys. Lett. **366**, 595–600 (2003).
- [200] M. Ono and K. Mitsuke.
Kinetic energy distribution and anisotropy of fragment ions from SF₆ by photoexcitation of a sulfur 2p-electron.
Chem. Phys. Lett. **379**, 248–254 (2003).

- [201] W. C. Wiley and I. H. McLaren.
Time-of-Flight Mass Spectrometer with Improved Resolution.
Rev. Sci. Instr. **26**, 1150–1157 (1955).
- [202] J. Günther.
Femtosekunden-Laserpulse im Vakuum-Ultraviolett.
Diplomarbeit, Universität Würzburg (2000).
- [203] A. Palacios, H. Bachau, and F. Martin.
Enhancement and Control of H₂ Dissociative Ionization by Femtosecond VUV Laser Pulses.
Phys. Rev. Lett. **96**, 143001 (2006).
- [204] W. Eberhardt, T. K. Sham, R. Carr, S. Krummacher, M. Strongin, S. L. Weng, and D. Wesner.
Site-Specific Fragmentation of Small Molecules Following Soft-X-Ray Excitation.
Phys. Rev. Lett. **50**, 1038–1041 (1983).
- [205] R. L. Abrams.
Coupling losses in hollow waveguide laser resonators.
IEEE Journal of Quantum Electron. **8**, 838–843 (1972).
- [206] D. Homoelle and A. L. Gaeta.
Nonlinear Propagation dynamics of an ultrashort pulse in a hollow waveguide.
Opt. Lett. **25**, 761–763 (2000).
- [207] G. Tempea and T. Brabec.
Theory of self-focusing in a hollow waveguide.
Opt. Lett. **23**, 762–764 (1998).
- [208] T. Pfeifer, R. Kemmer, R. Spitzenpfeil, D. Walter, C. Winterfeldt, G. Gerber, and C. Spielmann.
Spatial control of high-harmonic generation in hollow fibers.
Opt. Lett. **30**, 1497–1499 (2005).
- [209] E. Yablonov.
Self-Phase Modulation and Short-Pulse Generation from Laser-Breakdown Plasmas.
Phys. Rev. A **10**, 1888–1895 (1974).
- [210] R. M. Jenkins and R. W. J. Devereux.
Effect of field regeneration on the TEM₀₀ transmission characteristics of a circular-section waveguide.
Appl. Opt. **31**, 5086–5091 (1992).
- [211] A. Paulus, C. Winterfeldt, T. Pfeifer, D. Walter, G. Gerber, and C. Spielmann.
Novel time-of-flight electron spectrometer optimized for time-resolved soft-x-ray photoelectron spectroscopy.
Rev. Sci. Instrum. **77** (2006).
- [212] T. Hara, N. Fukuchi, Y. Kobayashi, N. Yoshida, Y. Igasaki, and M. H. Wu.
Electrically addressed spatial light phase modulator.
T. Hara, 5000 Hirakuchi, Hamakita-City, Japan (2000) (hara@crl.hpk.co.jp) .
- [213] D. Ebel.
Projektpraktikum, Universität Würzburg (2004).
- [214] A. Heinz.
Projektpraktikum, Universität Würzburg (2004).

Acknowledgments

I would like to thank all the members of “Experimentelle Physik 1” that I had the pleasure to work with over the last years. Many of the achievements reported in this thesis have been the result of joint efforts and excellent team work. It is a relieving feeling to work in an environment of friends that are eager to approach any of the smaller and bigger problems that are encountered day for day.

Special thanks are given to the following people:

- Prof. Dr. Gustav Gerber, for providing me with unique working conditions in an exciting research field, for the experimental freedom to pursue own ideas, for his generous support and gentle advice over all the years and also for his essential contribution to the successful completion of my Master Thesis in Stony Brook.
- Prof. Dr. Christian Spielmann, for his devotion to any of the different projects, the invaluable support of his experience in the field and the additional financial support to experience work in different laboratory environments with state of the art equipment.
- Prof. Dr. Alexander Mikhail Sergeev for providing his theoretical expertise and the fundamental code for many of the simulations shown in this work.
- Dr. Thomas Pfeifer for his motivation and extensive collaboration during the first half of this work and his friendly help and support long afterwards.
- Jan Lohbreier for being the ideal coworker for the last half of this work, for being open-minded for a lot of “quick-and-dirty” measurements and for all the fun and the excellent teamwork during and after work.
- Robert Spitzenpfeil for design the and construction of a new vacuum system and a great part of the new lab and his passion to unravel the mysteries of all kinds of physical and mathematical problems.
- Carsten Winterfeldt for successful collaboration during the optimization of high harmonics, his expertise with optical setups and the english language.
- Frank Dimler for being the ideal person for lots of discussions of (not only) physical problems and theories far beyond the daily course of life in the lab.
- Alexander Paulus for being able to raise the mood of all people around him and for always keeping excellent relationship to the machine shop.

- Stefan Eyring for his important contributions to the new experimental setup, for being a reliable source of information in and out of the lab and for all the exciting and funny sessions together.
- Many thanks to the “old” and the “new” computer administration team. Christian Dietl and Patrick Niklaus did the job during the initial part of this work. Special thanks to Sandra Dantscher for her support during our own “period of duty”. Not to forget Robert Spitzenpfeil and Jan Lohbreier who finally relieved us of this “burden”.
- The diploma students for much more than making important contributions in many ways: Axel Flettner (construction of the Microdroplets-Setup), Claudia Tremel (visible-laser-pulse polarization shaping), Alexander Paulus (soft x-ray photoelectron spectrometer construction and operation), Frank Dimler (construction and first studies with the new hollow fiber setup), Thomas Sokollik (visible-NIR crosscorrelation studies). Especial thanks to Ron Kemmer (design and construction of the new pulse shaping setup), Marisa Mäder (construction and first studies of the filament-setup) and Stefan Eyring (design and construction of the new x-ray spectrometer).
- Michael Hafner and his brother Julian Hafner for their help and motivated support during different periods of this work and all their designs for the machine shop.
- Michael Pieper for his patience with the first test-setup for high-harmonic generation in hollow fibers.
- The large number of advanced lab (Fortgeschrittenenpraktikum) students for their interest and work in many different areas: Jan Pfannes (SPIDER characterization), Markus Müller and Thomas Sokollik (both: Water-microdroplet studies in experiment and simulation), Daniel Kurfeß (CPA design), Philipp Mertsch (high-harmonic generation in heteronuclear molecules), Andreas Wörle (high-energy photoelectron spectroscopy), Dimitri Ebel (spatial laser-pulse shaping), Stefan Eyring (soft-x-ray beamline design), Melanie Kögler (x-ray spectrometer characterization), Alexander Heinz (programmable spatial wavefront analysis), Daniel Höhne (flat-field x-ray spectroscopy), Martin Batzer and Stefan Kirsch (stabilization of laser pulses), Ragnar Gleim (construction of a HHG-meter), Stefan Geisendrfer (design and construction of the Ni-tube for HHG) and all the others that have not been mentioned.
- Helga Schwark, Monika Seifer, and Diep Phan for being always there to solve all kinds of non-physical problems and to shield us from a lot of administrative paperwork.
- The rest of the EP1 group for being great friends and colleagues.

Lebenslauf

Persönliche Daten

Name: Dominik Walter
Wohnort: An der Hardt 12, 97292 Holzkirchen
geboren am: 4. Mai 1977 in Würzburg
Staatsangehörigkeit: deutsch
Familienstand: ledig

Schulbildung

09/1983 – 07/1987 Grundschohle Holzkirchen
09/1987 – 07/1988 Hauptschohle Helmstadt
09/1988 – 06/1997 "Balthasar-Neumann-Gymnasium" Marktheidenfeld
Juni 1997 Allgemeine Hochschulreife

Grundwehrdienst

07/1997 – 04/1998 "Pionierkaserne an der Schanz" Ingolstadt

Studium der Physik

5/1998 – 07/2000 "Bayerische Julius-Maximilians-Universität" Würzburg
10/1999 Vordiplom Physik
08/2000 – 08/2001 Stony Brook State University of New York (USA)
08/2001 Abschluss: Master of Arts (Thesis: "Ionization of Hydrogen Rydberg Atoms by Static and LP Microwave Fields at High Scaled Frequencies")
02/2002 Diplom Physik (Universität Würzburg)
seit 03/2002 "Bayerische Julius-Maximilians-Universität" Würzburg
Promotion bei Prof. Dr. G. Gerber

Berufsweg

seit 03/2002 wissenschaftlicher Mitarbeiter der Universität Würzburg

Würzburg, den 18. Dezember 2006

Dominik Walter